

Accepted Manuscript

Mechanical properties of high-entropy alloys with emphasis on face-centered cubic alloys

Zezhou Li, Shiteng Zhao, Robert O. Ritchie, Marc A. Meyers

PII: S0079-6425(18)30117-8

DOI: <https://doi.org/10.1016/j.pmatsci.2018.12.003>

Reference: JPMS 545

To appear in: *Progress in Materials Science*

Received Date: 9 March 2018

Revised Date: 15 December 2018

Accepted Date: 16 December 2018



Please cite this article as: Li, Z., Zhao, S., Ritchie, R.O., Meyers, M.A., Mechanical properties of high-entropy alloys with emphasis on face-centered cubic alloys, *Progress in Materials Science* (2018), doi: <https://doi.org/10.1016/j.pmatsci.2018.12.003>

This is a PDF file of an unedited manuscript that has been accepted for publication. As a service to our customers we are providing this early version of the manuscript. The manuscript will undergo copyediting, typesetting, and review of the resulting proof before it is published in its final form. Please note that during the production process errors may be discovered which could affect the content, and all legal disclaimers that apply to the journal pertain.

Mechanical properties of high-entropy alloys with emphasis on face-centered cubic alloys

Zezhou Li¹, Shiteng Zhao¹, Robert O. Ritchie², Marc A. Meyers^{1,*}

¹ Dept. of Mechanical & Aerospace Engineering, University of California, San Diego, CA 92093, USA

² Materials Sciences Division, Lawrence Berkeley National Laboratory, and Dept. of Materials Science & Engineering, University of California, Berkeley, CA 94720, USA.

ACCEPTED MANUSCRIPT

* Corresponding author: Marc A. Meyers; email: mameyers@eng.ucsd.edu

Contents

Mechanical properties of high-entropy alloys	0
1. Introduction and objectives	4
1.1 Entropy effect.....	8
1.2 Severe lattice-distortion effect	11
1.3 Short-range order effect	12
1.4 Sluggish diffusion.....	14
1.5 “Cocktail” effect.....	15
2. Alloy preparation	16
2.1 Phase selection rules	16
2.2 Synthesis methods	18
3. Mechanical properties of high-entropy alloys	18
3.1 Elastic constants	19
3.2 Strengthening mechanisms	20
3.3 Hardness.....	23
3.4. Hall-Petch relationship	24
3.5 Wear.....	26
3.6 Tensile behavior	27
3.6.1 Strain hardening	28
3.6.2 Strength and ductility trade-off.....	29

3.6.2.1 Lattice distortion and stacking-fault energy effect	35
3.6.2.2 Twinning effect	35
3.7 Fracture toughness.....	40
3.7.1 Fracture morphology.....	43
3.8 Fatigue	43
3.9 Dynamic strain aging.....	46
3.10 High-temperature properties	49
3.11 Creep.....	50
3.11.1 Creep mechanisms	50
3.11.2 Superplasticity	53
3.12 Compression response in micro/nanopillar experiments	55
3.13 High strain-rate and high-pressure deformation.....	56
4. Summary and conclusions.....	62
Acknowledgments	65
References	66

Abstract

High-entropy alloys (HEAs), also known as multi-principal element alloys or multi-component alloys, have been the subject of numerous investigations since they were first described in 2004. The earliest HEA was the equiatomic CrMnFeCoNi "Cantor" alloy, but HEAs now encompass a broad class of metallic and ceramic systems. The concept of utilizing the high entropy of mixing to develop stable multi-element alloys may not be scientifically correct but has produced extraordinary mechanical properties in specific HEAs, mainly CrCoNi-based alloys, associated with their continuous work-hardening rate that is sustained to large plastic strains (~0.5) and at low temperatures. This, in combination with the high frictional forces on dislocations and a propensity for twinning, leads to outstandingly high fracture toughness values (exceeding $200 \text{ MPa.m}^{1/2}$) and resistance to shear-band formation under dynamic loading. The critical shear strain for the onset of adiabatic shear band formation is ~7 for the Cantor alloy, much higher than that for conventional alloys, suggesting superior ballistic properties. The slower diffusion rates resulting from the multi-element environment contribute to the excellent intermediate-temperature performance. We review the principal mechanical properties of these alloys with emphasis on the face-centered cubic systems, such as the CrCoNi-based alloys. Their favorable mechanical properties and ease of processing by conventional means suggest extensive utilization in many future structural applications.

1. Introduction and objectives

The development of materials for structural applications usually calls for exceptional mechanical properties, such as high strength, good ductility, excellent fracture toughness, and sometimes creep and wear resistance [1, 2]. The mechanical performance of such materials is related to their crystal structure and chemical composition, and most importantly, to their microstructure. In this regard, seldom are superior mechanical properties achieved with a single element composition, and the past century has witnessed the development of several high strength, high toughness materials, as exemplified by superalloys, transformation-induced plasticity (TRIP) steels, dual-phase (DP) steels, ultrafine-grained materials (although these often lack toughness), and specific bulk-metallic glasses and their derivatives. These materials are, with the exception of the bulk-metallic glasses, crystalline and based on one major component, such as iron in steels, *etc.*; they additionally contain secondary elements serving to contribute to specific properties, such as corrosion resistance in stainless steels or to strength using the classical hardening mechanisms with which materials scientists and engineers are so familiar - solid-solution, precipitation, dispersion, transformation and grain-size reduction. Alternatively, composites of different classes of materials have been developed in parallel, with their own unique advantages. These materials comprise a continuous or discontinuous reinforcement entity housed within a polymer, metal, or ceramic matrix; depending on their dimensionality, they are classified into laminar-, fiber-, and particle-reinforced composites.

A distinctly different approach emerged in the early 2000s that was based on nominally equiatomic multi-component alloys typically with five or more elements, which were claimed to form stable single-phase solid solutions. This stability was attributed to the high entropy of mixing associated with a disordered solution of several elements, which was presumed to overwhelm the enthalpy of phase

formation. This concept, first proposed by Yeh and co-workers [3] in Taiwan and independently by Cantor and co-workers [4] in the U.K., has come to be known as “high-entropy alloys” and has proven to be of great significance in the design of new alloys.

Cantor *et al.* [4], in their seminal 2004 paper, pointed out that little was known about multi-component alloys with elements in equal or near-equal ratios since most alloy design investigations have traditionally focused on metallic materials based on one principal element. Accordingly, they explored the multi-component alloys using 3d transition elements. The initial experiments (in the 1980s) involved twenty elements in equal atomic fractions, out of which emerged an equiatomic, face-centered cubic (*fcc*) alloy with five elements of varying crystal structures (*fcc*, body-centered cubic (*bcc*), hexagonal closed packed (*hcp*)): Co (*hcp*), Fe (*bcc*), Cr (*bcc*), Mn (*bcc*) and Ni (*fcc*). This alloy, termed the “Cantor” alloy [5], is single-phase with the five elements apparently equally distributed (see the composition maps in Fig. 1), although the alloy has been subsequently shown to decompose after prolonged (500 day) anneals at 700°C, where a grain-boundary Cr-rich precipitate forms, and at 500°C where multiple phases can form at grain boundaries [6].

Concurrent with Cantor, Ramachandran [7] proposed the concept of “cocktail alloys” in which metals can be mixed as a multi-element mixture to form bulk metallic glasses or single-phase crystalline alloys. For metallic materials, the “cocktail effect” is not particularly scientific but simply implies that unexpected properties could be obtained after mixing many elements together, something which cannot be achieved in a material comprised of a single independent element.

Yeh *et al.* [3], in their classic paper, first proposed the notion of the design of an alloy with a series of elements in equimolar ratios based on the concept of a high configurational (or mixing) entropy. The mixing entropy is determined by the occupation of the atomic sites with different atoms; as such, possible configurations of n types of undistinguishable atoms in N sites produces the configurational (or

mixing) entropy. Different sizes of atoms lead to the distortion of sites which gives their excess entropy. This influence is small for dilute solid solutions, where few atoms are strained by the surrounding principal atoms, depicted in Fig. 2(a). This figure also presents the very minor influence of solutes on periodic Peierls-Nabarro energy barriers for dislocation motion in dilute solid solution. However, the uncertainty in atom locations increases with increasing differences in atomic sizes and concentrations. As the atoms may deviate from their lattice sites with the increase of different kinds of solutes (Fig. 2(b)), in theory, the mechanical properties (such as solid solution strengthening) of a complex, concentrated solid solution can be tuned by this lattice-distortion effect.

Although the notion of the high configurational entropy overwhelming the enthalpy of phase formation to create single-phase solid solutions in high-entropy alloys is certainly not universal, we believe that Yeh *et al.* [3]’s terminology will remain. However, as the field has evolved over the first 15 or so years, some degree of classification has emerged. We present here the classes identified by Miracle and Senkov [8] and Miracle *et al.* [9] which supplement Yeh’s categories based on configurational entropy [25]:

- Transition metal based HEAs, such as the CrMnFeCoNi; there are actually 38 transition metals.
- Refractory HEAs, such as the NbMoTaW; the principal elements here are: Ti, V, Cr, Nb, Mo, Hf, Ta, and W.
- Low-density HEAs, such as the $\text{Li}_{20}\text{Mg}_{10}\text{Al}_{20}\text{Sc}_{20}\text{Ti}_{30}$ HEA; the principal elements are: Li, Be, Mg, Al, Si, Sc, Ti, Zn, and Sn.
- Ceramic HEAs. Oxides [10], metal diborides [11], and perovskite structures [12]. This represents a new direction within HEA research; metal cations can be mixed with oxygen, boron, and other anions to produce covalently and ionically bonded materials. Diborides are synthesized by

maintaining the cationic components in equiatomic fraction plus boron [11]. In this manner, $(\text{Ti}_{0.2}\text{Zr}_{0.2}\text{Nb}_{0.2}\text{Hf}_{0.2}\text{Ta}_{0.2})\text{B}_2$ has been produced.

- Other types of HEAs: Lanthanide HEAs (consisting at least 4 of the lanthanide (4f) elements Dy, Gd, Lu, Tb and Tm, plus the element Y), brasses and bronzes, and precious metals [8]. The motivation behind the complex, concentrated brasses and bronzes alloys is to expand their broad range, and to achieve higher levels of strength through concentrated solid solutions. The representative alloys are $\text{Al}_x\text{Sn}_y\text{Zn}_z[\text{CuMnNi}]_{(1-x-y-z)}$ [13]. The precious metals are mainly used for catalysis applications. The elements in precious metal HEAs are mainly Ag, Au, Co, Cr, Cu, Ni, Pd, Pt, Rh and Ru. The alloys use the equi-atomic alloy substitution method. An earlier phase diagram study also identified a single-phase *hcp* MoPdRhRu alloy [14].

Miracle and Senkov [8] discuss at length the appropriateness of naming these alloys HEAs and propose additional designations, more attuned to alloys in which there are other phases present and alloys in which the stability is not governed by the Boltzmann mixing entropy. Thus, terms such as multi-principal element alloys (MPEAs) and complex concentrated alloys (CCAs) have been proposed, although we believe, as noted above, that the generic term of “high-entropy alloys” will continue to be used to generally describe these multiple-element alloys.

Recently, exceptional mechanical and physical properties of HEAs have been discovered for the CrCoNi-based series of alloys, and this is the stimulus for this article. Specifically, Gludovatz *et al.* [15] reported the superior fracture toughness of the Cantor alloy at both room and cryogenic temperatures, as shown in Fig. 3. In fact, the CrMnFeCoNi alloy represents one of the toughest materials reported to date with a plane-strain fracture toughness, K_{lc} , that exceeds 200 MPa.m^{1/2} with an outstanding tensile strength exceeding 1 GPa. Although other properties are not the focus of this review, as an example of exceptional functional behavior, these equiatomic CoCrNi single-phase alloys have also been reported to

be more resistant to radiation damage, as compared to the pure elements, due to a significant decrease in the mobility of dislocations [16].

The ratio of the number of publications under the heading “high-entropy alloy” to the total number of Elsevier publications keeps increasing dramatically over the past decade, from 2×10^{-5} (20 per million) in 2009 to 2.4×10^{-4} (240 per million) in 2018, as shown in Fig. 4, suggesting the prominence of this new alloy design philosophy. In absolute numbers, 900 papers were published in 2018. This is an amazing trajectory considering that this is a twelve-year span since they were first discovered. In light of this, the goal of this article is to focus on the mechanical properties of HEAs. Three excellent reviews were published by Zhang *et al.* [17] and Tsai and Yeh [18] in 2014, and by Miracle and Senkov [8] in 2017; these are supplemented by two comprehensive books, by Gao *et al.* [19] and Murty *et al.* [20]. The focus of these articles will not be repeated here; rather the emphasis is on the structure-property linkages responsible for the outstanding strength, fracture toughness and dynamic properties of certain high-entropy alloys.

However, before we discuss their mechanical properties, we first examine high-entropy alloys from five aspects:

- The high-entropy effect.
- The lattice-distortion effect.
- Short-range order effect.
- The sluggish diffusion effect.
- The “cocktail” effect.

1.1 Entropy effect

The statistical-mechanics definition of entropy developed by Boltzmann in 1870s has been successfully used to analyze the thermodynamic stability of the microscopic components in alloys [21-

24]. Boltzmann's hypothesis states that the entropy of a system, S , is linearly related to the logarithm of the frequency of the occurrence of a macro-state or, more precisely, the number, W , of the possible micro-states corresponding to the macroscopic state of a system:

$$S = k \ln W , \quad (1.1.1)$$

where $k = 1.38 \times 10^{-23}$ J.K⁻¹ is Boltzmann's constant. For a simple two-component system with atomic fractions x_1 and x_2 , the entropy is derived using Stirling's approximation to give the classic expression:

$$S_{mix} = -k(x_1 \ln x_1 + x_2 \ln x_2) . \quad (1.1.2)$$

The ideal configurational (or mixing) entropy (per mole) for a number of elements equal to n is obtained in a similar fashion:

$$S_{mix} = -R \sum_1^n x_i \ln x_i , \quad (1.1.3)$$

where R is the gas constant, equal to $N_A k$ (N_A is Avogadro's number). For equal atomic fractions, $x_i = 1/n$, Eqn. 1.1.3 reduces to:

$$S_{mix} = -R \ln 1/n = R \ln n , \quad (1.1.4)$$

where n' is the number of the elements in equimolar ratio. The corresponding change of the mixing entropy is shown in Fig. 5(a) [25]. The Gibbs free energy is expressed as:

$$\Delta G_{mix} = \Delta H_{mix} - T \Delta S_{mix} , \quad (1.1.5)$$

where ΔS_{mix} is the mixing entropy defined in Eqn. 1.1.4, T is the temperature in Kelvin, and ΔH_{mix} is the mixing enthalpy. From Eqn. 1.1.5, one can see that if ΔH_{mix} does not change, a higher mixing entropy results in a reduced Gibbs free energy, which stabilizes the alloys. However, Miracle and Senkov [8]

warn that only a small fraction of the solutions are ideal or regular and that the majority is sub-regular. As this analysis does not consider the mismatch entropy due to the atom-size difference [26], an additional term must be introduced for rigor.

This provided the origin of the name “high-entropy alloy” (HEA), with a value of $1.6R$ for the entropy of mixing five elements, distinguishing them from the conventional alloys. Based on the value of the ideal configurational entropy, according to Yeh *et al.* [25], the high-entropy alloys can be categorized into three types, shown in Fig. 5(b). Low-entropy alloys (LEAs) are classical alloys with one principal element. High-entropy alloys (HEAs) contain five or more principal elements. An additional group, medium-entropy alloys (MEAs) has 2 to 4 principal elements. Note that the appearance of multiple phases has still been observed in the HEAs with the increase in the mixing entropy – only a few HEAs are truly single-phase – but this problem should be less prevalent in MEAs.

The question as to the importance of the role the mixing entropy in achieving single-phase structures in equiatomic multi-element HEAs was examined by Otto *et al.* [27]. They investigated six different HEAs with five equimolar elements, and argued that if the mixing entropy does not change for these HEAs, different sets of elements should still create single-phase alloys, thereby demonstrating that the high-entropy effect can stabilize the single phase. However, as can be seen from Fig. 6, a single-phase microstructure was only observed for the original Cantor alloy. Other five types of HEAs [27] contained different phases such as Laves phases or numerous topologically close-packed (tcp) phases, designated as the μ , χ , and σ [28]. Therefore, as noted above, the assumption that the high-entropy effect can stabilize a single phase in HEAs is only occasionally accurate.

Furthermore, combined with the CALPHAD (Computed Phase Diagram) method for thermodynamic analysis, Otto *et al.* [27] provide insight into the design strategy of HEAs: (i) Both the mixing enthalpy and the mixing entropy play an significant role in minimizing the Gibbs free energy of

HEAs instead of merely increasing the mixing entropy, and (ii) it was established that if HEAs contain any elements which tend to form intermediate phases or compounds when alloyed as binary pairs, it is usually reflected in the microstructure with the presence of other phases instead of one single phase. Additionally, the sluggish diffusion effect of solutes often leads to the formation of nano-sized precipitates, as shown in Fig. 7. Nano-sized precipitates inside a spinodal plate appear in the CrFeCoNiCu alloy in Fig. 7(A) [3]. Fig. 7(B) shows that the microstructure of this alloy is very complicated, including the nano-sized precipitates, amorphous phases, and ordered or disordered solid-solution phases. This characteristic is caused by the interaction between all the mixing elements.

1.2 Severe lattice-distortion effect

Since each element has its specific and unique atomic size, severe lattice distortion can occur in HEAs. This is shown in Fig. 2 in a schematic fashion and create an irregular pattern of Peierls-Nabarro energy barriers. The lattice-distortion effect breaks up the perfect crystal structure, which in turn can influence the mechanical properties of HEAs [29]. A group of AlSiCrFeCoNiCu alloys, synthesized by adding different elements to Cu in equal atomic fractions was examined using x-ray diffraction (XRD) by Yeh *et al.* [30]. They demonstrated a significant decrement in the XRD intensities with the addition of more elements. Fig. 8(a) shows a schematic drawing of the pure metals with perfect crystal structure, while Fig. 8(b) shows severe x-ray scattering due to lattice-distortion, which can lead to the reduced peak intensity values shown in Fig. 8(c).

Fig. 8(c) shows the effects of lattice-distortion and temperature on the XRD peak intensity [30]. This effect is due to atoms deviating from their lattice sites. To quantify this, a new structure factor was proposed to modify the peak intensities of XRD patterns. Combined with the Debye–Waller temperature

factor M^T , the new structure factor $\bar{F}_{hkl}^{T,D}$ at a temperature T is given by:

$$\bar{F}_{hkl}^{T,D} = F_{hkl} \exp(-M^T - M^D), \quad (1.2.1)$$

where F_{hkl} is the structure factor for a specific $(h k l)$ crystal plane at the temperature of 0 K, not considering the thermal-fluctuation and lattice-distortion effects. Similar to the thermal-vibration factor

M^T, M^D is the lattice distortion factor. $\bar{F}_{hkl}^{T,D}$ includes both thermal-fluctuation and the lattice-distortion effects. Fig. 8(b) indicates the severity of this lattice-distortion effect, which causes the deviation of different kinds of atoms from their lattice sites. Thus, XRD patterns of different alloys in Fig. 8(d) demonstrate that the irregularities in the diffracted lattice planes can suppress the intensities of peaks. The peak intensities decrease with the addition of the equal percentage of other elements into pure Cu.

1.3 Short-range order effect

The short-range order (SRO) in the local structure of HEAs plays an important role on mechanical properties. The existence of local chemical SROs in HEAs is still a somewhat of a controversial issue, largely because to date it has not been convincingly verified by experiment. However, it is now more feasible by atom probe tomography and advanced transmission electron microscopy techniques to investigate short-range ordering at the atomic scale [31, 32].

Using a Density Functional Theory (DFT-) based Monte Carlo approach, Ding *et al.* [33] revealed a strong tendency for the formation of chemical short-range order in CrCoNi medium-entropy alloys, particularly around Cr atoms, which favor Ni and Co atoms as nearest neighbors. These neighbors cause an enhancement in the second and third shells of Cr. The DFT simulation results show that the degree of chemical short-range order varies from the random configuration up to the highest degree of order realized in the Monte Carlo approach simulations, leading to a large variation of the value of average intrinsic stacking fault energy $\bar{\gamma}_{isf}$ shown in Fig. 9(A). The value of $\bar{\gamma}_{isf}$ increases from -42.9 to $30 \text{ mJ}\cdot\text{m}^{-2}$, whereas the average stacking-fault energy $\bar{\gamma}_{esf}$ ranges between -27.8 and 66

$\text{mJ}\cdot\text{m}^{-2}$ as summarized in Figs. 9(B) and (C). In comparison, the experimentally measured value of $\bar{\gamma}_{isf}$, $22 \pm 4 \text{ mJ}\cdot\text{m}^{-2}$ [34], falls within the range predicted by the DFT calculation, suggesting that CrCoNi alloys may contain some degree of local chemical order. The study demonstrates the influence of local chemical short-range order on twinning, and even phase (*fcc* to *hcp*) transformation in CrCoNi medium-entropy solid-solution alloys, whose combination of strength, ductility, and toughness properties approaches the best on record [145].

Zhang *et al.* [39] also reported calculations of a negative stacking-fault energy (at 0 K) in the *fcc* CrCoNi and CrFeCoNi alloys through first-principles calculations. Similarly, they discovered that the stacking-fault energy of high-entropy alloys, dependent on valence electron counts, d-electron density and lattice distortion, can be tuned by the local atomic environment. The negative stacking-fault energy was caused by the energetic preference of *hcp* stacking, resulting in the metastable *fcc* structure at low temperatures.

Using x-ray diffraction and neutron total scattering, Zhang *et al.* [35] examined whether short-range order exists in a CrCoNi medium-entropy alloy. The results suggest that the Cr atoms are prone to bond with Ni and Co atoms, and the short-range order is enhanced by ion irradiation, resulting in the observed segregation. Ma *et al.* [36] also reported that chemical short-range order can induce a specific structure in two HEAs with a composition of Al_2M_{14} ($\text{M} = \text{Ni}_4\text{Co}_4\text{Fe}_3\text{Cr}_3$ or $\text{Ni}_1\text{Co}_1\text{Fe}_2\text{Cr}_1$) high-entropy alloys instead of average random solid solution.

Lei *et al.* [37] reported that when a TiZrHfNb HEA was doped with 2 atomic per cent oxygen, the tensile strength increased (by 48.5 ± 1.8 per cent) and ductility was substantially improved (by 95.2 ± 8.1 per cent) whereas, under conventional condition, oxygen doping always embrittles metals. They proposed that the ordered interstitial oxygen complexes change the dislocation shear mode from

planar to wavy slip, and promotes double cross-slip and thus dislocation multiplication through the formation of Frank–Read sources during deformation.

1.4 Sluggish diffusion

Compared to pure metals and traditional alloys, HEAs can behave differently under deformation conditions. Tasi *et al.* [38] proposed a sluggish diffusion effect of the elements in HEAs, compared to that in pure metals and steels. Mishra *et al.* [29] suggested a lattice-strain effect for HEAs, which would lead to a smaller dislocation nucleation energy, stacking-fault energy (SFE) and twin-boundary energy, compared with traditional alloys, all factors which can readily change deformation behavior. Zhang *et al.* [39] found theoretically a negative SFE in CrCoNi and CrFeCoNi *fcc* HEAs (at 0 K) because the *fcc* stacking arrangements were thermodynamically metastable, making the occurrence of stacking faults or nano-twins easier. This was calculated by using the first-principles method. The motion of atoms, vacancies, dislocations, and twins during deformation can vary significantly with the different component elements and lattice distortions.

Atoms need to overcome a lattice potential energy barrier to migrate, although it is different for an atom migrating from lattice sites M to L than from L to M; this is referred as mean difference (MD) in Fig. 10. Fig. 10 shows that the mean difference for atoms in two adjacent sites L and M; there is no difference in energy for these two sites in pure metals as their surroundings are identical but for *fcc* CrFeNi and the CrMn₅₀FeCoNi medium- and high-entropy alloys, a significant mean difference is generated due to their different surrounding atmospheres. As atoms strive to maintain a position consistent with the lowest lattice potential energy, diffusion becomes more difficult in HEAs owing to this reduction in the jumping frequency. Tsai *et al.* [38] examined the diffusion of Ni in a CrMn_{0.5}FeCoNi HEA and found that the mean difference between two lattice sites was 60.3 meV, and the ratio of transitional frequencies Γ from L to M to that from M to L was equal to, at 1273 K:

$$\Gamma_{L \rightarrow M} / \Gamma_{M \rightarrow L} = \exp(-MD/k_B T) \approx 0.58. \quad (1.3.1)$$

This implies that a Ni atom will tend to remain at a lower lattice potential energy site about 1.7 times longer than at a higher lattice potential energy site. Yeh *et al.*'s [39] results also show that the CrMn_{0.5}FeCoNi HEA has a larger lattice potential energy fluctuation than the CrFeNi alloy. Additionally, the diffusion coefficient of Ni in CrMn₅₀FeCoNi alloy is 1.5 times lower than that in CrFeNi alloys. Thus, a variety of low lattice potential energy crystal positions can function essentially as "traps" and retard the diffusion of atoms. The lattice potential energy fluctuation and the severe trapping effect can lead to the sluggish diffusion-rate of atoms.

Summarizing, the larger potential energy variation in lattice sites is responsible for higher activation energies for atom migration and decreased diffusion rates, resulting in sluggish diffusion in HEAs. This sluggish-diffusion effect can influence mechanical properties of HEAs by increasing their creep resistance [40]. However, to counter this, Miracle and Senkov [8] have argued that the sluggish diffusion effect is actually non-existent – it is largely associated with the normal variability in diffusion data; it only appears when one normalizes the temperature to the melting point.

1.5 “Cocktail” effect

Ranganathan [7] proposed this term, suggesting, without rigorous scientific basis, that the use of multicomponent alloys can lead to unexpected and synergistic properties. Specifically, as a result of the ‘cocktail’ elements, unexpected properties can be obtained. Resulting materials that have unique properties due to these synergies are the GUM alloy (a titanium alloy with high elasticity, ductility and yield strength), bulk metallic glasses, and HEAs.

2. Alloy preparation

2.1 Phase selection rules

To predict the phases occurring in HEAs, two empirical models, known as, $\Delta H_{mixing} - \delta$ and $\Omega - \delta$, have been proposed and widely used. They are based on the classical Hume–Rothery rules for the formation of binary alloys based on atomic-size mismatch [41, 42]. A regular phase selection model, as shown in Fig. 11(a) [43], has been proposed to simplify the calculation of the free energy of the HEAs and specifically the enthalpy of mixing, ΔH_{mix} :

$$\Delta H_{mix} = \sum_{i=1, j>i}^n 4\Delta H_{AB}^{mix} c_i c_j , \quad (2.1.1)$$

where ΔH_{AB}^{mix} is the mixing enthalpy for the AB alloys and c_i is the atomic fraction of the i^{th} element. The atomic-size mismatch, δ , is given by:

$$\delta = \sqrt{\sum_{i=0}^n c_i (1 - r_i / \sum_{j=1}^n c_j r_j)^2} , \quad (2.1.2)$$

where r_i and r_j are, respectively, the radii of the different elements. Based on Fig. 11(a), solid solutions tend to appear when δ is less than 0.066, and ΔH_{mix} is between -11.6 kJ.mol⁻¹ and 3.2 kJ.mol⁻¹.

Zhang *et al.* [44-46] proposed another criterion with a thermodynamics-originated parameter, Ω , to replace ΔH_{mix} in the $\Delta H_{mix} - \delta$ prediction shown in Fig. 11(b). Ω is defined as:

$$\Omega = \frac{T_m \Delta S_{mix}}{|\Delta H_{mix}|} , \quad (2.1.3)$$

where $T_m = \sum_{i=1}^n c_i (T_m)_i$ is the average melting temperature and $(T_m)_i$ is the melting temperature of the i^{th}

element in the alloy. The parameter Ω represents the competition between ΔH_{mix} and $T_m \Delta S_{mix}$. This phase formation rule for a solid solution turns out to be $\Omega \geq 1.1$ and $\delta \leq 0.06$.

Jiang *et al.* [12] used Goldschmidt's tolerance factor, t , instead of cation-size difference to predict the formation and temperature-stability of single cubic (ionically bonded) perovskite solid solutions [47]:

$$t = \frac{R_A + R_o}{\sqrt{2}(R_B + R_o)} , \quad (2.1.4)$$

where R_A and R_B , are the radii of A and B cations, respectively, and R_o is the radius of oxygen anion. The cubic phase tends to be stable if $0.9 \leq t \leq 1.0$, while a hexagonal or tetragonal phase may form if $t > 1$, and an orthorhombic or rhombohedral phase may require $t < 0.9$ [47]. However, more experimental data are needed to determine whether there are exceptions to these established rules [48].

Senkov *et al.* [49] developed a novel method to promptly predict phases of metals by combining computed phase diagrams, phase transformation temperatures, and valid microstructures. They evaluated more than 130,000 alloy systems and tried to optimize promising compositions of HEAs. Their results established that a true solid solution was not determined simply by increasing the number of mixing elements in HEAs, as described above, thereby contradicting the initial hypothesis that increased configurational entropy can stabilize the single phase solid solutions. With the increase in the number of elements, the mixing entropy rises gradually while the possibility to form phases with binary elements develops more rapidly. Santodonato *et al.* [50] examined the microstructure evolution of the Al_{1.3}CrFeCoNiCu alloy during solidification and performed neutron diffraction studies from room temperature up to 1400°C. Although this alloy undergoes precipitation, segregation and spinodal decomposition, significant disorder still can be observed due to the formation of multiple phases (Table 1) [50,51]. These sequences indicate that mixing multiple elements will not always lead to a single phase.

2.2 Synthesis methods

Numerous traditional industrial and modern laboratory methods have been used to synthesize HEAs. Fig. 12 describes several fabrication processes of HEAs, which can be classified into three principal methods [19]:

- Bridgman solidification, arc-melting, induction melting, metal-spinning, rapid solidification of powders and others have been used when starting from a liquid mix.
- Solid-state processing, where plastic deformation is applied using different methods such as mechanical alloying, equal channel angular pressing and high-pressure torsion, the latter resulting in severely reduced grain sizes. More conventional methods such as extrusion, rolling, and forging can also be used.
- Gas mixing methods have also been applied and include different deposition methods, such as sputtering, ion-beam assisted deposition, pulse laser deposition, and molecular beam epitaxy.

The use of spark plasma sintering (SPS) is also effective in consolidating powders with high melting points; the technique can produce compacts with densities as high as 99.6% [52]. One favored manner to produce powders with nanocrystalline structures is to use ball milling. Another method is spray atomization of the alloy from five nozzles [53]; this can be achieved by simultaneous laser deposition. Thus, the synthesis and processing of HEAs use the vast arsenal of techniques developed for other metals and alloys.

3. Mechanical properties of high-entropy alloys

Using combinatorial theory, the maximum number of potential alloys comprising combinations of five elements from a pool of 118 elements can be estimated; this is equal to: $118!/(5! \cdot 113!)$ which means that there are potentially ~200 million new alloys to be explored. This is an astronomical number,

but of course includes many impractical elements, yet nevertheless illustrates the daunting task of exploring this vast universe of alloys. Even if one focuses on a much more limited number of elements such as transition metals (38), one still obtains a high number of potential new alloys, specifically $38!/(5!33!)$ or $\sim 500,000$ new compositions. It is not clear at this time how best to interrogate so many alloys, although one can make some assumptions that alloys with a face-centered cubic (fcc) structure are more likely to exhibit some degree of ductility, whereas those containing intermetallic compounds are likely to be the most brittle. Computational approaches generally focus on composition and bonding; this may be adequate for electronic materials, but not generally for structural materials as the mechanical properties are invariably controlled more by microstructure through thermo-mechanical treatment and often metastable phases, such as martensite in steels. The mechanical properties of alloys have been a subject of investigation for over a century, and it is clearly difficult to make generalizations. Thus, the sections below, while discussing specific examples, cannot be construed as generalizations.

3.1 Elastic constants

The dependence of the shear modulus, G , and Young's modulus, E , on the temperature for the Cantor alloy has been summarized by Gludovatz *et al.* [54], based on measurements conducted from 55 K to room temperature by Laplanche *et al.* [55] and from 200 K to 1000 K by Haglund *et al.* [56]. These two studies used ultrasonic resonant frequency techniques but the geometries of samples were different, although data from the two studies (at 200 - 293K) certainly overlap (Fig. 13). Values of the shear modulus and Young's modulus were found to be, respectively, 80 and 202 GPa at room temperature increasing to 85 and 214 GPa at 77 K. Using empirical Varshni expressions [57], the temperature dependence of the shear modulus and Young's modulus can be expressed (in GPa) as:

$$G = 85 - 16/(e^{448/T} - 1), \quad (3.1.1)$$

$$E = 214 - 35/(e^{416/T} - 1), \quad (3.1.2)$$

where T is the absolute temperature. It was reported that the temperature dependence of the shear modulus for the Cantor alloy is somewhat weaker than that for pure Ni [56, 58, 59]. The lower modulus of the Cantor alloy may be related to the melting temperature, because the modulus for metals decreases linearly with the reduction in the temperature when no magnetic or phase transformations take place [55]. In summary, compared to traditional metallic alloys [60], the temperature dependence of the elastic moduli of the Cantor alloy is in no way anomalous.

3.2 Strengthening mechanisms

The strengthening mechanisms are dependent on the structure of metals and alloys, and this naturally applies to HEAs. As mentioned earlier, the best-known mechanisms are solution, precipitation, strain, grain-size, dispersion, order, and transformation strengthening. Each HEA has to be considered separately and the contributions of the various mechanisms have to be assessed individually and, in many cases, synergistically.

Many effects such as short-range order, crystallographic structures, interstitial solutes and concentration can influence the solid-solution strengthening mechanism. Fig. 2 shows the schematic representation of a dislocation overcoming a periodic Peierls-Nabarro energy field in high-entropy alloys. The energy barriers are not uniformly distributed. This indicates that local chemical environments can influence their strength. Patriarca *et al.* [61] used the ‘modified’ Peierls–Nabarro

equation $\tau = \frac{1}{b} \max \left\{ \frac{dE_{\text{misfit}}}{du} \right\}$ (where E_{misfit} is the energy barrier function of dislocation displacements u)

to predict the critical resolved shear stress for slip in CrMnFeCoNi high-entropy alloy. This study also suggests a the strong influence of solute ordering on the Peierls–Nabarro stress.

A fundamental means to interrogate this structure is to establish the activation volume, $V = bA$ (b is the Burgers vector), for plastic deformation, which is related to the activation area, A , representing the area swept by a dislocation overcoming an obstacle. The shear flow stress has, in the formalism created by Seeger [62], an athermal and a thermal component, the former being unaffected by temperature and strain-rate. Examples are the grain size and larger obstacles to dislocations. Strain-rate changes and stress relaxation experiments can both be conducted to determine the activation volume, which is defined as:

$$V = bA = \frac{\partial \Delta G(\tau)}{\partial \tau} \Big|_T = M k T \frac{\partial \ln \dot{\varepsilon}}{\partial \sigma} \Big|_T, \quad (3.2.1)$$

where σ and τ are the normal and shear stresses, respectively, M is the Taylor factor (converting the shear to normal stresses), $\Delta G(\tau)$ is the free energy barrier, and $\dot{\varepsilon}$ is the strain rate.

Laplanche *et al.* [63] analyzed the deformation mechanisms in the Cantor alloy by means of stress relaxation experiments at different strains and temperatures, and for samples loaded at two strain rates. Characteristic relaxation results are shown in Fig. 14(a). As expected, the relaxation was dependent on the loading rate. The rate of decrease in stress was then used to calculate an apparent activation volume, from which V was obtained.

It is known that *fcc* metals have an activation volume dictated by forest dislocations, and their spacing l is equal to $\sim \rho^{1/2}$, where ρ is the dislocation density. In contrast, *bcc* metals have a much lower V , ($\sim b^3$), dictated by the Peierls-Nabarro stress. The activation volumes for the processes of solid-solution hardening (V_{ss}) and forest dislocation (V_f) cutting were combined into a single value, V , by Laplanche *et al.* [55]:

$$\frac{1}{V} = \frac{1}{V_{ss}} + \frac{1}{V_f} . \quad (3.2.2)$$

To evaluate this relationship, we note that the activation volume for forest dislocation cutting can be obtained from the activation area A , which is equal to the product of the dislocation spacing, l , and w , the width of the obstacle:

$$V_f = bwl = bw\rho^{-1/2}, \quad (3.2.3)$$

where ρ is the dislocation density equal to l^{-2} . The shear stress can be expressed by the Taylor equation for parabolic hardening [64]:

$$\tau_f = \alpha G b \rho^{1/2}, \quad (3.2.4)$$

where $\alpha = f(T, \dot{\gamma})$ is a parameter related to the effect of temperature and strain-rate on stress, and τ_f can be converted into a normal stress through M , an orientation parameter:

$$\sigma_f = M \tau_f . \quad (3.2.5)$$

Thus, one can obtain the activation volume:

$$V_f = \frac{M \alpha G b^2 w}{\sigma_f} . \quad (3.2.6)$$

The other term in Eqn. 3.2.2, V_{ss} , can be obtained from the solid-solution strengthening theory developed by Curtin and coworkers [65-67]:

$$V_{ss} = \frac{0.55M}{\sigma_{ss}} \Delta E_b , \quad (3.2.7)$$

when value of σ_{ss} is smaller than $0.5\sigma_{yo}$, where σ_{yo} is the apparent zero-temperature flow stress; ΔE_b is the activation barrier energy for solid solution.

Using values of V , shown in Fig. 14(b), in Eqn. 3.2.2 and substituting in the values from Eqns. 3.2.6 and 3.2.7, the flow stress at various plastic strains and temperatures can be calculated and compared to measured values, the latter being corrected for a grain size of $d = 17 \mu\text{m}$ to single crystal values. The line tension model was developed by Escaig *et al.* [68] based on the cross slip of dislocations in *fcc* metals. α is an empirical fitting scaling parameter to calculate the line tension energy $T = \alpha G b^2 / 2$ (where G is shear modulus and b is the Burgers vector) to match the atomistic predictions of stress dependence of cross slip energy barrier [69]. In general, increasing α will decrease the separation between partials. Fig. 14(b) shows the predicted stress decreases due to the increase of α , which was attributed to less twinning activity. Two values of the dislocation line parameter, 0.123 and 0.0625, were used. The calculated and experimental results show an excellent correspondence (Fig. 14(c)), leading Laplanche *et al.* [63] to conclude that these single-phase HEAs deform by the mechanisms that are not atypical of any other solute-strengthened *fcc* alloys, *i.e.*, by solid-solution, forest dislocations and grain-boundary strengthening, and that no new intrinsic deformation mechanisms are introduced by their complex structure.

3.3 Hardness

As a material's mechanical property related to strength, hardness represents the resistance to plastic deformation in a confined geometry. The hardness of HEAs can rise from $\sim 150 \text{ HV}$ [70] to $\sim 1200 \text{ HV}$ [71], depending on the synthesis method and composition, as reported by Diao *et al.* [72]. The Vickers hardness HV , (units of MPa) correlates approximately with the yield strength, σ_y , of metals through the Tabor [73] equation:

$$HV = C_V \sigma_y, \quad (3.3.1)$$

where C_V is a constant approximately equal to 3. A low-density $\text{Li}_{20}\text{Mg}_{10}\text{Al}_{20}\text{Sc}_{20}\text{Ti}_{30}$ HEA (Fig. 15), synthesized using mechanical alloying to form a single *fcc* phase, with an average grain-size about 12 nm, displayed a high microhardness of 606 HV due to its nanocrystalline structure [74]. This corresponds to a strength of ~2 GPa, a very high value. Zhang *et al.* [71] also obtained a high hardness for their $(\text{AlSiTiCrFeCoNiCuMo})\text{B}_{0.5}$ HEA, fabricated by laser cladding, containing a lath-like martensite phase. The martensite phase nucleates during the rapid solidification, such that this alloy reaches a high Vickers hardness of 1122 HV both due to the presence of martensite and to interstitial-solute hardening.

3.4. Hall-Petch relationship

Most metals and alloys exhibit grain-size strengthening due to the boundaries that act as obstacles to dislocations. Such is also the case of HEAs, as has been demonstrated in a few studies. A CrMnFeCoNi *fcc* HEA was annealed at various temperatures to achieve different grain sizes and thereby examine its grain growth behavior [75]. The growth kinetics constant C for the grain-growth equation $d^n - d_0^n = Ct$ (where d and d_0 are the final and initial grain sizes, respectively, n is a grain-growth exponent found to be ~3, and t is time) can be expressed as [76, 77]:

$$C = A_0 \exp(-Q / RT), \quad (3.4.1)$$

where A_0 is a constant, R is the gas constant, and Q is the activation energy for grain growth at the absolute temperature T . The activation energy, Q , of the HEA can be calculated easily from the plot of $\ln(d^3 - d_0^3 / \text{time})$ against $(1/T)$. Fig. 16(a) shows that the value of Q for this alloy is about $321.7 \text{ kJ.mol}^{-1}$; interestingly, this is similar to that ($317.5 \text{ kJ.mol}^{-1}$) for the diffusion-rate of Ni in CrMnFeCoNi HEA. This suggests that the grain growth-rate of the HEA is related to the diffusion rate of the slowest element.

Hall-Petch slopes for the CrMnFeCoNi alloy and 304 stainless steel [78] are shown in Fig. 16(b) and compared to the Hall-Petch slopes of pure Fe and pure Ni [69]. They all follow the classical Hall-Petch relationship:

$$\sigma_y = \sigma_{y0} + k_{HP} d^{-1/2} , \quad (3.4.2)$$

where σ_y is the yield stress, d is the grain size and k_{HP} is the Hall-Petch coefficient. The microhardness HV values for the CrMnFeCoNi alloy [75] in Fig. 16(b) were converted to equivalent yield stress values using the equation $HV=3\sigma_y$ for comparison. The value of k_{HP} for the CrMnFeCoNi HEA, determined by the slope of the curve, is $226 \text{ MPa} \cdot \mu\text{m}^{-1/2}$. By comparison, Otto *et al.* [79] reported that the slope for Hall-Petch relationship of the Cantor alloy was $494 \text{ MPa} \cdot \mu\text{m}^{-1/2}$ in uniaxial tensile tests. The Hall-Petch slope is comparable to other alloys such as stainless steel, as shown in Fig. 16(b). Thus, like virtually all metals, these HEAs follow the Hall-Petch relationship when their grain sizes are in the micrometer-scale.

An inverse Hall-Petch relationship has been widely reported for nanocrystalline materials [80]. Tschopp *et al.* [81], among others, pointed out that the volume fraction of inter-crystal regions such as grain boundaries and triple junctions increases with decreasing grain size using the tetrakaidecahedron as a grain configuration shown in Fig. 17. By varying the thickness of the grain-boundary from 1 nm (depicted by the thick line), to 0.5 nm (shown by the dashed lines), the volume fraction of inter-crystal regions decreases accordingly. This effect becomes more pronounced as the grain size decreases and becomes nanocrystalline ($<100 \text{ nm}$). For example, Malloy and Koch [82] and Abrahamson [83] reported the reduction in the Hall-Petch slope in iron for grain sizes between 250 nm and 25 nm, which was modeled using a core-and-mantle model by Meyers and Ashworth [84]. The basic idea is that the volume fraction of grain-boundary regions increases when grain sizes decrease. This model was expressed as:

$$\sigma_y = \sigma_B + 8k_{MA}(\sigma_{Gb} - \sigma_B)d^{-1/2} - 16k_{MA}^2(\sigma_{Gb} - \sigma_B)d^{-1} , \quad (3.4.3)$$

where σ_y is the yield stress, σ_B is the flow stress in the grain interior, σ_{Gb} is flow stress in the grain-boundary region (after compatibility stresses produce enhanced hardening), and k_{MA} is a constant parameter. The flow stress (σ_{Gb}) in the grain-boundary region was assumed to have higher value than that (σ_B) in the grain interior because of more complex compatibility requirements leading to additional cross-slip. The second term in the Eqn. 3.4.3 is negative and represents a decrease in the slope, which becomes more important as d decreases [199]. At a critical value of d , the slope becomes negative. The model compares well with experimental results. However, the inverse Hall-Petch effect [85-87] still needs to be examined for nanostructured HEAs. A single-phase *fcc* nanocrystalline Al_{7.5}Co₂₅Fe₂₅Ni₂₅Cu_{17.5} HEA was found to display a flat stress-strain curve due to reduced dislocation activity after an initial plastic deformation stage of rapid work hardening [88]; this behavior is similar to other nanocrystalline materials [80]. The mechanical properties of nanocrystalline HEAs need to be explored to examine whether an inverse Hall-Petch phenomenon actually occurs. In other metals, grain sizes below 15 nm are required.

3.5 Wear

The wear performance of four HEA alloys was examined by adding different atomic fractions of Al and Ti to CrCoNi alloys [89]: Ti_{9.1}Cr_{18.2}Fe_{18.2}Co_{27.3}Ni_{27.3}, Al_{3.5}Ti_{8.8}Cr_{17.5}Fe_{17.5}Co_{26.3}Ni_{26.3}, Ti_{16.7}Cr_{16.7}Fe_{16.7}Co₂₅Ni₂₅, and Al_{3.2}Ti_{16.1}Cr_{16.1}Fe_{16.1}Co_{24.2}Ni_{24.2}. The wear properties of these HEAs were studied using the pin-on-disk testing method in the dry condition. The anti-wear materials, SUJ2 bearing steel and SKH51 high-speed tool steel, were chosen for comparison. The wear performance of the HEAs was described by the wear resistance parameter: $W_r = L / \Delta V$, where W_r is the wear resistance, and ΔV (measured by dividing the weight change by the density of the sample) is the volumetric loss after

sliding a specific distance L for the pin-on-disk testing. Fig. 18 compares the wear resistance and hardness of the six tested alloys. The $\text{Al}_{3.2}\text{Ti}_{16.1}\text{Cr}_{16.1}\text{Fe}_{16.1}\text{Co}_{24.2}\text{Ni}_{24.2}$ HEA has the highest wear resistance parameter of the four tested alloys, approximately twice that of the $\text{Ti}_{16.7}\text{Cr}_{16.7}\text{Fe}_{16.7}\text{Co}_{25}\text{Ni}_{25}$ HEA. As expected, HEAs with higher hardness ($\text{Al}_{3.2}\text{Ti}_{16.1}\text{Cr}_{16.1}\text{Fe}_{16.1}\text{Co}_{24.2}\text{Ni}_{24.2}$ and $\text{Ti}_{16.7}\text{Co}_{25}\text{Cr}_{16.7}\text{Fe}_{16.7}\text{Ni}_{25}$) had higher wear resistance than the softer alloys ($\text{Ti}_{9.1}\text{Cr}_{18.2}\text{Fe}_{18.2}\text{Co}_{27.3}\text{Ni}_{27.3}$ and $\text{Ti}_{16.7}\text{Cr}_{16.7}\text{Fe}_{16.7}\text{Co}_{25}\text{Ni}_{25}$). Although the hardness of $\text{Al}_{3.2}\text{Ti}_{16.1}\text{Cr}_{16.1}\text{Fe}_{16.1}\text{Co}_{24.2}\text{Ni}_{24.2}$ is similar to that of SUJ2 steel and significantly lower than that of SKH51 steel, its wear resistance parameter is much higher than the two reference anti-wear alloys. Compared with the reference steels, the excellent wear resistance of $\text{Ti}_{16.7}\text{Cr}_{16.7}\text{Fe}_{16.7}\text{Co}_{25}\text{Ni}_{25}$ and $\text{Al}_{3.2}\text{Ti}_{16.1}\text{Cr}_{16.1}\text{Fe}_{16.1}\text{Co}_{24.2}\text{Ni}_{24.2}$ HEAs appears to be a result of the lower high-temperature softening rates of the HEAs and their greater oxidation resistance.

The wear resistance can also be associated with the high work-hardening rate, in a manner similar to the traditional Hadfield Manganese steel, used in the mining industry for applications requiring high impact and wear resistance (*i.e.*, crushers and grinders), cement mixers, rock crushers, railway switches and crossings, and tractor treads. The surface layer, under the action of minerals, rocks, or train wheels, undergoes continuous hardening without crack initiation, and thus maintains its structural integrity. This is an important characteristic of HEAs that can make them potential candidates for such applications.

3.6 Tensile behavior

Alloying of *fcc* metals usually results in a lowering of the stacking-fault energy. Prime examples are austenitic stainless steels, with compositions of nominally ~18 wt.% Cr and 8 wt.% Ni. As noted above, the first HEAs were *fcc* equiatomic solid solutions. Newer generations of HEAs encompass a vast landscape which includes *fcc*, *hcp* and *bcc* single-phase alloys as well as two-phase metallic alloys and ceramics. Mechanical properties are dependent on the elements that comprise the HEAs as well as

on the structure of the principal phases. The formation of intermetallic compounds (R, σ , and Laves phases) can naturally have a marked effect on their tensile behavior. Many of these phases are brittle and act as initiation sites for failure.

3.6.1 Strain hardening

The term $\frac{d\sigma}{d\varepsilon}$ is used to describe the strain-hardening ability of materials. If an alloy has low $\frac{d\sigma}{d\varepsilon}$, it will readily neck in tension. The Considère criterion is a simple representation of this response. If a high $\frac{d\sigma}{d\varepsilon}$ is combined with a high flow stress, there is a high probability that the alloy has also a high toughness. These characteristics are not unique to HEAs and indeed a number of successful *fcc* alloys benefit from this. As noted above, as early as 1880 Sir Robert Hadfield developed one of the first successful iron-based alloys, a 10-13 wt.% Mn steel which became globally known as Hadfield Manganese steel. With its high yield stress and extraordinary strain-hardening ability, a number of favorable mechanical properties result. Hadfield steels [90] accomplish this by an *fcc* structure, where the high yield stress is the result of solid-solution strengthening by the Mn atoms [91], and the high strain-hardening effect derives from the interaction of dislocations with solid-solution carbon atoms.

Another example of the superior work-hardening ability of low stacking-fault (SFE) *fcc* alloys are the twinning-induced plasticity (TWIP) steels [92-94]. Specifically, mechanical twinning during deformation can provide barriers for dislocation motion causing a decrease in the dislocation motion path and leading to an increase of dislocation densities inside the twins. Steinmetz *et al.* [95] attributed the high strain-hardening rate of TWIP steels to the interaction between dislocations and deformation twins. Some HEAs benefit from the same favorable work hardening [96]. Gludovatz *et al.* [15] revealed that the continuous strain-hardening of the CrMnFeCoNi HEA at both room and cryogenic temperature

was caused by a combination of planar dislocation slip and mechanical nano-twinning. Although twinning does not have a dominant role during tensile deformation at room temperature and at low strain-rates, the Cantor alloy retains a high strain-hardening rate and shows excellent work-hardening ability, as can be seen by comparing it with the other alloys in Fig. 19. This is in part associated with solid-solution hardening and cutting forest dislocations.

The Considère criterion describes the onset of the instability during the tensile deformation and has the following form:

$$\left(\frac{\partial \sigma}{\partial \varepsilon} \right)_{\dot{\varepsilon}} \leq \sigma \quad (3.6)$$

where σ is the true stress, and $\dot{\varepsilon}$ is the strain-rate [1]. The subsequent increase in the strain-hardening rate after its initial decrease was clearly seen in both the Cantor alloy and twin-induced plasticity (TWIP) steel in Fig. 19, and can be attributed to twinning hardening. The evolution of $d\sigma/d\varepsilon$ with true strain ε for the alloys discussed above and transformation-induced plasticity (TRIP), dual-phase (DP) (TRIP-DP) $\text{Cr}_{10}\text{Mn}_{30}\text{Fe}_{50}\text{Co}_{10}$ high-entropy steel [97, 98] is presented in Fig. 19, together with the stress-strain curves; they will be discussed in the following sections.

3.6.2 Strength and ductility trade-off

There is generally a strength–ductility trade-off effect for most metals [2]; increasing strength invariably leads to loss in ductility, which is clearly undesirable for structural materials. Usually a reduction in grain size into nanocrystalline region leads to a reduction in ductility because of the increasing presence of sinks of dislocations at the grain boundaries, decreasing their build-up and associated hardening. In order to overcome this, Lu *et al.* [99-101] synthesized nano-twinned copper with high ductility incorporating excellent strain-hardening ensured by twin boundaries interacting with dislocations and losing their cohesiveness during plastic deformation. Furthermore, Lu *et al.* [102, 103]

developed gradient materials with a combination of coarse-crystalline and nanocrystalline gradient structures leading to increased ductility at a relatively high strength [104]. To similarly defeat the strength/ductility tradeoff, Yang *et al.* [105] introduced high-density ductile multicomponent intermetallic nanoparticles ($\text{Ni}_{43.3}\text{Co}_{23.7}\text{Fe}_8)_3(\text{Ti}_{14.4}\text{Al}_{8.6}\text{Fe}_2)$ with coherent grain boundaries in a complex $(\text{FeCoNi})_{86}\text{-Al}_8\text{Ti}_6$ alloy. The material achieves a superb strength of 1.5 GPa and 50% ductility in tension at room temperature. The Ti doping in this alloy promotes the Ti/Al ratio, which can increase the antiphase boundary energy and leads to a higher work-hardening because of the activation of dislocation cross-slip [106]. In addition to precipitation hardening, the dislocation microband-induced plasticity, resulting in higher back stress hardening and forest dislocation hardening, is mainly attributed to the unusual high strain-hardening rate in this high-entropy alloy.

Hadfield steel has the *fcc* structure which, as noted above, confers its excellent work hardening, and consequently, superior ductility. The strengthening is due to the carbon atoms (~1 wt.% C) which change position during deformation and confer dynamic strain aging to the structure [107]. With a similar composition but more Mn (~20 wt.%), and additions of Al (<3 wt.%), Si (<3 wt.%), and C (<1 wt. %), TWIP steels undergo significant twinning during deformation which blocks dislocation glide and enhances the general resistance to deformation, thereby increasing work hardening. These steels can reach ultimate tensile strengths exceeding 1 GPa with tensile ductilities over 85%.

In the HEA domain, Li *et al.* [97, 108-110] reported a (transformation-induced plasticity and dual- phase) TRIP-DP $\text{Cr}_{10}\text{Mn}_x\text{Fe}_{80-x}\text{Co}_{10}$ steel, which exhibits enhanced ductility while retaining a high tensile failure strength (in the range of 800 MPa). Moreover, the excellent strain-hardening ability is enabled by a combination of dislocation work hardening in the stable phase and further hardening due to phase transformation, specifically from *fcc* to *hcp*. Fig. 20(a) shows the tensile behavior of the TRIP-DP steel with its excellent properties in terms of the strength–ductility trade-off. In comparison to the

Hadfield steel (Fe-11.4 at.% Mn-1.13 at.% C-0.2 at.% Si-0.17 at.% Ni-0.16 at.% Cr-0.08 at.% Mo) [107], and the (twinning-induced plasticity) TWIP steel (Fe-22 wt.% Mn-0.6 wt.% C) [111], the Al_{0.3}CrFeCoNi HEA [96, 112] and the CrMnFeCoNi HEA alloys [15] show promising mechanical properties with nano-twinning as a prominent deformation mechanism at lower temperatures. There is a common trend in these alloys; they are all *fcc* solid solutions, which can provide solid-solution strengthening and improved ductility by easy motion of dislocations. Fig. 20(b) summarizes the simultaneous high strength (from solid-solution hardening and boundary strengthening with increasing interface densities of twins and new phases) and good ductility (from dislocation slip, mechanical twinning, and phase-transformation) achieved in the TRIP-DP Cr₁₀Mn_xFe_{80-x}Co₁₀ steel.

Raabe and coworkers [97] developed high-entropy ‘steels’ containing between 20 and 50 at.% Fe. These steels have an attractive combination of strength and ductility that exceeds that of the best TRIP and TWIP steels. Fig. 21(a) shows the performance of high-entropy steels in the ultimate strength-ductility space. These steels utilize the transformation from *fcc* to *hcp* martensite during plastic deformation to enhance work hardening, as shown in Fig. 21(b). In combination with a grain size reduction to 4.4 μm , the alloy Cr₁₀Mn₂₀Fe₅₀Co₁₉ shows an ultimate tensile strength of ~900 MPa with ductility ~70%. However, a potential problem with utilizing the TRIP effect to achieve enhanced work hardening and hence ductility in HEAs is that the product phase, in the above case the *hcp* phase, may not have good intrinsic toughness properties. A excellent case in point is the *in-situ* transformation of retained austenite under load in ultrahigh-strength low alloy steels, where the formation of untempered martensite can lead to tempered martensite embrittlement [205].

He *et al.* [113] demonstrated precipitation hardening in a CrFeCoNi HEA with the appearance of a new reinforcing phase, L1₂-Ni₃(Ti, Al); this was accomplished by small additions of Ti and Al. Using thermomechanical processing, excellent tensile properties of this HEA were obtained at room

temperature, benefiting from the precipitation hardening. Varvenne *et al.* [114] systematically studied strengthening mechanisms in a series of N ($2 \leq N \leq 5$) component *fcc* HEAs. As the atoms are randomly distributed, strengthening was proposed to mainly result from dislocation interactions with the randomly distributed local solutes. These authors found that: (i) the strength of HEAs did not simply depend on the number of components N , and was not maximized by the increase of N , and (ii) the high strength can originate from the chemical and structural fluctuations in HEA materials.

In CrCoNi-based HEAs, the achievement of both strength and ductility, which is exceptional in these alloys at cryogenic temperatures due to the occurrence of deformation twinning, can also be impressive at ambient temperatures in the absence of twinning. A case in point is the CrMnFeCoNi HEA which displays little to no deformation twinning at room temperature but still has a tensile strength exceeding 700 MPa with a tensile ductility well above 50%. The basic reason for this damage-tolerance is that these alloys have low stacking fault energies (SFE ~ 20 mJ.m⁻²) coupled with a high lattice friction stress; the latter follows from the apparently random distribution of the solutes, which form a true solid solution down to the atomic scale leading to a relatively high resistance to the motion of dislocations [115].

Deformability in the Cantor alloy at ambient temperatures (in the absence of twinning) has been shown by Zhang *et al.* [115] to be achieved by the initial easy motion of the leading Shockley partial dislocations, resulting in the formation of stacking faults. This appears to provide a mechanism for the alloy's ample ductility. As the applied stress increases, perfect dislocations are generated but their motion is extremely hard since they slip through intersecting localized planar-slip bands containing a variety of closely packed dislocations. The planar slip-bands work as strong barriers for partial dislocation motion, providing the hardening mechanism. Strengthening can also be produced by parallelepiped-shaped sessile volume defects that can form in this alloy by the interaction of partial

dislocations slipping on multiple planes that impede the motion of other dislocations. This synergy of deformation mechanisms provides the primary source of this alloy's combination of high strength and ductility, which of course can be further enhanced at lower temperatures where the higher strength can additionally activate deformation nano-twinning

3.6.2.1 Lattice distortion and stacking-fault energy effect

Though the atomic misfit strain in CrFeCoNi and CrMnFeCoNi HEAs is not that significant, large concentrations of different kinds of solutes can still lead to a severe lattice distortion effect. Lattice distortion, which is the same as the atomic-size mismatch parameter, can be expressed as [29]:

$$\delta = \left\{ \sum_{i=1}^n c_i \left[1 - \left(\frac{r_i}{\bar{r}} \right)^2 \right] \right\}^{1/2}, \quad (3.6.1)$$

where c_i is chemical proportion of the element, r_i is the Goldschmidt radius for a specific element and \bar{r} is the average radius for all the elements.

Fig. 22(a) shows atomic misfit for a series of HEAs. The corresponding lattice-distortion values of the alloys are plotted in Fig. 22(b), showing that the value for $\text{Al}_{2.44}\text{Cr}_{24.4}\text{Fe}_{24.4}\text{Co}_{24.4}\text{Ni}_{24.4}$ HEA is the highest. The severe lattice-distortion effect of HEAs has been discussed in Section 1.2; it appears that the lattice-distortion in solid solutions leads to the decrease in the activation energy for dislocation nucleation (Fig. 22(c)). As a consequence, the energy barrier for dislocation nucleation is lower in HEAs than that in conventional alloys with one principal element; additionally, the values of stacking-fault energy (SFE) and twin-boundary energy are reduced. The role of different kinds of solutes in decreasing the SFE in solid solutions has been widely examined. For example, on the one hand, Rohatgi *et al.* [116] reported that adding Al to pure Cu decreases the SFE of Cu-Al alloy, which was also reported by Meyers *et al.* [117]. On the other hand, Fig. 22(d) shows anomalous behavior of the coarse-grained (CG) $\text{Al}_{0.1}\text{CrFeCoNi}$ HEA with very low activation volumes reported by Mishra *et al.* [29], about one fourth

of that for the traditional CG alloys. Since the slip planes for dislocation motion can be roughened and distorted by solutes, the area swept during the stress change decreases, leading to the very low activation volume. This implies that the area swept by a dislocation in an HEA during a stress change is much smaller, even as small as that of ultrafine-grained materials. Thus, solutes in HEAs can be regarded as a dampening factor for dislocation motion.

The SFEs of equiatomic *fcc* metals from pure Ni to CrMnFeCoNi HEA were established based on both XRD experiments and density functional theory (DFT) simulations by Zaddach *et al.* [118]. The SFE was estimated by the expression [119, 120]:

$$\gamma = \frac{K_{111}\omega_0 G_{(111)} a_0 A^{-0.37}}{\pi\sqrt{3}} \cdot \frac{\varepsilon^2}{\alpha}, \quad (3.6.2)$$

where $G_{(111)}$ is the shear modulus in the (111) plane, $K_{111}\omega_0$ is considered to be a constant equal to 6.6 for *fcc* metals, a_0 is the corresponding lattice constant, A is the Zener elastic anisotropy equal to $2C_{44}/(C_{11}-C_{12})$, ε^2 is the mean square microstrain, and α is the stacking-fault probability. The SFE of the CrFeCoNi and CrMnFeCoNi HEAs have been measured by x-ray diffraction as about 20 mJ.m^{-2} and 25 mJ.m^{-2} [121], respectively, as shown in Fig. 23. These values are significantly lower than that of pure Ni (130 mJ.m^{-2}) and FeNi alloys. Thus, by altering the chemical composition of HEAs, SFE can be reduced to extremely small values, which can influence their mechanical properties. This creates the possibility designing low SFE *fcc* HEAs with desired ductility by tailoring the twin-induced plasticity.

The stacking-fault energy fluctuates significantly in Ni-2 at.%Fe alloy and Ni-20 at.% Fe-26 at.% Cr alloy [122], as shown in Fig. 24(a). The distance between the partial dislocations in the solid solution varies along the dislocation line, indicating local differences in the stacking fault energy, which is referred as “local SFE”. Such “local SFE” values have been calculated through molecular dynamics, using the embedded-atom method inside a $30\times30\times30$ supercell, where all atoms are randomly distributed

and surface unit cells are shown in Fig. 24(b); the potential energies of all solutes inside a column, with the cross section of the fault plane, are summed and divided by the area. A single {111} plane is created by the slip of a 1/6 [211] partial dislocation to generate an intrinsic stacking-fault. Thus, the excess energy of this geometry per unit fault area is established to be the stacking-fault energy. Since the chemical composition can change along the fault plane in the “local” area, the “local SFE” values can be very small and even negative at several sites even though the average SFE remains positive, as seen in Fig. 24(c). A negative “local SFE” implies that the specific stacking-fault sequence for *fcc* HEAs stays in a more favorable and stable state, compared with their perfect packing sequence. Figs. 25(a,b) show the increased microhardness with increase of the lattice distortion and the decrease of the stacking-fault energy. But this may not be applied to all of high-entropy alloys [123].

3.6.2.2 Twinning effect

The incidence of deformation twins depends on the stacking-fault energy and their frequency increases with the decrease in SFE. The nucleation of mechanical twins requires the emission of twinning dislocations along specific planes parallel to the coherent twin boundary. These twinning dislocations are generated by the decomposition of partial dislocations on parallel planes [1]. Meyers *et al.* [124] examined the relationship between the twinning stress and temperature for several monocrystalline or polycrystalline metals, and concluded that the twinning stress was insensitive to the temperature. In addition, a constitutive equation was developed to predict the critical stress for twinning as a function of external (temperature, strain rate) and internal (grain size, stacking-fault energy) parameters. Meyers *et al.* [124] proposed that the twinning happens when twinning stress σ_T is equal to slip stress, σ_S : $\sigma_s = \sigma_T$. For *fcc* metals, the twinning stress has been expressed as [125]:

$$\sigma_T = \alpha_T \left(\frac{\gamma_{SF}}{Gb} \right)^{1/2}, \quad (3.6.3)$$

where γ_{SF} is the stacking-fault energy, G is the shear modulus, α_T is an adjustable parameter and b is Burgers vector. For the Cantor HEA, the stacking fault energy is measured as 25 mJ.m^{-2} , G is 80 GPa , the lattice parameter is measured as 0.36 nm , and $\vec{b} = \frac{1}{6} \langle \bar{1}\bar{1}2 \rangle$ (the Shockley partial dislocation) [55].

Laplanche *et al.* [126] studied the critical stress for twinning in the CrMnFeCoNi HEA by examining its microstructure evolution under tension. Twinning was found to occur at a stress of $\sim 700 \text{ MPa}$. A good fit for Eqn. 3.6.3 can be obtained with $\alpha_T = 16 \text{ GPa}$. However, there obviously exists some variation of twinning stress for the Cantor alloys prepared by different methods.

The slip response of this Cantor alloy was modeled through the Zerilli–Armstrong equation [127] for *fcc* metals [128, 129] as:

$$\sigma_s = \sigma_G + k_{HP} d^{-1/2} + C_1 \varepsilon^\varpi \exp \left[-C_2 T + C_3 T \ln \frac{\dot{\varepsilon}}{\dot{\varepsilon}_0} \right], \quad (3.6.4)$$

where $\sigma_G + k_{HP} d^{-1/2} \approx 450 \text{ MPa}$ (σ_G is the athermal component of stress, and k_{HP} is the Hall-Petch slope) as discussed in the Section 3.4, $\varpi = 0.76$, $C_1 = 2000 \text{ MPa}$, $C_2 = 3.82 \times 10^{-3} \text{ K}^{-1}$, and $C_3 = 4.68 \times 10^{-4} \text{ K}^{-1}$, for the Cantor alloy [128]. Other constitutive equations can also describe the tensile response of these alloys, but the Zerilli-Armstrong equation has a strong dislocation foundation. The slip-twinning transition curves (using true strains $\varepsilon = 0.1, 0.5$ and a reference strain-rate $\dot{\varepsilon}_0 = 10^3 \text{ s}^{-1}$) for this alloy are constructed in Fig. 26(a) by setting $\sigma_T = \sigma_s$. Two domains of slip and twinning are defined in the strain rate-temperature plot. Thus, at lower temperatures and higher strain-rates, deformation twinning takes a dominant role for this alloy. Fig. 26(a) shows that either an increase in strain-rate or a decrease in temperature will increase the propensity for twinning. The predictions of Fig. 26(a) are corroborated by observation. The red arrow shows that dislocations prefer to slip at low strain-rates and high temperature. In comparison, twinning happens at high strain-rates and low temperatures. In addition, twinning often

happens at a larger strain when dislocation slip becomes difficult. This is why there are two slip-twinning transition curves shown in Fig. 26(a): one at 0.1 and one at 0.5.

The relationship between the critical twinning stress and the radius of the nucleus of mechanical twins was also calculated by Meyers *et al.* [124] using the Eshelby inclusion theory. The stress acting on the twin embryo produces an elastic distortion, which leads to the change of total free energy, resulting from a combination of twin-matrix interfacial energy and the energy needed for the nucleation of the twin. The latter can be treated as an ellipsoidal Eshelby inclusion. Once the radius of the twin reaches the critical size for nucleation (the maximum in the free energy), it grows in a stable manner. The critical radius of the twin embryo is proportional to the twin-boundary energy γ_{TB} and specific twin stress:

$$r_c = \frac{5\pi}{4} \frac{G\gamma_{TB}}{(\tau_{twin})^2} , \quad (3.6.5)$$

where the shear modulus G is 80 GPa [55] and the twin-boundary energy $\gamma_{TB} = 2\gamma_{SF} = 50 \text{ mJ.m}^{-2}$ for the Cantor alloy [121]. The critical twin nucleus size as a function of the applied stress is depicted in Fig. 26(b). As noted in Section 3.6.2.1, the stacking-fault energy of HEAs is relatively low. This results in an easy nucleation of deformation twins. Zhang *et al.* [39] even reported calculations of a negative SFE in the *fcc* CrCoNi and CrFeCoNi alloys (at 0 K) through first-principles calculations. They discovered that the negative SFEs was caused by the energetic preference of *hcp* stacking, resulting in the metastable *fcc* structure at low temperatures. Experimental measurements of the SFE for these alloys are invariably positive though; as discussed by Ding *et al.* [33] this is believed to be the result of some degree of local chemical ordering in the real materials. The easy formation of deformation twins in the Cantor alloy at lower temperatures, not to mention the CrCoNi alloy and TWIP and TRIP steels discussed in Section

3.6.2 (Fig. 20), serves to confer an excellent balance of strength and ductility to these materials which can be further enhanced at cryogenic temperature where twinning may be even more predominant.

Christian *et al.* [130] and later Zhu *et al.* [131] reviewed nucleation and growth mechanisms of deformation twinning. The formation of deformation twins for nanocrystalline *fcc* metals is well established, as depicted in Fig. 27. This is based on the mechanism originally proposed by Cohen and Weertman [132]. The twinning dislocations are all Shockley partials gliding on the (111) slip planes with Burgers vectors $\mathbf{b}_1 = B\delta = a/6[2\bar{1}\bar{1}]$, $\mathbf{b}_2 = A\delta = a/6[\bar{1}2\bar{1}]$, and $\mathbf{b}_3 = C\delta = a/6[\bar{1}\bar{1}2]$. These are three equivalent Shockley partials, as shown by the Thompson tetrahedron in Figs. 27(a,b). Also, there also exist three partial dislocations with opposite Burgers vectors, $-\mathbf{b}_1$, $-\mathbf{b}_2$, and $-\mathbf{b}_3$. A deformation twin can be created by the continuous glide of Shockley partials on (111) parallel slip planes. Fig. 27(c) shows the formation of a four-layer twin through the slip of partial dislocations with the same Burgers vector \mathbf{b}_1 ; additionally, in Fig. 27(d) a four-layer twin with the same stacking structure as in Fig. 27(c) is formed by the slip of four partials with a combination of three Burgers vectors (\mathbf{b}_1 , \mathbf{b}_2 , and \mathbf{b}_3) on (111) slip planes.

Such deformation mechanisms in the Cantor alloy were examined by Otto *et al.* [79]. Fig. 28(a) reveals the presence of deformation twins in the tensile sample at a strain ~0.2 at 77 K. The high-resolution TEM image in Fig. 28(b) concentrates on an area where two deformation nano-twins with a thickness ~2.5 nm are observed (inside the corresponding insert). Fig. 28(d) shows the corresponding diffraction pattern indices for Fig. 28(c). The twinning elements in Fig. 28(e) can be described by $K_1 = (\bar{1}\bar{1}\bar{1})$; $\eta_1 = [\bar{1}12]$; $K_2 = (\bar{1}11)$; $\eta_2 = [\bar{1}12]$. These twinning elements are indicated on the [110] projection; white-color indices appear as the lattice in region 1 while red-color indices appear as the

lattice in region 2. This similar twinning behavior was also found in other *fcc* crystals and is reported in the classic paper by Christian and Mahajan [130].

Not only does deformation twinning influence the mechanical behavior of materials, but also annealing twins can make a difference and provide barriers for slip. Lu *et al.* [101] demonstrated how nano-twinned copper produced by pulsed electrodeposition can exhibit enhanced ductility and Zhang *et al.* [133] showed how the fatigue resistance can be enhanced by these boundaries, that are somewhat permeable to dislocations. In HEAs that have low SFEs, there is often also a high density of annealing (or recrystallization) twins. The formation of annealing twins can be achieved by grain growth, grain encounter, stacking errors, and stacking-fault packets at migration boundaries [200-201] and their frequency increases with decreasing stacking-fault energy. Figs. 29 (a,b) show the microstructure of CrCoNi and Al_{0.3}CrFeCoNi alloys with annealing twin boundaries. These twins often have a configuration of two parallel boundaries. A model was proposed by Meyers *et al.* [134,135] for the formation of annealing twins, where an annealing twin can emerge from one side of a grain boundary, and then propagate into the interior of grain by the migration of the noncoherent twin boundary, as illustrated in Figs. 29 (c,d). The noncoherent boundary can be represented by arrays of the parallel Shockley dislocations of opposite sign, so that the global Burgers vector is zero, as shown in Fig. 29(e); propagation of the twin proceeds by the migration of these partial dislocations into the grain. The global strain is zero, in contrast with deformation twins. The density of these twins can be controlled through grain-boundary engineering. Meyers and McCowan [134] showed that different thermomechanical processes can result in different twin boundary densities. However, the contribution of annealing twins to the deformation of HEAs has not as been quantified. It is of the authors' opinion that their role is fairly inconsequential.

3.7 Fracture toughness

The toughness of a material is a quantitative measure of resistance to fracture and is ideally established at the critical point where the initiation of unstable cracking occurs [136]. In plane strain under small-scale yielding conditions, the critical value of the linear-elastic stress-intensity factor, K_{lc} , can be measured at the onset of crack initiation and is termed the "plane-strain fracture toughness." In addition, the critical values of the J -integral, J_{lc} , or the crack tip opening displacement, (δ_i or δ_{lc}) can describe the (crack-initiation) toughness in an elastic-plastic material [137-141]. For the small-scale yielding condition, these parameters are related by:

$$J_{lc} = \frac{K_{lc}^2}{E'} = \lambda \delta_i \sigma_0 . \quad (3.7.1)$$

σ_0 is the flow stress, E is the elastic (Young's) modulus ($E' = E$ in plane stress or $E/(1 - \nu^2)$ in plane strain, where ν is Poisson's ratio), and λ (varying from 0.3 to 1) is a constant depending on the yield stress, work-hardening exponent, and whether plane stress or plane strain conditions are relevant. Where fracture instability is not coincident with crack initiation, *e.g.*, under non-plane strain or elastic-plastic (more correctly, nonlinear-elastic) conditions, subcritical crack propagation can be characterized by the crack-growth resistance curve, or R-curve, *e.g.*, the $K_R(\Delta a)$ or $J_R(\Delta a)$ resistance curve, as shown in Fig. 30(a) [142].

Fig. 30(b) shows how strength and fracture behavior can be considered in terms of intrinsic (plasticity) and extrinsic (shielding) toughening mechanisms associated with the crack extension [2, 143]. The illustration shows the competition between intrinsic toughening mechanisms, which act ahead of the crack tip to make fracture more difficult, and extrinsic shielding mechanisms, which are active at, or behind, the crack tip. Intrinsic toughening is primarily driven by plastic deformation; in many classes of materials, especially metallic materials, this results both in an increase in the crack-initiation and

crack-growth toughness. At the same time, the extrinsic toughening mechanisms can decrease the local stress and strain fields near the crack tip, by such mechanisms as crack deflection and crack bridging which carry loads that would otherwise be used to further crack propagation; this invariably results in rising R-curve behavior.

Fig. 31(a) shows the initial microstructure of the fully recrystallized Cantor HEA (with a $\sim 6 \mu\text{m}$ grain size) containing a high density of annealing twins by virtue of its low stacking-fault energy. SEM-EDX and XRD analysis demonstrate that it is a single *fcc* phase with elements in equimolar proportions. With the decrease of temperature from 293 K to 77 K, the yield strength σ_y of this alloy shows a significant increase (by $\sim 85\%$) to 795 MPa; the ultimate tensile strength σ_{uts} also exhibits an impressive increase (by $\sim 70\%$), to 1280 MPa. Moreover, the tensile ductility (strain to failure, ε_f) increases by $\sim 25\%$ to ~ 0.7 , and its high work-hardening ability is retained at cryogenic temperature.

To understand the origin for the marked increase in damage-tolerance of the Cantor alloy at cryogenic temperatures, Gludovatz *et al.* [15] evaluated its fracture toughness using precracked and side-grooved compact-tension specimens, to determine the J_R crack-resistance curves at temperatures between ambient and liquid-nitrogen temperatures; stress-intensity K values can be back-calculated from the J measurements using nonlinear-elastic fracture mechanics (Eqn. 3.7.1). Fig. 31(b) shows that a J_{Ic} crack-initiation fracture toughness of 250 kJ.m^{-2} is measured at 293 K, equivalent to a K_{Jlc} toughness of $217 \text{ MPa}\cdot\text{m}^{1/2}$. Although the strength of this alloy increases significantly with a lowering of the temperature, the K_{Jlc} toughness values remain well above $210 \text{ MPa}\cdot\text{m}^{1/2}$ at 200 K and at 77 K, representing an extremely high toughness for a metallic material.

The fracture surfaces of the samples examined at 293 K and 77 K were analyzed using backscattered electron (BSE) microscopy (Fig. 32(a)) and electron backscatter diffraction (EBSD)

analysis (Fig. 32(b)). Fig. 32(c) shows the presence of nanoscale deformation twins near the crack tip, in addition to planar dislocation slip within the grains. The nano-twinning is critical to maintaining a high strain-hardening rate, especially at cryogenic temperatures; in turn, this ensures the high tensile ductility of the Cantor alloy, together with a higher strength at cryogenic temperatures, and is responsible for its extraordinary damage-tolerance.

Furthermore, using *in-situ* atomic/nanoscale TEM, Zhang *et al.* [144] revealed that the excellent toughness of the Cantor alloy at room temperature, *i.e.*, in the absence of deformation twinning, can be attributed to a novel synergistic sequence of strengthening mechanisms (Fig. 33). Firstly, nanovoids are observed to form near the crack tip at the intersection of two {111} slip planes to create crack-tip bridging. Interestingly, these nanoscale- to submicron-sized voids lead to the formation of considerable amounts of the nanoscale fiber-like regions, which are connected to the crack faces for approximately a few hundred nanometers behind the crack tip (Fig. 33(a)). Nano-twins within the nanobridges are observed during crack extension. Consequently, a large fraction of these nano-bridges showed significant elongation when twinning shear was observed to be the dominant deformation mechanism of the accommodation of plastic deformation. Figs. 33(b,c) shows the tensile loading of the specimen at different stages, where nanobridges spanning the crack and deformation twinning are observed.

As mentioned, the damage resistance of a material can benefit from both intrinsic and extrinsic mechanisms; however, intrinsic mechanisms are the most effective means of toughening in ductile materials, such as metals. The HEA shows a special property in that it can benefit simultaneously from these two mechanisms when deformed at low temperature: a number of plasticity and hardening mechanisms create both high strength and good ductility by intrinsic means, and the nano-bridging near the crack tip, rarely observed in ductile metals, provide extrinsic toughening.

Gludovatz *et al.* [145] also examined an equiatomic CrCoNi MEA with a single-phase *fcc* solid-solution, which shows strength-toughness properties exceeding these of all HEAs and most of the multi-phase alloys. At room temperature, this alloy exhibits ultimate tensile strengths of almost 1 GPa, failure strains of ~0.7, and K_{Ic} fracture-toughness values above 200 MPa.m^{1/2}. The strength, ductility, and toughness of this alloy improve: they are, respectively, 1.3 GPa, ~0.9, and 275 MPa.m^{1/2} at cryogenic temperatures. Compared with the mechanical response of the Cantor alloy, the superior properties of CrCoNi MEA suggest that the mechanical behavior of HEA is related to the nature of elements themselves in MEAs, which is more significant than just the number of mixing-elements. In particular, the three-component alloy is harder than the five-component Cantor alloy and accordingly deformation twins at room temperature, which is thought to contribute to its enhanced toughness.

3.7.1 Fracture morphology

Gludovatz *et al.* [15] concluded that the excellent fracture toughness of the Cantor alloy is connected with a 100% ductile failure by the coalescence of microvoids. Fig. 34(a) shows a representative image of tensile fracture surface from such an alloy obtained after fracture of a specimen. The dimpled appearance is very evident. Dimples are generated from Mn- and Cr-rich particles. One such particle is seen in Fig. 34(b); it has a cuboidal shape. Similar tensile ductile fracture surface has been observed by Wu *et al.* [146] for a refractory Zr₂₅Nb₂₅Hf₂₅Ti₂₅ HEA.

3.8 Fatigue

The process of fatigue failure is usually separated into four stages: (i) initial cyclic damage (cyclic hardening or softening), (ii) formation of an initial flaw where crack initiates, (iii) macroscopic propagation of this flaw, and (iv) the final catastrophic failure or instability, as described by Ritchie *et al.* [147]. The change in the fatigue-crack growth, da/dN , is generally expressed as a function of the applied stress-intensity range ΔK in metals, following the Paris power-law relationship [148]. This approach is

based on linear-elastic fracture, as summarized by the schematic drawing of Fig. 35(a), which shows the change of da/dN with the nominal stress-intensity range ($\Delta K = K_{\max} - K_{\min}$). Indeed, the growth rates depend upon a number of other factors other than ΔK , although this is the main factor promoting the growth of cracks in metals:

$$\frac{da}{dN} = f[\Delta K, K_{\max} (\text{or } R), v, \text{environment}, \text{wave form ...}] , \quad (3.8.1)$$

where v is the frequency and the R is the ratio between minimum and maximum applied loads ($=K_{\min}/K_{\max}$ for positive R). In general, results of fatigue-crack growth rate tests for most ductile metals show the following stages: (i) a region at low values of ΔK and da/dN (less than $\sim 10^{-11}\text{-}10^{-9} \text{ m.cycle}^{-1}$) where fatigue cracks initiate (or grow at very small rates) below the fatigue threshold, ΔK_{TH} ; (ii) an intermediate region ($\sim 10^{-9}$ to $10^{-6} \text{ m.cycle}^{-1}$) described by the Paris power-law equation [148]:

$$da / dN = C(\Delta K)^m , \quad (3.8.2)$$

where C and m (~ 2 to 4 in metals) are material scaling constants; and (iii) an upper region of crack growth (above $\sim 10^{-6} \text{ m.cycle}^{-1}$) as K_{\max} reaches K_c or the loads reach the limit load value for severe plastic deformation.

There are few studies on fatigue-crack propagation in HEAs. Lewandowski and coworkers [149] initially published fatigue data on as-cast Al-CrFeNi-based HEAs and measured extremely high fatigue thresholds with ΔK_{TH} values above $20 \text{ MPa.m}^{1/2}$; these values, however, may be somewhat artificial because of the very coarse as-cast structure of the alloy, the small size of the specimens tested and the correspondingly excessive plasticity throughout their cross-section. Crack-propagation studies using much larger disk-shaped compact-tension specimens have been performed on the wrought Cantor alloy by Thurston *et al.* [150]. They characterized fatigue-crack propagation behavior at a load ratio of $R = K_{\min}/K_{\max} = 0.1$, principally at lower, near-threshold, growth rates in this alloy both at room temperature

(293K) and at low temperature 198K (Fig. 35(b)). At 293K, the alloy showed a fatigue threshold, ΔK_{TH} , of $\sim 4.8 \text{ MPa.m}^{1/2}$, which increased by more than 30% to $\Delta K_{TH} \sim 6.3 \text{ MPa.m}^{1/2}$ with a reduction of temperature to 198 K. In addition, the Paris exponent m for the intermediate range of growth rates was observed to rise from roughly 3.5 to 4.5 with decreasing temperature.

The fracture surfaces and crack paths in the Cantor alloy revealed a transition from primarily transgranular crack propagation at room temperature to intergranular-dominated fracture at the lower temperature [141]. Such a change in crack path is generally connected to an increasing degree of physical contact between the two fracture surfaces, *i.e.* roughness-induced fatigue crack closure, which was deemed as a primary cause for the difference in the measured thresholds. In addition, the higher thresholds found at 198 K were attributed to higher strength of this alloy at lower temperatures, which both reduces the crack-tip opening displacements at a given ΔK and prevents plastic deformation of the grains in the wake of the crack. In general though, there was nothing out of the ordinary about the fatigue-crack propagation properties of this Cr-Co-Ni-based HEA. Its crack-growth resistance and threshold behavior compared favorably with that of traditional metallic alloys, such as austenitic stainless steels and TWIP steels. SEM characterization of the fracture surfaces of samples fatigued at 293 K revealed mainly transgranular crack propagation as shown in Fig. 36(a-c), whereas at 198 K planar slip could also be detected as a major deformation mechanism (Fig. 36(d)). Crack propagation at the lower temperatures occurred mainly through faceted, intergranular-type, failure, as shown in Fig. 36(e,f). The authors concluded that when taken with its remarkable combination of strength, ductility and fracture toughness at both room and cryogenic temperatures, as described above, the Cantor alloy represents an impressive structural material with many potential applications that can utilize its remarkable damage-tolerant properties.

The Al_{0.5}CrFeCoNiCu HEA also shows promising fatigue characteristics [151]. Studies show that this alloy attains the long fatigue life at relatively a high stress. Fig. 37(a) shows that the fatigue endurance limit of this alloy is between 540 MPa and 945 MPa. Some scattering of the fatigue lives of specimens are observed in the stress-life ($S-N$) curves, which may be related to the presence of aluminum oxide particles or microcracks induced during processing (such as casting and rolling). It was proposed that this alloy may have a better fatigue resistance, exceeding that of the conventional alloys, if the number of these defects can be reduced, but this has never been proven. Fig. 37(b) shows that the fatigue endurance strength to ultimate tensile strength (UTS) ratios, between ~0.4 and ~0.7, are high, in comparison with conventional materials, such as Ni, Al, and Ti alloys, steels, and some advanced bulk-metallic glass alloys. This trend, however, may be primarily motivated by the high ultimate tensile strength of the HEAs, which is known to generally enhance fatigue endurance strength.

3.9 Dynamic strain aging

Dynamic strain aging with characteristic serrated flow, also known as the Portevin-Le Chatelier effect, was found to occur in both the single crystal Al_{0.3}CrFeCoNi HEA at 873 K and at 1073 K [152] (Fig. 38(a)). The strain-rate sensitivity, m , is defined by the rate of change of the stress, σ , and obtained by strain-rate change tests:

$$m = \left(\frac{d\sigma}{d\varepsilon} \right)_T . \quad (3.9.1)$$

In the strain-rate change tests, ε was suddenly changed at a plastic strain (ε) of 1% by the following sequence: $1.7 \times 10^{-4} \text{ s}^{-1} \rightarrow 1.7 \times 10^{-5} \text{ s}^{-1} \rightarrow 1.7 \times 10^{-4} \text{ s}^{-1} \rightarrow 1.7 \times 10^{-3} \text{ s}^{-1} \rightarrow 1.7 \times 10^{-4} \text{ s}^{-1}$. A positive strain-rate sensitivity m was observed at 93 K and 293 K, whereas it displays a low or even negative value at 873 K (Fig. 38(b)). This negative strain-rate sensitivity is one of the hallmarks of dynamic strain

aging. Fig. 38(c) shows a transmission electron microscopy (TEM) micrograph of the dislocation configuration on (111) plane of specimens deformed at 873 K [152].

Dynamic strain aging is also observed in the $\text{Al}_{0.3}\text{CrFeCoNi}$ single crystal HEA at 873 K [153]. Similar serration behavior has also been observed in the $\text{Al}_{0.1}\text{CrFeCoNi}$ HEA [154]. Al solute atmospheres are formed near moving dislocation cores [155] or stacking faults [156]. This can raise the frictional stress and retard the dislocation motion. Once the dislocations escape from the solute atmosphere at a specific high stress, the frictional stress suddenly decreases, leading to the serrations in the stress-strain curves [157]. Usually, dynamic strain aging is related to the relationship between the velocity of dislocation motion and the diffusion rate of solutes. A relatively low velocity of dislocation motion, below a critical value, can encourage the creation of a solute atmosphere, making dislocation motion more challenging. Conversely, the frictional stress of the dislocations tends to decrease above a critical value because they escape from their solute atmospheres; these changes lead to the negative strain-rate sensitivity m at 873 K.

Fig. 39(a) shows the serrated flow of Hadfield steel [107] at room temperature under tensile deformation. Three different types of serrations, termed A, B and C and described below, were found at different temperatures in this steel. Types A and B serrations were present at lower temperatures in contrast with type C serrations. The magnitude of serrations increased when the temperature rose, and they gradually disappeared at the temperatures above 190°C. At low temperatures, below roughly -25°C or at high strain rates, the carbon atoms are less mobile in both the dislocation cores and lattice, such that pinning does not happen. Similarly, work hardening in the Hadfield steel is reduced at temperatures above and below the dynamic strain aging range. Thus, the excellent work-hardening ability in Hadfield steel is generally considered to be affected by the interaction of C-Mn couples with the cores of dislocations. However, the contribution of the specific solutes to serration behavior in HEAs still needs

to be examined. This is indeed a fascinating research topic, since interstitial atoms, often held responsible for dynamic strain aging, are not present.

Fig. 39(b) shows three types of serrations in HEAs [158]. Type-A curves show sudden rise of stress accompanied by stress drops. They occur preferentially at high strain rates or at low temperatures. Type-B serrations exhibit such oscillations at a faster frequency; they happen at higher temperatures and at lower strain rates, and can develop from type-A serrations. Type-C curves show the largest stress drops. They occur at lower strain-rates and at higher temperatures, in comparison with types A and B [159, 160].

Serrations are also observed in MEAs and LEAs in specific ranges of strain, dependent on strain rate: the single *fcc* phase LEAs (Ni and CoNi), MEAs (FeCoNi and CrFeCoNi), and HEA (CrMnFeCoNi) exhibit them [159]. Fig. 39(c) indicates the complementary cumulative distributions of slip sizes, $C(S)$, which represent the proportion of serrations that are larger than the stress drop size, S , during one serration process. The complementary cumulative distribution function was then defined as:

$$C(S) \equiv \int_s^{\infty} D(S) dS , \quad (3.9.2)$$

which represents the probability that the stress drop of a slip avalanche is larger than the specific size S . The distribution of small avalanches, $D(S)$, can be described with the small slip-avalanche sizes, S , by $D(S) \sim S^{-\kappa} e^{-S/S_{max}}$ (where κ is a detail-independent exponent and S_{max} is the expected cutoff size of the power-law scaling regime of $D(S)$). The results indicate that there are weak regions on slip planes, where solute atoms diffuse and pin dislocation and impede their motion. This can trigger other slip avalanches resulting in rapid stress drops. When the stress decreases to a specific value, the weak spots can be re-strengthened during the slip avalanches, which are determined by the combination of temperature, strain rate, and chemical composition. The healing rate reaches the highest value at a specific temperature and

strain rate. Abundant sources of solute atoms of HEAs provide higher healing rates than in the conventional strain aging phenomenon. In addition, MEAs (FeCoNi and CrFeCoNi) and the Cantor alloy show faster healing rate between slip avalanches than conventional alloys; thus, HEAs tend to show the Portevin-Le Chatelier effect in a more pronounced fashion than in pure metals and MEAs.

It is possible that local reorganization of the atoms around the dislocation cores is responsible for dynamic strain aging in HEAs. This effect should be prevalent when the jump frequency is compatible with the dislocation velocity. By comparing the formation of serrations for Hadfield steel and CrMnFeCoNi HEA at the same strain rate of 10^{-4} s⁻¹, one can see that they occur within a very different temperature ranges: -10° to 190°C for the Hadfield steel and 300° to 600°C for the HEA. This difference is consistent with interstitial *vs.* substitutional diffusion. The 300°C shift of serration behavior may be because the interstitial diffusion for C in steel dominates at lower temperature and substitutional diffusion for atoms in HEAs dominates at higher temperature, both in the cores of dislocations, leading to the serration behavior.

3.10 High-temperature properties

As the entropy term is enhanced by an increase in temperature through the term TS_{mix} , solid solutions in HEAs should be stabilized at elevated temperatures. Accordingly, refractory HEAs should have many potential applications, particularly for aerospace components [161]. Senkov *et al.* [162] studied mechanical properties of NbMoTaW and VNbMoTaW refractory HEAs with a single *bcc* phase at different temperatures. Fig. 40 indicates that the high-temperature capability (especially yield stress) of some of these refractory HEAs is significantly superior to that of superalloys, such as Inconel 718 superalloy, which is widely used in the gas-turbine industry [163]. The yield strength decreases monotonically until 1000°C, whereas a significant yield strength drop takes place in Inconel 718 at 900°C. In the case of NbMoTaW and VNbMoTaW alloys, the yield strength retains a high value until

1400°C. The superior resistance to high-temperature softening, compared with the conventional superalloys, may be attributed to sluggish diffusion effect of elements in the refractory HEAs at high temperatures up to 1600°C; additionally, it may be related to their very high melting temperatures which approach 3000 K. In addition, Senkov *et al.* [164] found that adding of Al to the AlTiZrNbMo_{0.5}Ta_{0.5} refractory HEA can further improve its high-temperature performance. However, many of these mechanical property evaluations have been performed in compression, which for refractory materials (which are often brittle in nature) may not be truly representative of their actual structural integrity. Indeed, except for the stress, other mechanical properties, such as fracture toughness, fatigue properties and creep resistance, need to be examined in these refractory HEAs if such high-temperature service applications and truly contemplated. Moreover, it would be unlikely that the oxidation resistance of these refractory HEAs compares with that of most Ni- or Co-base superalloys. In this regard, Gorr *et al.* [165] did examine a Al₂₀Ti₂₀Cr₂₀Mo₂₀W₂₀ HEA and found a combination of high hardness (HV800) and good high-temperature oxidation resistance. This alloy was exposed to air at 1000°C for about 40 h with only minor mass change as the presence of the moderate oxide layer on the surface of the alloy proceeded through solid-state diffusion. This result is encouraging but a series of comprehensive studies of the oxidation/corrosion behavior of refractory HEA is definitely warranted before realistic structural applications are considered.

3.11 Creep

3.11.1 Creep mechanisms

Fig. 41 shows the Weertman–Ashby map [166, 167] describing creep mechanisms. The red transition line from the dislocation creep mechanism to the dislocation glide mechanism was observed in the Cantor alloy by Kang *et al.* [168]. The study shows the creep behavior of the Cantor alloy in the intermediate temperatures (from 535 °C to 650 °C). The transition from the dislocation-climb

mechanism to the dislocation-glide mechanism was revealed when the stresses drop to ~ 40 MPa. Their calculation shows that Cr is the most influential element to viscous glide behavior at high stresses. This is attributed to the large atomic size misfit of Cr to relieve the dislocation line energy and the appropriate diffusivity comparable to the dislocation velocity. For simplicity, Weertman-Ashby plots assume that there are some unique and distinct regimes of deformation of materials in the absence of phase transformations [1]. The main creep mechanisms are listed below: (i) above the theoretical shear strength, plastic flow of the material can occur without dislocations, by simple glide of one atomic plane over another; (ii) dislocation glide occurs for $\sigma/G > 10^{-2}$; (iii) dislocation creep includes glide and climb, both being influenced by diffusion. In the stress range $10^{-5} < \sigma/G < 10^{-2}$, creep tends to occur by dislocation glide assisted by vacancy diffusion (when an obstacle has to be overcome); (iv) diffusion creep tends to occur for $\sigma/G \leq 10^{-5}$. Nabarro *et al.* [169] proposed a mechanism by which vacancies move from one grain boundary to another, a process which has become known as Herring-Nabarro creep. This mechanism involves the flux of vacancies inside the grain; the vacancies moving in such fashion result in an elongation of the grain along the loading direction; (v) Coble [202] proposed a similar mechanism based on grain-boundary diffusion to achieve the same effect; this occurs at slightly lower homologous temperatures than Herring-Nabarro creep.

It is possible to differentiate the different diffusion mechanisms by experiments at which the steady-state creep rate $\dot{\varepsilon}_{ss}$ is established as a function of the applied stress [170]. It is well accepted that the creep stress exponent, $n = \partial \ln \dot{\varepsilon}_{ss} / \partial \ln \sigma$, ($\dot{\varepsilon}_{ss}$ is the steady-state creep rate and σ is the applied stress), is an effective indicator to reveal the creep mechanisms in metallic materials. For example, $n = 1$ is consistent with diffusion creep by Nabarro-Herring creep (by lattice diffusion) and Coble creep (by

grain-boundary diffusion); $n = 2$ is consistent with grain-boundary sliding, and $n > 3$ with dislocation creep.

Lee *et al.* [40] performed creep experiments on nanocrystalline CrMnFeCoNi HEAs prepared by high-pressure torsion. Fig. 42(a) depicts the initial dendritic microstructure for the as-received HEAs. To observe the initial microstructure, grain size and grain orientations in the HEAs, electron backscatter diffraction (EBSD) analysis was used. Fig. 42(b) shows that initial grain size d was about $46 \mu\text{m}$. The microstructure of the specimens at the edges of the high-pressure torsion (HPT) disk specimens for 1/4 and 2 turns was then examined by transmission electron microscopy (TEM). These turns correspond to an applied equivalent strain ~ 5 and ~ 40 at the edges, respectively. Figs. 42(c,d) show bright-field TEM images and corresponding selected area diffraction (SAD) patterns of the microstructures at the disk edges for 1/4 and 2 turns, respectively. The SAD patterns for both samples indicate a single *fcc* phase. These images illustrate that equiaxed fine grains with an average grain size d of ~ 49 and $\sim 33 \text{ nm}$ for 1/4 and 2 turns, respectively. Furthermore, indentation creep tests in these areas indicated that creep occurred in both coarse-grained and nanocrystalline HEAs even at room temperature, although it was more apparent at higher shear strains.

The time-dependent plastic deformation behavior of nanocrystalline and coarse-grained CrMnFeCoNi HEAs was systematically investigated by Lee *et al.* [40] using a spherical nanoindentation creep setup. Fig. 43(a) shows that the creep exponent n was estimated to be ~ 3 for the coarse-grained HEA and ~ 1 for the nanocrystalline alloy. The dominant creep mechanisms were examined considering the values of n and their creep activation volumes V^* (defined in Section 3.2), which can be expressed as:

$$V^* = \sqrt{3}kT \left(\frac{\partial \ln \dot{\varepsilon}_{QSS}}{\partial \sigma} \right), \quad (3.11.1)$$

where k is the Boltzmann's constant and T is the absolute temperature, $\dot{\varepsilon}_{\text{oss}}$ is the steady-state creep rate and σ is the normal stress. It was reported that the value of V^* varied by orders of magnitude for the various rate-limiting processes. Specifically, it changes in the range of $\sim 100 b^3$ to $1000 b^3$ for dislocation glide in *fcc* materials, down to $\sim b^3$ for diffusion either along the grain boundaries or through the crystalline lattice [85]. In Fig. 43(b), the V^* for the nanocrystalline Cantor alloy is calculated as $\sim 0.8 b^3$, which indicates that the dominant creep mechanism in these alloys may be diffusion creep. For coarse-grained Cantor alloy, the calculated V^* is $\sim 4.6 b^3$. This is much smaller than that for the conventional *fcc* metals where cutting forest dislocation mechanism takes the dominant role; Lee *et al.* [40] attributed this to diffusion along the interface between the tip of the indenter and the surface of the sample. In summary, creep mechanisms in the nanocrystalline CrMnFeCoNi HEA at room temperature appear to be predominantly controlled by grain-boundary diffusion. These alloys are claimed to have better creep resistance than conventional *fcc* nanocrystalline metals, possibly because of its sluggish-diffusion effect.

3.11.2 Superplasticity

Processing of a CrMnFeCoNi HEA by high pressure torsion through 5 turns resulted in a grain-size of ~ 10 nm and gave excellent ductility in tensile tests at 873–1073 K, including superplastic elongations ($> 400\%$) at temperatures of 873 and 973 K, as shown in Fig. 44 [173]. The maximum total elongation exceeded 600% at 973 K. To understand the mechanism controlling the superplastic deformation in the CrMnFeCoNi HEA, the Mukherjee-Bird-Dorn equation was utilized [203]:

$$\dot{\varepsilon} = A \left(\frac{b}{d} \right)^p \left(\frac{\sigma}{G} \right)^{1/q} \exp \left(-\frac{Q}{RT} \right), \quad (3.11.2)$$

where A is a constant, σ is the flow stress, G is the shear modulus, b is the Burgers vector, d is the grain size, p is the grain size exponent, Q is the activation energy for deformation, R is the gas constant and T is the absolute temperature. An experimental activation energy Q for the Cantor alloy, $\sim 113 \text{ kJ.mol}^{-1}$, is

close to the value of $\sim 115 \text{ kJ}\cdot\text{mol}^{-1}$ reported for grain-boundary diffusion in pure Ni [171]. Also, it is reported that Ni is the element having the lowest diffusion coefficient in Cantor alloy. This suggests that, as in conventional superplasticity [172], the rate of flow is controlled by grain-boundary diffusion. The existence of superplastic elongations suggests that grain-boundary diffusion occurs in this alloy at 873–1073 K. This is confirmed by the absence of any elongated grains within the microstructure after tensile testing and the lack of any incipient necking within the gauge length. The strain-rate sensitivity m was measured to be ~ 0.3 in these experiments but analysis shows that this value, which is lower than the regular value of $m = 0.5$ for superplastic flow [172], is caused by the appearance of significant grain growth during tensile loading. Accordingly, Shahmir *et al.* [173] concluded that the CrMnFeCoNi HEA was not deformed by dislocation glide and exhibited true superplastic flow when tested at elevated temperatures.

The fracture surfaces from tensile specimens show a significant effect of grain size. CrMnFeCoNi HEAs, subjected to high pressure torsion deformation by Schuh *et al.* [70] and having a grain size of $\sim 50 \text{ nm}$, were subsequently annealed at different temperatures and times to produce different grain sizes. Whereas the fracture surface of the nanocrystalline material (Fig. 45(a)) is composed of ductile dimples with a few hundred nanometers, it becomes gradually more brittle, forming grain-boundary cracks when it is annealed for 1 and 15 hours, respectively, at 450°C , Figs. 45(b,c). Correspondingly, the embrittlement is caused by the presence of the multiphase-composite consisting of several different new phases. By increasing the annealing temperature to 600° , 700° , and 800°C , significant grain growth takes place, resulting in a decrease in strength. The fracture surface returns to its ductile dimpled morphology. For the elevated annealing temperature anneals in Figs. 45(d, e, f), the dimple sizes gradually increase. For anneals at 800°C , the spacing of particles increases and so does

the dimple size (Fig. 45(f)). This size, ~20 um, is approximately the same as that reported by Gludovatz *et al.* [15] and shown in Fig. 30.

3.12 Compression response in micro/nanopillar experiments

So-called nanopillar experiments consist of subjecting a cylindrical specimen with a diameter in the 100 nm-10 μm range to compression. They have provided an enlightening look at the plastic response of metals because they enable the isolation of specific mechanisms that are dependent on the spatial scale. First introduced in 2005 by Greer, Oliver and Nix [174], they have been useful in explaining how strength can be specimen size-dependent. In the cylindrical geometry, there are no stress/strain gradients and therefore the observed behavior cannot be attributed to gradient effect. For monocrystalline gold, and later for a number of metals, a significant size effect was observed: the yield stress of gold increased from 30 MPa (characteristic of the bulk material) for a pillar size of 7 μm to 4.56 GPa for a diameter of 300 nm. Greer *et al.* [175-178] and Arzt and coworkers [179] proposed a dislocation starvation mechanism to explain the marked elevation of strength in deforming nanoscale pillars. Unlike deformation mechanisms in bulk materials, dislocations in micro/nano pillars can move very limited distances before disappearing at free surfaces, thus reducing the overall dislocation reproduction rate. Accordingly, gliding dislocations will leave the pillars more rapidly than they reproduce, reducing their overall density. These sequences result in a “dislocation-starved” state, demanding very high stress to nucleate new dislocations. This is especially the case when the grain size is larger than the pillar diameter; virtually all existing dislocations can escape, prior to multiplying.

Zou *et al.* [180, 181] studied the mechanical response of pillars of the HEA Nb₂₅Mo₂₅Ta₂₅W₂₅ with average grain size ~100 nm. The small-scale pillars were prepared by focused ion beam machining with the subsequent micro-compression tests performed in a nanoindenter. After the experiments, some of pillars larger than 1 μm in diameter showed evidence of cracking along grain boundaries at

strains larger than ~ 0.2 , as shown in Fig. 46(a). The smaller pillars (Figs. 46(b–d)) experienced more continuous plastic deformation without too much cracking, even at strains larger than ~ 0.3 , suggesting that ductility is significantly improved with the decrease of the pillar size. In addition, a 580-nm normal sputtering HEA pillar, termed “Normal”, exhibited a yield strength of ~ 5 GPa, whereas a 580 nm ion beam-assisted deposition HEA pillar, termed “IBAD”, showed an extremely high yield strength of ~ 6.5 GPa. These strengths are about twice of that of the single crystal HEA pillar and six times of that of the bulk HEA, as shown in Fig. 46(e). These HEA pillars also show a size-dependent strength, as illustrated by the relationship between the flow stress at 5% strain ($\sigma_{0.05}$) vs. the pillar diameter, D , shown in Fig. 46(f). The IBAD HEA pillars show the highest strength levels, around 5 to 7 times higher than that of single-crystal W pillars [179], and the slightest size-dependence [182]. The HEA pillar with a 70 nm diameter displayed an exceptionally high yield strength of ~ 10 GPa, representing one of the highest reported strengths in micro-/nano-pillar compression tests, and one order of magnitude higher than that of the same materials when measured in macroscopic sample. This pillar showed significant ductility, with compressive plastic strains over 20%; however, it is not expected that the tensile ductility would be anyway near as high.

3.13 High strain-rate and high-pressure deformation

The high-strain rate response of materials is important in applications such as crashworthiness of vehicles and ballistics (either as a projectile or armor). High-entropy alloys, due to their excellent work-hardening ability, would seem to be natural candidates for these extreme regimes of deformation. Hadfield steels, which have similar strength-ductility characteristics, were used for helmets in World Wars I and II, specifically, the Brodie helmet used by the British Army.

Corresponding assessments of the dynamic properties of HEAs to date have included a range of testing methods, including: (i) Hopkinson bar experiments to determine dynamic strength at $10^3\text{--}10^4\text{ s}^{-1}$;

- (ii) gas gun impact experiments to establish the Hugoniot Elastic Limit; (iii) wave reflection experiments (in gas gun or using laser pulses) to establish the ultimate tensile strength, known as spall strength [183];
- (iv) shear localization experiments (both forced and spontaneous) to establish the susceptibility of HEAs to failure by adiabatic shear bands.

The dynamic properties of a single *fcc* phase Al_{0.3}CrFeCoNi HEA have been investigated using a combination of Hopkinson bar experiments, constitutive equations and forced shear localization by Li *et al.* [96]. A combination of multiple strengthening mechanisms such as solid-solution hardening, forest dislocation hardening (Figs. 47(a,b)), as well as mechanical twinning (Figs. 47(c,d)) results in a high work-hardening rate in this alloy. The shear-band susceptibility was studied by dynamically-loading hat-shaped specimens (Fig. 47(e)) to induce forced shear localization. However, no adiabatic shear bands could be observed in Fig. 47(f). Adiabatic shear bands tend form when the material starts to “soften”. The condition for instability, expressed in terms of shear stress τ and shear strain γ , is $\frac{d\tau}{d\gamma} \leq 0$. It can be expressed from the general function $\tau = f(\gamma, \dot{\gamma}, T)$ (where $\dot{\gamma}$ is shear strain-rate and T is the material) by differentiation:

$$\frac{d\tau}{d\gamma} = \left(\frac{\partial \tau}{\partial \gamma} \right)_{\dot{\gamma}, T} + \left(\frac{\partial \tau}{\partial \dot{\gamma}} \right)_{\gamma, T} \frac{\partial \dot{\gamma}}{\partial \gamma} + \left(\frac{\partial \tau}{\partial T} \right)_{\gamma, \dot{\gamma}} \frac{dT}{d\gamma} \leq 0 \quad . \quad (3.13.1)$$

The normal stress and strain can be provided by the Zerilli-Armstrong constitutive equation (Eqn. 3.6.4), which requires obtaining the parameters (n , C_1 , C_2 and C_3) experimentally at different strain rates and temperatures. They can be converted into the corresponding shear stress τ and shear strain γ [184] through: $\tau = \frac{\sigma}{2}$ and $\gamma = \sqrt{2e^{2\varepsilon} - 1} - 1$. Experiments on Al_{0.3}CrFeCoNi HEA were conducted at constant strain rate ($\dot{\gamma} \sim 10^4 \text{ s}^{-1}$) and temperature T [88] up to a shear strain of 1.1. The strain hardening

parameter $\left(\frac{\partial \tau}{\partial \gamma}\right)_{\gamma,T}$ was established as ~ 440 MPa, and the thermal softening parameter $\left(\frac{\partial \tau}{\partial T}\right)_{\gamma,\gamma}$ was ~ -0.2 MPa.K $^{-1}$. Consequently, $\frac{dT}{d\gamma} = 175$ K $^{-1}$. Neglecting the second term in Eqn. 3.13.1:

$$\frac{d\tau}{d\gamma} = \left(\frac{\partial \tau}{\partial \gamma}\right)_{\gamma,T} + \left(\frac{\partial \tau}{\partial T}\right)_{\gamma,\gamma} \frac{dT}{d\gamma} \approx 440 - 0.2 \times 175 = 405 \text{ MPa} \geq 0. \quad (3.13.2)$$

Thus, the condition for shear instability is not reached, and no shear bands would be formed at a shear strain equal to ~ 1.1 , the highest value used in these experiments. As the strain increases, the term $(d\tau/d\gamma)$ decreases until eventually it becomes equal to zero. This marks the onset of shear localization and the failure of the material.

Thus, one concludes that (i) the high strain-hardening rate, enabled by solid-solution hardening, forest dislocation hardening and twinning hardening, (ii) the high strain-rate sensitivity and (iii) modest thermal softening, all act in concert to give rise to the high resistance to shear localization of the Al_{0.3}CrFeCoNi HEA.

To further study shear localization in HEAs, hat-shaped specimens of the CrMnFeCoNi HEA were subjected to more severe shear strains (beyond 1.1) to produce shear bands, as shown in Fig. 48(a). Fig. 48(b) shows that the temperature (calculated by converting 90% of work done into heat) can rise to the recrystallization region (0.3T_m-0.5T_m) inside the shear band. This requires a shear strain of ~ 7 . In agreement with the recrystallization hypothesis, the onset of shear localization did occur for a strain of ~ 7 . Fig. 48(c) shows the microstructure of the shear band, which had a width of ~ 10 μm . Due to the sluggish diffusion effect of HEAs, the recrystallized grains cannot be formed by migration recrystallization mechanisms (recrystallization produced by nucleation and growth of new grains); rather the equiaxed grains are proposed to be formed by a rotational dynamic recrystallization mechanism [185]. This same mechanism operates in severe plastic deformation (SPD). Essentially the grains break

down by virtue of extreme plastic deformation, the dislocations forming subgrains and these transforming to ultrafine or nano grains by continued plastic deformation. The recrystallized twin, shown by the red arrow in Fig. 48(d), was also found inside the ultrafine grain under high strain-rate deformation due to the alloy's low stacking-fault energy.

Both $\text{Al}_{0.3}\text{CrCoFeNi}$ and CrMnFeCoNi high-entropy alloys show high strain-hardening ability under dynamic impact as shown in Fig. 49(a). The twin networks, where the twin boundaries act as barriers to dislocation motion, provide for higher strength. In addition, the interaction of deformation twins can also generate a high strain-hardening rate. One of our findings is that shear localization of the CrMnFeCoNi high-entropy alloy was only found at a shear strain larger than 7 under dynamic compression, as shown in Fig. 49(d). It is therefore proposed that the combination of the excellent strain-hardening ability in Fig. 49(c) and modest thermal softening in Fig. 49(b) lead to the exceptional resistance to shear localization [186].

Jiang *et al.* [187] studied shock compression of the *fcc* CrMnFeCoNi HEA and the *bcc* AlCrFeCoNi HEA. The results showed that these two kinds of HEAs exhibited a relatively high Hugoniot elastic limit and high-phase transition threshold stress. The observed amounts of dislocations and mechanical twins indicate that these are the dominant deformation modes at extreme-high strain-rates in the *fcc* CrMnFeCoNi HEA. However, in the *bcc* AlCrFeCoNi HEA samples recovered from extreme-high strain-rate experiments, only highly tangled dislocations were found. Wu *et al.* [188] reported amorphization at twin-twin intersection regions in the CrFeCoNi HEA subjected to high-pressure torsion. The amorphous phase nucleated and grew at twin-twin intersections, while the expansion of amorphous phase was restricted by the intersected twin boundaries. The nucleation of amorphous phases at intersections of stacking faults and twins has also been demonstrated by molecular dynamics (MD) simulation and observed in shock compression of Si and Ge [189]. Tray *et al.* [204]

reported the high-pressure synthesis of a *hcp* phase CrMnFeCoNi HEA. The martensitic transformation starts at 14 GPa and was attributed to the suppression of the local magnetic moments, destabilizing the initial *fcc* structure. However, the behavior of CrMnFeCoNi HEA is uncommon in that the *hcp* phase is retained following decompression to room pressure, producing a metastable mixture of *fcc* and *hcp* phases. This provides a method of altering the microstructures and mechanical properties of HEAs, which cannot be achieved by conventional processing techniques.

Recently, laser ablation-driven shock experiments have proven to be a powerful tool to understand the deformation mechanisms of materials in a regime of strain rates ($10^7\text{--}10^8\text{ s}^{-1}$) [190-193] and pressures (100-200 GPa). This regime is known as ‘extreme’. Preliminary results show that the Al_{0.3}CrFeCoNi undergoes massive planar faulting (as shown in Fig. 50(b)) when subjected to laser shock compression [194]. These planar faults, whose interfaces align with the {111} planes of the *fcc* lattice, are presumably nano-sized deformation twins. Note that there is extra contrast within the planar faulted area (Fig. 50(c)), suggesting the interaction of planar faulting with other deformation mechanisms such as dislocation-mediated plasticity. The thermal effect is another factor that must be considered in laser shock experiments. Fig. 50(a) shows that in addition to the high density of planar faults, the surface of the shock-recovered sample was covered by a nanocrystalline layer (grain size ~50 nm), which is the result of melting and rapid quenching.

More recent results on shock hardening (front surface) and spalling (rear surface) of the Cantor alloy employed laser ablation shock compression as a surface modification method. The ultrafast ionization and condensation of the surface atoms usually result in a refined micro/nanostructure and the passage of the shock wave imposes a compressive deformation onto the materials. Zhao *et al.* [195] shocked an as-cast Cantor alloy using a nanosecond pulsed laser with a peak laser intensity of 10^{16} kg.s^{-3} , generating a compressive stress of ~180 GPa. The strength of the Cantor alloy increases with the strain

rate. The 180 GPa compressive stress is the peak longitudinal shock pressure that was imposed on the surface of the target by intense laser ablation. It does not mean that the yield strength of the material is 180 GPa. HEAs will yield long before that, resulting a hydrostatic stress-state. The work produced by pressure (time volumetric strain) leads to the generation of heat at shock front which leads to the surface melting of the sample. It should also be noted that the stress will decay rapidly as the shock wave propagates through the sample. The resultant microstructure from the recovered sample can be seen in the secondary electron SEM micrograph in Fig. 51(a) which shows shock crater clearly visible at the front surface. Fig. 51(b) is the magnified view of the ultrafine-grained surface region inside the shock crater, revealing a grain size of 100~500 nm. Front-view SEM images suggest these grains are equiaxed; however, the cross-sectional TEM images reveal that they are actually columnar and that the grain boundaries tend to align with the direction of the shock-wave propagation. These features are shown in Fig. 51(c), with the various deformation features such as dislocations and stacking faults visible below the surface.

Upon release of the shock wave, *i.e.*, when the compressive wave is reflected at the free (rear) surface, the resultant stress state is changed from compression to tension. Fracture then tends to occur at the plane where the material experiences the highest tensile stress. Such a process is termed spalling and is usually achieved by void nucleation, growth and coalescence in ductile metals. Meyers *et al.* [196] proposed that the homogeneous void initiation in ductile metals can happen at vacancy clusters or special grain-boundary configurations such as triple junctions through shear loop expansion, which has been observed in the fracture of the nanocrystalline copper under high strain-rate tension. Spalling leads to the bulge of the rear surface. X-ray computed tomography reconstruction shows that a fracture surface was created within the sample, as shown in Figs. 51(d,e). The rough fracture surface seen in Fig. 51(e) indicates that the Cantor alloy undergoes a very ductile failure under dynamic loading, which is

attributed to the defining deformation mechanisms of this material. The current research aims at determining the stress at which this fracture occurs; this has an important bearing on the ballistic performance of this alloy.

4. Summary and conclusions

The number and different types of high-entropy alloys (HEAs) are essentially unbounded and research to date has hardly *even scratched the surface* (so to speak). Accordingly, it is essential that one avoids generalizations when evaluating the mechanical properties, or any other properties for that matter, of HEAs. Of the hundreds of alloys synthesized to this date, many have poor performance. The same complexities governing the mechanical response of established and experimental alloys apply to HEAs: the structure, as well as composition, determines the mechanical properties through the classic strengthening and weakening mechanisms. Accordingly, we could not possibly in this review comprehensively evaluate the mechanical response of all of the growing number and classes of HEAs being developed, but instead have focused primarily on medium- and high-entropy alloys based on the transition metal elements of Cr, Co and Ni, which generally display some of the best properties reported to date.

Specifically, many high-entropy alloys though, in particular those based on the CrCoNi system, show excellent mechanical properties and appear promising as structural materials for future structural applications. These mechanical properties are in part due to the operation of multiple deformation mechanisms, including solid-solution strengthening, dislocation slip, twinning and in some alloys phase transformations. This class of alloys, which initially consisted of solid solutions, has now expanded to include two-phase materials, such that the mechanical response is not only characteristic of a single-phase face-centered cubic alloy, but incorporates complexities due to multiple phases and, in some cases, stress-induced martensitic transformations. The strength, ductility, and mechanical performance are

intimately connected to their structure and the activation of these mechanisms; we note that face-centered and body-centered cubic HEAs have different strain-rate sensitivities and thermal softening responses, as do two-phase HEAs and HEAs containing brittle phases (R, σ , $t\sigma$, and Laves). Below are listed the most prominent mechanical properties:

(1) The values of G and E of the CrMnFeCoNi Cantor alloy are 80 and \sim 200 GPa, respectively, while at 77 K the corresponding values are 85 and 214 GPa, respectively. The temperature dependence of the elastic modulus of this HEA does not appear to be anomalous compared to other metals and alloys. We do not expect any anomalous elastic response for the other HEAs unless unforeseen phase transformations (such as *fcc* to *bcc*) take place.

(2) CrCoNi-based HEAs possess good ductility due to a combination of dislocation slip and twinning and, in some cases, phase transformations. A transformation induced plasticity-assisted, dual-phase Co₁₀Mn₃₀Fe₅₀Cr₁₀ high-entropy alloy exhibits enhanced trans-grain and inter-grain slip resistance, and hence, increased strength. Moreover, the increased strain-hardening capacity that is enabled by dislocation hardening of the stable phase and transformation-induced hardening of the metastable phase produces increased ductility.

(3) The face-centered cubic Cantor alloy shows exceptional mechanical properties, particularly at cryogenic temperatures, due to a synergy of deformation mechanisms associated with the alloy's low stacking-fault energy and high lattice friction, and additionally with the onset of deformation nanotwinning at lower temperatures.

(4) Several CrCoNi alloys possess high fracture toughness with a combination of high strength and ductility develop through extrinsic and principally intrinsic toughening mechanisms. At room temperature, these alloys show tensile strengths of almost 1 GPa, failure strains of \sim 70% and K_{Ic}

fracture-toughness values above $200 \text{ MPa.m}^{1/2}$; at cryogenic temperatures, the strength, ductility and toughness of the CrCoNi alloy are enhanced even further to strength levels above 1.3 GPa, failure strains up to 90% and K_{Ic} values of $275 \text{ MPa.m}^{1/2}$. These are some of the highest values of damage-tolerance (strength and toughness) reported to date. Compared with the mechanical response of CrMnFeCoNi HEA, the superior properties of MEA CrCoNi, which result from a greater propensity for deformation twinning, suggest that the mechanical behavior of HEAs is related to the elements in complex solid solutions and the resulting microstructures, rather than the mere number of elements present.

(5) Encouraging fatigue resistance characteristics due to the long fatigue lives of various samples at relatively high stresses has been obtained. The $\text{Al}_{0.5}\text{CoFeCrNiCu}$ HEA shows promising fatigue resistance characteristics.

(6) High impact resistance of HEAs is expected from their good high strain-rate plasticity. The high strain-hardening ability of the $\text{Al}_{0.3}\text{CoFeCrNi}$ HEA, enabled by solid-solution hardening, forest dislocation hardening and twinning hardening, a marked strain-rate sensitivity and modest thermal softening, result in an excellent resistance to shear localization. For the CrMnFeCoNi alloy, a shear strain of ~ 7 has been reported as required for the shear-band propagation (using a hat-shaped specimen that enables one single shear band to initiate and grow). This compares very favorably to a shear strain of ~ 1 for a Ti-6Al-4V alloy. This resistance to shear localization is critical for ballistic applications.

(7) High-temperature superplasticity of the CrMnFeCoNi alloy was found to be primarily associated with grain-boundary sliding.

(8) Refractory HEAs (with compositions based on Nb, Mo, Ta and W) have also been developed with exceptional high-temperature properties. Although their ambient temperature strength is below that of the common superalloys (*e.g.*, Inconel 718 and Haynes 23), their strength is retained up to

temperatures above 1200°C. In the case of NbMoTaW and VNbMoTaW, the yield strength is retained at a high value up to 1400°C. The stability of the solid solution at higher temperature is enhanced by the increasing importance of the entropic term, TS_{mix} .

(9) The hardness of HEAs varies widely from ~140 HV to ~1200 HV, and even higher for nanocrystalline HEAs. This is due to the broad range in compositions of these alloys and of their structures, including grain sizes. The high hardness due to solid-solution strengthening, grain-boundary strengthening, dislocation reactions and secondary phase strengthening.

(10) High-entropy oxides and diborides are being developed which show significant potential. Other ceramic systems, such as carbides, carbonitrides, and nitrides will follow rapidly.

Acknowledgments

This work was supported by the U.S. Department of Energy through grant NNSA/SSAP (DE-NA0002080) and the UCSD Center for High Energy Density Science (UCOP LAB FEES GRANT ID: LFR-17-449059) (for S.Z. and M.A.M.), and through the Mechanical Behavior of Materials Program (KC13) at the Lawrence Berkeley National Laboratory supported by the Office of Science, Office of Basic Energy Sciences, Materials Sciences and Engineering Division, under contract no. DE-AC02-05CH11231 (for R.O.R.). Additional support was provided by the University of California Research Laboratories, Grant 09-LR-06-118456-MEYM (for S.Z. and M.A.M.), and by a China Scholarship Council Scholarship (grant no. 201508020004) for Z.L.

References

- [1] Meyers MA, Chawla KK. Mechanical behavior of materials: Cambridge University Press Cambridge. 2009.
- [2] Ritchie RO. The conflicts between strength and toughness. *Nature Materials*. 2011;10:817-22.
- [3] Yeh J-W, Chen SK, Lin SJ, Gan JY, Chin TS, Shun TT, Chang SY. Nanostructured high-entropy alloys with multiple principal elements: novel alloy design concepts and outcomes. *Advanced Engineering Materials*. 2004;6:299-303.
- [4] Cantor B, Chang ITH, Knight P, Vincent AJB. Microstructural development in equiatomic multicomponent alloys. *Materials Science and Engineering: A*. 2004;375–377:213-8.
- [5] Cantor B. Multicomponent and high entropy alloys. *Entropy*. 2014;16:4749-68.
- [6] Otto F, Dlouhý A, Pradeep KG, Kuběnová M, Raabe D, Eggeler G, George EP. Decomposition of the single-phase high-entropy alloy CrMnFeCoNi after prolonged anneals at intermediate temperatures. *Acta Materialia*. 2016;112:40-52.
- [7] Ranganathan S. Alloyed pleasures: multmetallic cocktails. *Current science*. 2003;85:1404-6.

- [8] Miracle D, Senkov O. A critical review of high entropy alloys and related concepts. *Acta Materialia*. 2017;122:448-511.
- [9] Miracle DB, Miller JD, Senkov ON, Woodward C, Uchic MD, Tiley J. Exploration and development of high entropy alloys for structural applications. *Entropy*. 2014;16:494-525.
- [10] Rost CM, Sachet E, Borman T, Moballegh A, Dickey EC, Hou D, Jones JL, Curtarolo S, Maria JP. Entropy-stabilized oxides. *Nature Communications*. 2015;6:8454.
- [11] Gild J, Zhang Y, Harrington T, Jiang S, Hu T, Quinn MC, Mellor WM, Zhou N, Vecchio K, Luo J. High-entropy metal diborides: A new class of high-entropy materials and a new type of ultrahigh temperature ceramics. *Scientific Reports*. 2016;6:37946.
- [12] Jiang S, Hu T, Gild J, Zhou N, Nie J, Qin M, Harrington T, Vecchio K, Luo J. A new class of highentropy perovskite oxides. *Scripta Materialia*. 2018;142:116-20.
- [13] Cantor B, Kim K, Warren PJ. Novel multicomponent amorphous alloys. *Materials Science Forum*. 2002; 386:27-31.
- [14] Paschoal J, Kleykamp H, Thuemmler F. Phase equilibria in the quaternary molybdenum-ruthenium-rhodium-palladium system. *Zeitschrift Für Metallkunde*. 1983;74:652-64.
- [15] Gludovatz B, Hohenwarter A, Catoor D, Chang EH, George EP, Ritchie RO. A fracture-resistant high-entropy alloy for cryogenic applications. *Science*. 2014;345:1153-8.
- [16] Granberg F, Nordlund K, Ullah MW, Jin K, Lu C, Bei H, Wang LM, Djurabekova F, Weber WJ, Zhang Y, Mechanism of radiation damage reduction in equiatomic multicomponent single phase alloys. *Physical Review Letters*. 2016;116:135504.
- [17] Zhang Y, Zuo TT, Tang Z, Gao MC, Dahmen KA, Liaw PK, Lu ZP, Microstructures and properties of high-entropy alloys. *Progress in Materials Science*. 2014;61:1-93.

- [18] Tsai M-H, Yeh J-W. High-entropy alloys: a critical review. *Materials Research Letters*. 2014;2:107-23.
- [19] Gao MC, Yeh J-W, Liaw PK, Zhang Y. *High-Entropy Alloys*. Springer. 2016.
- [20] Murty BS, Yeh J-W, Ranganathan S. *High-entropy alloys*: Butterworth-Heinemann. 2014.
- [21] Ruffa A. Thermal potential, mechanical instability, and melting entropy. *Physical Review B*. 1982;25:5895.
- [22] Swalin RA, King AL. Thermodynamics of solids. *American Journal of Physics*. 1962;30:778.
- [23] Swalin RA. *Thermodynamics of solids*. Wiley. 1972.
- [24] Gearhart CA. Einstein before 1905: The early papers on statistical mechanics. *American Journal of Physics*. 1990;58:468-80.
- [25] Yeh J-W, Chen YL, Lin SJ, Chen SK. High-entropy alloys—a new era of exploitation. *Materials Science Forum: Trans Tech Publ*. 2007;560:1-9.
- [26] Takeuchi A, Inoue A. Calculations of Mixing Enthalpy and Mismatch Entropy for Ternary Amorphous Alloys. *Materials Transactions, JIM*. 2000;41:1372-8.
- [27] Otto F, Yang Y, Bei H, George EP. Relative effects of enthalpy and entropy on the phase stability of equiatomic high-entropy alloys. *Acta Materialia*. 2013;61:2628-38.
- [28] Barrett C, Massalski T. *Structure of Metals*, 3rd. Pergamon Press. 1980.
- [29] Mishra R, Kumar N, Komarasamy M. Lattice strain framework for plastic deformation in complex concentrated alloys including high entropy alloys. *Materials Science and Technology*. 2015;31:1259-63.
- [30] Yeh J-W, Chang S-Y, Hong Y-D, Chen S-K, Lin S-J. Anomalous decrease in X-ray diffraction intensities of Cu–Ni–Al–Co–Cr–Fe–Si alloy systems with multi-principal elements. *Materials Chemistry and Physics*. 2007;103:41-6.

- [31] Pradeep K, Wanderka N, Choi P, Banhart J, Murty B, Raabe D. Atomic-scale compositional characterization of a nanocrystalline AlCrCuFeNiZn high-entropy alloy using atom probe tomography. *Acta Materialia*. 2013;61:4696-706.
- [32] Ozdol V, Gammer C, Jin X, Ercius P, Ophus C, Ciston J, Minor A. Strain mapping at nanometer resolution using advanced nano-beam electron diffraction. *Applied Physics Letters*. 2015;106:253107.
- [33] Ding J, Yu Q, Asta M, Ritchie RO. Tunable stacking fault energies by tailoring local chemical order in CrCoNi medium-entropy alloys. *Proceedings of the National Academy of Sciences*. 2018;115(36): 8919-8924.
- [34] Laplanche G, Kostka A, Reinhart C, Hunfeld J, Eggeler G, George E. Reasons for the superior mechanical properties of medium-entropy CrCoNi compared to high-entropy CrMnFeCoNi. *Acta Materialia*. 2017;128:292-303.
- [35] Zhang F, Zhao S, Jin K, Xue H, Velisa G, Bei H, Huang R, Ko JYP, Pagan DC, Neufeind JC, Weber WJ, Zhang Y. Local structure and short-range order in a NiCoCr solid solution alloy. *Physical Review Letters*. 2017;118:205501.
- [36] Ma Y, Wang Q, Li C, Santodonato LJ, Feygenson M, Dong C, Liaw PK. Chemical short-range orders and the induced structural transition in high-entropy alloys. *Scripta Materialia*. 2018;144:64-8.
- [37] Lei Z, Liu X, Wu Y, Wang H, Jiang S, Wang S, Hui X, Wu Y, Gault B, Kontis P, Raabe D, Gu L, Zhang Q, Chen H, Wang H, Liu J, An K, Zeng Q, Nieh T-G, Lu Z. Enhanced strength and ductility in a high-entropy alloy via ordered oxygen complexes. *Nature*. 2018;563:546–550.
- [38] Tsai K-Y, Tsai M-H, Yeh J-W. Sluggish diffusion in Co–Cr–Fe–Mn–Ni high-entropy alloys. *Acta Materialia*. 2013;61:4887-97.
- [39] Zhang Y, Zhuang Y, Hu A, Kai J, Liu C. The origin of negative stacking fault energies and nano-twin formation in face-centered cubic high entropy alloys. *Scripta Materialia*. 2017;130:96-9.

- [40] Lee D-H, Seok M-Y, Zhao Y, Choi I-C, He J, Lu Z, Suh J-Y, Ramamurty U, Kawasaki M, Langdon TG, Jiang J-i. Spherical nanoindentation creep behavior of nanocrystalline and coarse-grained CoCrFeMnNi high-entropy alloys. *Acta Materialia*. 2016;109:314-22.
- [41] Hume-Rothery W. The structure of metals and alloys. 1937.
- [42] Guo S. Phase selection rules for cast high entropy alloys: an overview. *Materials Science and Technology*. 2015;31:1223-30.
- [43] Guo S, Hu Q, Ng C, Liu C. More than entropy in high-entropy alloys: Forming solid solutions or amorphous phase. *Intermetallics*. 2013;41:96-103.
- [44] Zhang Y, Zhou YJ, Lin JP, Chen GL, Liaw PK. Solid-solution phase formation rules for multi-component alloys. *Advanced Engineering Materials*. 2008;10:534-8.
- [45] Yang X, Zhang Y. Prediction of high-entropy stabilized solid-solution in multi-component alloys. *Materials Chemistry and Physics*. 2012;132:233-8.
- [46] Zhang Y, Yang X, Liaw P. Alloy design and properties optimization of high-entropy alloys. *JOM*. 2012;64:830-8.
- [47] Ramadass N. ABO_3 -type oxides—Their structure and properties—A bird's eye view. *Materials Science and Engineering*. 1978;36:231-9.
- [48] Ye Y, Wang Q, Lu J, Liu C, Yang Y. High-entropy alloy: challenges and prospects. *Materials Today*. 2016;19:349-62.
- [49] Senkov O, Miller J, Miracle D, Woodward C. Accelerated exploration of multi-principal element alloys with solid solution phases. *Nature Communications*. 2015;6:6529.
- [50] Santodonato LJ, Zhang Y, Feygenson M, Parish CM, Gao MC, Weber RJ, Neufeind JC, Tang Z, Liaw PK, Deviation from high-entropy configurations in the atomic distributions of a multi-principalelement alloy. *Nature Communications*. 2015;6:5964.

- [51] Ikeda T, Numakura H, Koiwa M. A Bragg–Williams model for the thermodynamic activity and the thermodynamic factor in diffusion for ordered alloys with substitutional defects. *Acta Materialia*. 1998;46:6605-13.
- [52] Fang S, Chen W, Fu Z. Microstructure and mechanical properties of twinned $\text{Al}_{0.5}\text{CrFeNiCo}_{0.5}\text{C}_{0.2}$ high entropy alloy processed by mechanical alloying and spark plasma sintering. *Materials & Design* 2014;54:973-9.
- [53] Hong Z, Morrison AP, Zhang H, Roberts SG, Grant PS. Development of a Novel Melt Spinning-Based Processing Route for Oxide Dispersion-Strengthened Steels. *Metallurgical and Materials Transactions A*. 2018;49:604-12.
- [54] Gludovatz B, George EP, Ritchie RO. Processing, microstructure and mechanical properties of the CrMnFeCoNi high-entropy alloy. *JOM*. 2015;67:2262-70.
- [55] Laplanche G, Gadaud P, Horst O, Otto F, Eggeler G, George E. Temperature dependencies of the elastic moduli and thermal expansion coefficient of an equiatomic, single-phase CoCrFeMnNi high-entropy alloy. *Journal of Alloys and Compounds*. 2015;623:348-53.
- [56] Haglund A, Koehler M, Catoor D, George E, Keppens V. Polycrystalline elastic moduli of a high-entropy alloy at cryogenic temperatures. *Intermetallics*. 2015;58:62-4.
- [57] Varshni Y. Temperature dependence of the elastic constants. *Physical Review B*. 1970;2:3952.
- [58] Wu Z, Bei H, Pharr GM, George EP. Temperature dependence of the mechanical properties of equiatomic solid solution alloys with face-centered cubic crystal structures. *Acta Materialia*. 2014;81:428-41.
- [59] Haasen P. Plastic deformation of nickel single crystals at low temperatures. *Philosophical Magazine*. 1958;3:384-418.

- [60] Ledbetter HM, Reed RP. Elastic Properties of Metals and Alloys, I. Iron, Nickel, and Iron-Nickel Alloys. *Journal of Physical and Chemical Reference Data*. 1973;2:531-618.
- [61] Patriarca L, Ojha A, Sehitoglu H, Chumlyakov Y. Slip nucleation in single crystal FeNiCoCrMn high entropy alloy. *Scripta Materialia*. 2016;112:54-7.
- [62] Seeger A. The temperature dependence of the critical shear stress and of work-hardening of metal crystals. *The London, Edinburgh, and Dublin Philosophical Magazine and Journal of Science*. 1954;45:771-3.
- [63] Laplanche G, Bonneville J, Varvenne C, Curtin W, George EP. Thermal activation parameters of plastic flow reveal deformation mechanisms in the CrMnFeCoNi high-entropy alloy. *Acta Materialia*. 2018;143:257-64.
- [64] Taylor GI. The mechanism of plastic deformation of crystals. Part I. Theoretical. *Proceedings of the Royal Society of London Series A, Containing Papers of a Mathematical and Physical Character*. 1934;145:362-87.
- [65] Leyson G, Hector L, Curtin W. First-principles prediction of yield stress for basal slip in Mg-Al alloys. *Acta Materialia*. 2012;60:5197-203.
- [66] Leyson G, Hector L, Curtin W. Solute strengthening from first principles and application to aluminum alloys. *Acta Materialia*. 2012;60:3873-84.
- [67] Varvenne C, Leyson G, Ghazisaeidi M, Curtin W. Solute strengthening in random alloys. *Acta Materialia*. 2017;124:660-83.
- [68] Bonneville J, Escaig B. Cross-slipping process and the stress-orientation dependence in pure copper. *Acta Metallurgica*. 1979;27:1477-86.
- [69] Kang K, Yin J, Cai W. Stress dependence of cross slip energy barrier for face-centered cubic nickel. *Journal of the Mechanics and Physics of Solids*. 2014;62:181-93.

- [70] Schuh B, Mendez-Martin F, Völker B, George E, Clemens H, Pippan R, Hohenwarter A, Mechanical properties, microstructure and thermal stability of a nanocrystalline CoCrFeMnNi highentropy alloy after severe plastic deformation. *Acta Materialia*. 2015;96:258-68.
- [71] Zhang H, He Y, Pan Y. Enhanced hardness and fracture toughness of the laser-solidified FeCoNiCrCuTiMoAlSiB_{0.5} high-entropy alloy by martensite strengthening. *Scripta Materialia*. 2013;69:342-5.
- [72] Diao H, Feng R, Dahmen K, Liaw P. Fundamental deformation behavior in high-entropy alloys: An overview. *Current Opinion in Solid State and Materials Science*. 2017;21:252-266.
- [73] Hutchings IM. The contributions of David Tabor to the science of indentation hardness. *Journal of Materials Research*. 2009;24:581-9.
- [74] Youssef KM, Zaddach AJ, Niu C, Irving DL, Koch CC. A novel low-density, high-hardness, high-entropy alloy with close-packed single-phase nanocrystalline structures. *Materials Research Letters*. 2015;3:95-9.
- [75] Liu W, Wu Y, He J, Nieh T, Lu Z. Grain growth and the Hall–Petch relationship in a high-entropy FeCrNiCoMn alloy. *Scripta Materialia*. 2013;68:526-9.
- [76] Burke J, Turnbull D. Recrystallization and grain growth. *Progress in Metal Physics*. 1952;3:220-292.
- [77] Burke J. Some factors affecting the rate of grain growth in metals. *AIME TRANS*. 1949;180:73-91.
- [78] Schino AD, Salvatori I, Kenny J. Effects of martensite formation and austenite reversion on grain refining of AISI 304 stainless steel. *Journal of Materials Science*. 2002;37:4561-5.
- [79] Otto F, Dlouhý A, Somsen C, Bei H, Eggeler G, George EP. The influences of temperature and microstructure on the tensile properties of a CoCrFeMnNi high-entropy alloy. *Acta Materialia*. 2013;61:5743-55.

- [80] Meyers MA, Mishra A, Benson DJ. Mechanical properties of nanocrystalline materials. *Progress in Materials Science*. 2006;51:427-556.
- [81] Tschopp M, Murdoch H, Kecske L, Darling K. "Bulk" nanocrystalline metals: review of the current state of the art and future opportunities for copper and copper alloys. *JOM*. 2014;66:1000-19.
- [82] Malow T, Koch C. Mechanical properties in tension of mechanically attrited nanocrystalline iron by the use of the miniaturized disk bend test. *Acta Materialia*. 1998;46:6459-73.
- [83] Abrahamson II E. *Surfaces and interfaces*. Syracuse Univ. Press. 1968.
- [84] Meyers MA, Ashworth E. A model for the effect of grain size on the yield stress of metals. *Philosophical Magazine A*. 1982;46:737-59.
- [85] Conrad H. Grain size dependence of the plastic deformation kinetics in Cu. *Materials Science and Engineering: A*. 2003;341:216-28.
- [86] Van Swygenhoven H, Spaczer M, Caro A. Microscopic description of plasticity in computer generated metallic nanophase samples: a comparison between Cu and Ni. *Acta Materialia*. 1999;47:3117-26.
- [87] Takaki S, Kawasaki K, Kimura Y. Mechanical properties of ultra fine grained steels. *Journal of Materials Processing Technology*. 2001;117:359-63.
- [88] Fu Z, Chen W, Wen H, Zhang D, Chen Z, Zheng B, Zhou Y, Lavernia EJ. Microstructure and strengthening mechanisms in an FCC structured single-phase nanocrystalline $\text{Co}_{25}\text{Ni}_{25}\text{Fe}_5\text{Al}_{7.5}\text{Cu}_{17.5}$ high-entropy alloy. *Acta Materialia*. 2016;107:59-71.
- [89] Chuang M-H, Tsai M-H, Wang W-R, Lin S-J, Yeh J-W. Microstructure and wear behavior of $\text{Al}_x\text{Co}_{1.5}\text{CrFeNi}_{1.5}\text{Ti}_y$ high-entropy alloys. *Acta Materialia*. 2011;59:6308-17.
- [90] Hadfield RA. Hadfield's manganese steel. *Science*. 1888;12:284-6.

- [91] Hutchinson B, Ridley N. On dislocation accumulation and work hardening in Hadfield steel. *Scripta Materialia*. 2006;55:299-302.
- [92] Yan F, Tao N, Lu K. Tensile ductility of nanotwinned austenitic grains in an austenitic steel. *Scripta Materialia*. 2014;84:31-4.
- [93] Bintu A, Vincze G, Picu CR, Lopes AB, Grácio JJ, Barlat F. Strain hardening rate sensitivity and strain rate sensitivity in TWIP steels. *Materials Science and Engineering: A*. 2015;629:54-9.
- [94] Byun T, Hashimoto N, Farrell K. Temperature dependence of strain hardening and plastic instability behaviors in austenitic stainless steels. *Acta Materialia*. 2004;52:3889-99.
- [95] Steinmetz DR, Jäpel T, Wietbrock B, Eisenlohr P, Gutierrez-Urrutia I, Saeed-Akbari A, Hickel T, Roters F, Raabe D. Revealing the strain-hardening behavior of twinning-induced plasticity steels: Theory, simulations, experiments. *Acta Materialia*. 2013;61:494-510.
- [96] Li Z, Zhao S, Diao H, Liaw P, Meyers M. High-velocity deformation of $\text{Al}_{0.3}\text{CoCrFeNi}$ high-entropy alloy: Remarkable resistance to shear failure. *Scientific Reports*. 2017;7:42742.
- [97] Li Z, Pradeep KG, Deng Y, Raabe D, Tasan CC. Metastable high-entropy dual-phase alloys overcome the strength–ductility trade-off. *Nature*. 2016;534:227-230.
- [98] Raabe D, Tasan CC, Springer H, Bausch M. From High-Entropy Alloys to High-Entropy Steels. *Steel Research International*. 2015;86:1127-38.
- [99] Lu L, Sui M, Lu K. Superplastic extensibility of nanocrystalline copper at room temperature. *Science*. 2000;287:1463-6.
- [100] Lu L, Shen Y, Chen X, Qian L, Lu K. Ultrahigh strength and high electrical conductivity in copper. *Science*. 2004;304:422-6.
- [101] Lu L, Chen X, Huang X, Lu K. Revealing the maximum strength in nanotwinned copper. *Science*. 2009;323:607-10.

- [102] Lu K. Making strong nanomaterials ductile with gradients. *Science*. 2014;345:1455-6.
- [103] Lu K. Stabilizing nanostructures in metals using grain and twin boundary architectures. *Nature Reviews Materials*. 2016;1:16019.
- [104] Liu Z, Meyers MA, Zhang Z, Ritchie RO. Functional gradients and heterogeneities in biological materials: Design principles, functions, and bioinspired applications. *Progress in Materials Science*. 2017.
- [105] Yang T, Zhao Y, Tong Y, Jiao Z, Wei J, Cai J, Han X, Chen D, Hu A, Kai J, Lu K, Liu Y, Liu CT. Multicomponent intermetallic nanoparticles and superb mechanical behaviors of complex alloys. *Science*. 2018;362:933-7.
- [106] Raynor D, Silcock J. Strengthening mechanisms in γ' precipitating alloys. *Metal Science Journal*. 1970;4:121-30.
- [107] Dastur YN, Leslie WC. Mechanism of work hardening in Hadfield manganese steel. *Metallurgical Transactions A*. 1981;12:749-59.
- [108] Li Z, Körmann F, Grabowski B, Neugebauer J, Raabe D. Ab initio assisted design of quinary dual-phase high-entropy alloys with transformation-induced plasticity. *Acta Materialia*. 2017.
- [109] Li Z, Raabe D. Influence of compositional inhomogeneity on mechanical behavior of an interstitial dual-phase high-entropy alloy. *Materials Chemistry and Physics*. 2017.
- [110] Li Z, Tasan CC, Pradeep KG, Raabe D. A TRIP-assisted dual-phase high-entropy alloy: Grain size and phase fraction effects on deformation behavior. *Acta Materialia*. 2017.
- [111] Gutierrez-Urrutia I, Raabe D. Dislocation and twin substructure evolution during strain hardening of an Fe–22wt.% Mn–0.6 wt.% C TWIP steel observed by electron channeling contrast imaging. *Acta Materialia*. 2011;59:6449-62.

- [112] Shun T-T, Du Y-C. Microstructure and tensile behaviors of FCC Al_{0.3}CoCrFeNi high entropy alloy. *Journal of Alloys and Compounds*. 2009;479:157-60.
- [113] He J, Wang H, Huang H, Xu X, Chen M, Wu Y, Liu XJ, Nieh TG, An K, Lu ZP. A precipitationhardened high-entropy alloy with outstanding tensile properties. *Acta Materialia*. 2016;102:187-96.
- [114] Varvenne C, Luque A, Curtin WA. Theory of strengthening in fcc high entropy alloys. *Acta Materialia*. 2016;118:164-76.
- [115] Zhang Z, Sheng H, Wang Z, Gludovatz B, Zhang Z, George EP, Yu Q, Mao SX, Ritchie RO. Dislocation mechanisms and 3D twin architectures generate exceptional strength-ductility-toughness combination in CrCoNi medium-entropy alloy. *Nature Communications*. 2017;8:14390.
- [116] Rohatgi A, Vecchio KS, Gray GT. The influence of stacking fault energy on the mechanical behavior of Cu and Cu-Al alloys: deformation twinning, work hardening, and dynamic recovery. *Metallurgical and Materials Transactions A*. 2001;32:135-45.
- [117] Meyers MA, Schneider M, Jarmakani H, Kad B, Remington B, Kalantar D, Mcnaney J, Cao B, Wark J. Deformation substructures and their transitions in laser shock–compressed copper-aluminum alloys. *Metallurgical and Materials Transactions A*. 2008;39:304-21.
- [118] Zaddach A, Niu C, Koch C, Irving D. Mechanical properties and stacking fault energies of NiFeCrCoMn high-entropy alloy. *JOM*. 2013;65:1780-9.
- [119] Reed R, Schramm R. Relationship between stacking-fault energy and x-ray measurements of stacking-fault probability and microstrain. *Journal of Applied Physics*. 1974;45:4705-11.
- [120] Schramm RE, Reed RP. Stacking fault energies of fcc fe-Ni alloys by x-ray diffraction line profile analysis. *Metallurgical Transactions A*. 1976;7:359-63.

- [121] Huang S, Li W, Lu S, Tian F, Shen J, Holmström E, Vitos L. Temperature dependent stacking fault energy of FeCrCoNiMn high entropy alloy. *Scripta Materialia*. 2015;108:44-7.
- [122] Smith T, Hooshmand M, Esser B, Otto F, McComb D, George E, Ghazisaeidi M, Mills MJ. Atomic-scale characterization and modeling of 60° dislocations in a high-entropy alloy. *Acta Materialia*. 2016;110:352-63.
- [123] Laplanche G, Horst O, Otto F, Eggeler G, George E. Microstructural evolution of a CoCrFeMnNi high-entropy alloy after swaging and annealing. *Journal of Alloys and Compounds*. 2015;647:548-57.
- [124] Meyers MA, Vöhringer O, Lubarda VA. The onset of twinning in metals: a constitutive description. *Acta Materialia*. 2001;49:4025-39.
- [125] Narita N, Takamura J-I. Deformation twinning in fcc and bcc metals. *Dislocations in Solids*. 1992;9:135-69.
- [126] Laplanche G, Kostka A, Horst O, Eggeler G, George E. Microstructure evolution and critical stress for twinning in the CrMnFeCoNi high-entropy alloy. *Acta Materialia*. 2016;118:152-63.
- [127] Zerilli FJ, Armstrong RW. Dislocation - mechanics - based constitutive relations for material dynamics calculations. *Journal of Applied Physics*. 1987;61:1816-25.
- [128] Wang B, Fu A, Huang X, Liu B, Liu Y, Li Z, Zan X. Mechanical properties and microstructure of the CoCrFeMnNi high entropy alloy under high strain rate compression. *Journal of Materials Engineering and Performance*. 2016;25:2985-92.
- [129] Zerilli FJ, Armstrong RW. The effect of dislocation drag on the stress-strain behavior of FCC metals. *Acta Metallurgica et Materialia*. 1992;40:1803-8.
- [130] Christian JW, Mahajan S. Deformation twinning. *Progress in Materials Science*. 1995;39:1-157.
- [131] Zhu Y, Liao X, Wu X. Deformation twinning in nanocrystalline materials. *Progress in Materials Science*. 2012;57:1-62.

- [132] Cohen J, Weertman J. A dislocation model for twinning in fcc metals. *Acta Metallurgica*. 1963;11:996-8.
- [133] Zhang Z, Li L, Zhang Z, Zhang P. Twin boundary: Controllable interface to fatigue cracking. *Journal of Materials Science & Technology*. 2017;33:603-6.
- [134] Meyers M. The formation of annealing twins: overview and new thoughts. *Interface Migration and Control of Microstructure*. 1984:99-123.
- [135] Meyers MA, Murr LE. A model for the formation of annealing twins in F.C.C. metals and alloys. *Acta Metallurgica*. 1978;26:951-62.
- [136] Ritchie RO, Thompson AW. On macroscopic and microscopic analyses for crack initiation and crack growth toughness in ductile alloys. *Metallurgical Transactions A*. 1985;16:233-48.
- [137] Rice JR. A path independent integral and the approximate analysis of strain concentration by notches and cracks. *ASME*. 1968.
- [138] Rice JR. Some remarks on elastic crack-tip stress fields. *International Journal of Solids and Structures*. 1972;8:751-8.
- [139] Rice J, Paris P, Merkle J. Some further results of J-integral analysis and estimates. *Progress in flaw growth and fracture toughness testing: ASTM International*. 1973.
- [140] Begley J, Landes J. The J integral as a fracture criterion. *Fracture Toughness: Part II: ASTM International*. 1972.
- [141] Knott JF. Fundamentals of fracture mechanics: Gruppo Italiano Frattura. 1973.
- [142] Shih C. Relationships between the J-integral and the crack opening displacement for stationary and extending cracks. *Journal of the Mechanics and Physics of Solids*. 1981;29:305-26.
- [143] Ritchie RO. Mechanisms of fatigue-crack propagation in ductile and brittle solids. *Int J Fracture*. 1999;100:55-83.

- [144] Zhang Z, Mao M, Wang J, Gludovatz B, Zhang Z, Mao SX, George EP, Yu Q, Ritchie RO. Nanoscale origins of the damage tolerance of the high-entropy alloy CrMnFeCoNi. *Nature Communications*. 2015;10:1038.
- [145] Gludovatz B, Hohenwarter A, Thurston KV, Bei H, Wu Z, George EP, Ritchie RO. Exceptional damage-tolerance of a medium-entropy alloy CrCoNi at cryogenic temperatures. *Nature Communications*. 2016;7:10602.
- [146] Wu Y, Cai Y, Wang T, Si J, Zhu J, Wang Y, Hui X, A refractory $Hf_{25}Nb_{25}Ti_{25}Zr_{25}$ high-entropy alloy with excellent structural stability and tensile properties. *Materials Letters*. 2014;130:277-80.
- [147] Ritchie RO. Influence of microstructure on near-threshold fatigue-crack propagation in ultra-high strength steel. *Metal Science*. 1977;11:368-81.
- [148] Paris PC, Erdogan F. A critical analysis of crack propagation laws. *ASME*. 1963.
- [149] Seifi M, Li D, Yong Z, Liaw PK, Lewandowski JJ. Fracture toughness and fatigue crack growth behavior of as-cast high-entropy alloys. *JOM*. 2015;67:2288-95.
- [150] Thurston KV, Gludovatz B, Hohenwarter A, Laplanche G, George EP, Ritchie RO. Effect of temperature on the fatigue-crack growth behavior of the high-entropy alloy CrMnFeCoNi. *Intermetallics*. 2017;88:65-72.
- [151] Hemphill MA, Yuan T, Wang G, Yeh J, Tsai C, Chuang A, Liaw PK. Fatigue behavior of $Al_{0.5}CoCrCuFeNi$ high entropy alloys. *Acta Materialia*. 2012;60:5723-34.
- [152] Yasuda HY, Shigeno K, Nagase T. Dynamic strain aging of $Al_{0.3}CoCrFeNi$ high entropy alloy single crystals. *Scripta Materialia*. 2015;108:80-3.
- [153] Mulford R, Kocks U. New observations on the mechanisms of dynamic strain aging and of jerky flow. *Acta Metallurgica*. 1979;27:1125-34.

- [154] Komarasamy M, Alagarsamy K, Mishra RS. Serration behavior and negative strain rate sensitivity of $\text{Al}_{0.1}\text{CoCrFeNi}$ high entropy alloy. *Intermetallics*. 2017;84:20-4.
- [155] Yoshinaga H, Morozumi S. A Portevin-Le Chatelier effect expected from solute atmosphere dragging. *Philosophical Magazine*. 1971;23:1351-66.
- [156] Suzuki H. Chemical interaction of solute atoms with dislocations. *Science reports of the Research Institutes, Tohoku University Ser A, Physics, chemistry and metallurgy*. 1952;4:455-63.
- [157] Aboulfadl H, Deges J, Choi P, Raabe D. Dynamic strain aging studied at the atomic scale. *Acta Materialia*. 2015;86:34-42.
- [158] Zhang Y, Liu JP, Chen SY, Xie X, Liaw PK, Dahmen KA, Qiao JW, Wang YL. Serration and noise behavior in materials. *Progress in Materials Science*. 2017;90:358-460
- [159] Carroll R, Lee C, Tsai C-W, Yeh J-W, Antonaglia J, Brinkman BA, LeBlanc1 M, Xie X, Chen S, Liaw PK, Dahmen KA. Experiments and model for serration statistics in low-entropy, medium-entropy, and high-entropy alloys. *Scientific Reports*. 2015;5:16997.
- [160] Cottrell AH, Bilby B. Dislocation theory of yielding and strain ageing of iron. *Proceedings of the Physical Society Section A*. 1949;62:49.
- [161] Senkov O, Wilks G, Miracle D, Chuang C, Liaw P. Refractory high-entropy alloys. *Intermetallics*. 2010;18:1758-65.
- [162] Senkov O, Wilks G, Scott J, Miracle D. Mechanical properties of $\text{Nb}_{25}\text{Mo}_{25}\text{Ta}_{25}\text{W}_{25}$ and $\text{V}_{20}\text{Nb}_{20}\text{Mo}_{20}\text{Ta}_{20}\text{W}_{20}$ refractory high entropy alloys. *Intermetallics*. 2011;19:698-706.
- [163] Lu Y, Dong Y, Guo S, Jiang L, Kang H, Wang T, Wen B, Wang Z, Jie J, Cao Z, Ruan H, Li T. A promising new class of high-temperature alloys: eutectic high-entropy alloys. *Scientific Reports*. 2014;4:6200.

- [164] Senkov O, Senkova S, Woodward C. Effect of aluminum on the microstructure and properties of two refractory high-entropy alloys. *Acta Materialia*. 2014;68:214-28.
- [165] Gorr B, Azim M, Christ H-J, Mueller T, Schliephake D, Heilmaier M. Phase equilibria, microstructure, and high temperature oxidation resistance of novel refractory high-entropy alloys. *Journal of Alloys and Compounds*. 2015;624:270-8.
- [166] Ashby MF. A first report on deformation-mechanism maps. *Acta Metallurgica*. 1972;20:887-97.
- [167] Langdon TG, Mohamed FA. A simple method of constructing an Ashby-type deformation mechanism map. *Journal of Materials Science*. 1978;13:1282-90.
- [168] Kang YB, Shim SH, Lee KH, Hong SI. Dislocation creep behavior of CoCrFeMnNi high entropy alloy at intermediate temperatures. *Materials Research Letters*. 2018;6(12):689-95.
- [169] Nabarro FRN, De Villiers F. Physics of creep and creep-resistant alloys. CRC press. 1995.
- [170] Langdon TG. Dependence of creep rate on porosity. *Journal of the American Ceramic Society*. 1972;55:630-1.
- [171] Wazzan AR. Lattice and Grain Boundary Self-Diffusion in Nickel. *Journal of Applied Physics*. 1965;36:3596-9.
- [172] Langdon T. A unified approach to grain boundary sliding in creep and superplasticity. *Acta Metallurgica et Materialia*. 1994;42:2437-43.
- [173] Shahmir H, He J, Lu Z, Kawasaki M, Langdon TG. Evidence for superplasticity in a CoCrFeNiMn high-entropy alloy processed by high-pressure torsion. *Materials Science and Engineering: A*. 2017.
- [174] Greer JR, Oliver WC, Nix WD. Size dependence of mechanical properties of gold at the micron scale in the absence of strain gradients. *Acta Materialia*. 2005;53:1821-30.

- [175] Greer JR, Nix WD. Nanoscale gold pillars strengthened through dislocation starvation. *Physical Review B*. 2006;73:245410.
- [176] Greer JR, De Hosson JTM. Plasticity in small-sized metallic systems: Intrinsic versus extrinsic size effect. *Progress in Materials Science*. 2011;56:654-724.
- [177] Giwa AM, Liaw PK, Dahmen KA, Greer JR. Microstructure and small-scale size effects in plasticity of individual phases of Al 0.7 CoCrFeNi High Entropy alloy. *Extreme Mechanics Letters*. 2016;8:220-8.
- [178] Kim J-Y, Jang D, Greer JR. Tensile and compressive behavior of tungsten, molybdenum, tantalum and niobium at the nanoscale. *Acta Materialia*. 2010;58:2355-63.
- [179] Schneider A, Kaufmann D, Clark B, Frick C, Gruber P, Mönig R, Kraft O, Arzt E. Correlation between critical temperature and strength of small-scale bcc pillars. *Physical Review Letters*. 2009;103:105501.
- [180] Zou Y, Maiti S, Steurer W, Spolenak R. Size-dependent plasticity in an Nb₂₅Mo₂₅Ta₂₅W₂₅ refractory high-entropy alloy. *Acta Materialia*. 2014;65:85-97.
- [181] Zou Y, Wheeler JM, Ma H, Okle P, Spolenak R. Nanocrystalline high entropy alloys: A new paradigm in high temperature strength and stability. *Nano Letters*. 2017.
- [182] Zou Y, Ma H, Spolenak R. Ultrastrong ductile and stable high-entropy alloys at small scales. *Nature Communications*. 2015;6:7748.
- [183] Meyers MA, Taylor Aimone C. Dynamic fracture (spalling) of metals. *Progress in Materials Science*. 1983;28:1-96.
- [184] Culver RS. Thermal instability strain in dynamic plastic deformation. *Metallurgical effects at high strain rates*. Springer. 1973:519-30.

- [185] Meyers MA, Nesterenko VF, LaSalvia JC, Xue Q. Shear localization in dynamic deformation of materials: microstructural evolution and self-organization. *Materials Science and Engineering: A.* 2001;317:204-25.
- [186] Meyers MA , Li Z, Zhao S, Wang B, Liu Y, Liaw PK. shear localization of fcc high-entropy alloys, *EPJ Web of Conferences*, 2018;183:03028.
- [187] Jiang Z, He J, Wang H, Zhang H, Lu Z, Dai L. Shock compression response of high entropy alloys. *Materials Research Letters*. 2016;4:226-32.
- [188] Wu W, Ni S, Liu Y, Liu B, Song M. Amorphization at twin-twin intersected region in FeCoCrNi high-entropy alloy subjected to high-pressure torsion. *Materials Characterization*. 2017;127:111-5.
- [189] Zhao S, Hahn E, Kad B, Remington B, Wehrenberg C, Bringa E, Meyers MA. Amorphization and nanocrystallization of silicon under shock compression. *Acta Materialia*. 2016;103:519-533.
- [190] Remington TP, Remington BA, Hahn EN, Meyers MA. Deformation and failure in extreme regimes by high-energy pulsed lasers: A review. *Materials Science and Engineering: A.* 2017;688:429-58.
- [191] Zhao S, Kad B, Wehrenberg CE, Remington BA, Hahn EN, More KL, Meyers MA. Generating gradient germanium nanostructures by shock-induced amorphization and crystallization. *Proceedings of the National Academy of Sciences*. 2017;114:9791-9796.
- [192] Zhao S, Kad B, Hahn EN, Remington BA, Wehrenberg CE, Huntington CM, Park H-S, Bringa EM, More KL, Meyers MA. Pressure and shear-induced amorphization of silicon. *Extreme Mechanics Letters*. 2015;5:74-80.
- [193] Zhao S, Kad B, Remington BA, LaSalvia JC, Wehrenberg CE, Behler KD, Meyers MA. Directional amorphization of boron carbide subjected to laser shock compression. *Proceedings of the National Academy of Sciences*. 2016;113:12088-93.

- [194] Zhao S, Li Z, Diao H, Liaw PK, Wehrenberg CE, Remington BA, Meyers MA, in preparation.
- [195] Zhao S, Li Z, Zhu C, Wehrenberg CE, Remington BA, Yang W, Ritchie RO, Meyers MA, in preparation.
- [196] Meyers MA, Traiviratana S, Lubarda V, Benson DJ, Bringa EM. The role of dislocations in the growth of nanosized voids in ductile failure of metals. *JOM*. 2009;61:35-41.
- [197] Li Z, Zhao S, Alotaibi SM, Liu Y, Wang B, Meyers MA, Adiabatic shear localization in CrMnFeCoNi HEA, *Acta Materilia* 2018;151:424-431.
- [198] Hughes G, Smith S, Pande C, Johnson H, Armstrong R. Hall-Petch strengthening for the microhardness of twelve nanometer grain diameter electrodeposited nickel. *Scripta Metallurgica*. 1986;20:93-7.
- [199] Hahn EN, Meyers MA. Grain-size dependent mechanical behavior of nanocrystalline metals. *Materials Science and Engineering: A*. 2015;646:101-34.
- [200] Beyerlein IJ, Zhang X, Misra A. Growth twins and deformation twins in metals. *Annual Review of Materials Research*. 2014;44:329-63.
- [201] Gleiter H. The formation of annealing twins. *Acta Metallurgica*. 1969;17:1421-8.
- [202] Coble R. A model for boundary diffusion controlled creep in polycrystalline materials. *Journal of Applied Physics*. 1963;34:1679-82.
- [203] Mukherjee AK, Bird JE, Dorn JE. Experimental corrections for high-temperature creep, *Transactions of American Society for Metals*. 1969;62:155.
- [204] Tracy CL, Park S, Rittman DR, Zinkle SJ, Bei H, Lang M, Ewing RC, Mao WL. High pressure synthesis of a hexagonal close-packed phase of the high-entropy alloy CrMnFeCoNi. *Nature Communications*. 2017;8:15634.

[205] Horn RM, Ritchie RO. Mechanisms of tempered martensite embrittlement in low alloy steels. Metallurgical Transactions A. 1978;9(8):1039-53.

Table 1. Evolution of structure and ordering of Al _{1.3} CrFeCoNiCu [50]			
Temperature range	Microstructure	Volume fraction (%), phase, composition	Atomic distribution
Above 1,315 °C		100%, liquid (L), Al _{1.3} CoCrCuFeNi	Preferred nearest-neighbour pair correlations: Al-Ni; Cr-Fe; Cu-Cu
1,230 to 1,315 °C		(100 - F)% liquid, Cu rich + F%, BCC, Al _{1.3} CoCrCu _{1-x} FeNi*	Liquid plus BCC crystals, with CSRO $1.73R \leq (\Delta S_{\text{mix}}^{\text{conf}})_{\text{BCC}} \leq 1.79R$
1,080 to 1,230 °C		95%, {B2} matrix [†] , Al _{1.3} CoCrCu _{0.7} FeNi + 5% liquid, Cu-rich ID region	{B2} matrix plus liquid. Order: $\eta_{\text{Al}} = 0.93$ $\eta_{\text{TM}} = -0.29$ $1.63R \leq (\Delta S_{\text{mix}}^{\text{conf}})_{\text{(B2)}} \leq 1.73R$
600 to 1,080 °C		85%, {B2} matrix, Al _{1.3} CoCrCu _{0.1} FeNi + 10%, FCC rods (r), Cu rich [‡] + 5%, FCC solid ID, Cu rich	FCC phases treated as pure Cu, with $(\Delta S_{\text{mix}}^{\text{conf}})_{\text{FCC}} \sim 0$ $(\Delta S_{\text{mix}}^{\text{conf}})_{\text{(B2)}} = 1.50R$ $\eta_{\text{Al}} = 0.93, \eta_{\text{TM}} = -0.29$
Room temperature to 600 °C		84%, spinodal BCC/{B2}, [Co _{0.2} CrFe _{0.5}]/[Al _{1.3} Co _{0.8} Fe _{0.5} Ni] + 10%, FCC rods + 5%, FCC ID, Cu rich + 1%, nanoprecipitates, Cu rich [‡]	Spinodal BCC/{B2}-ordered phase: $\eta_{\text{Al}} = 0.73$ $\eta_{\text{Ni}} = \eta_{\text{Co}} = -0.60$ $\eta_{\text{Fe}} = 0.24$ $(\Delta S_{\text{mix}}^{\text{conf}})_{\text{alloy}} = 0.89R$

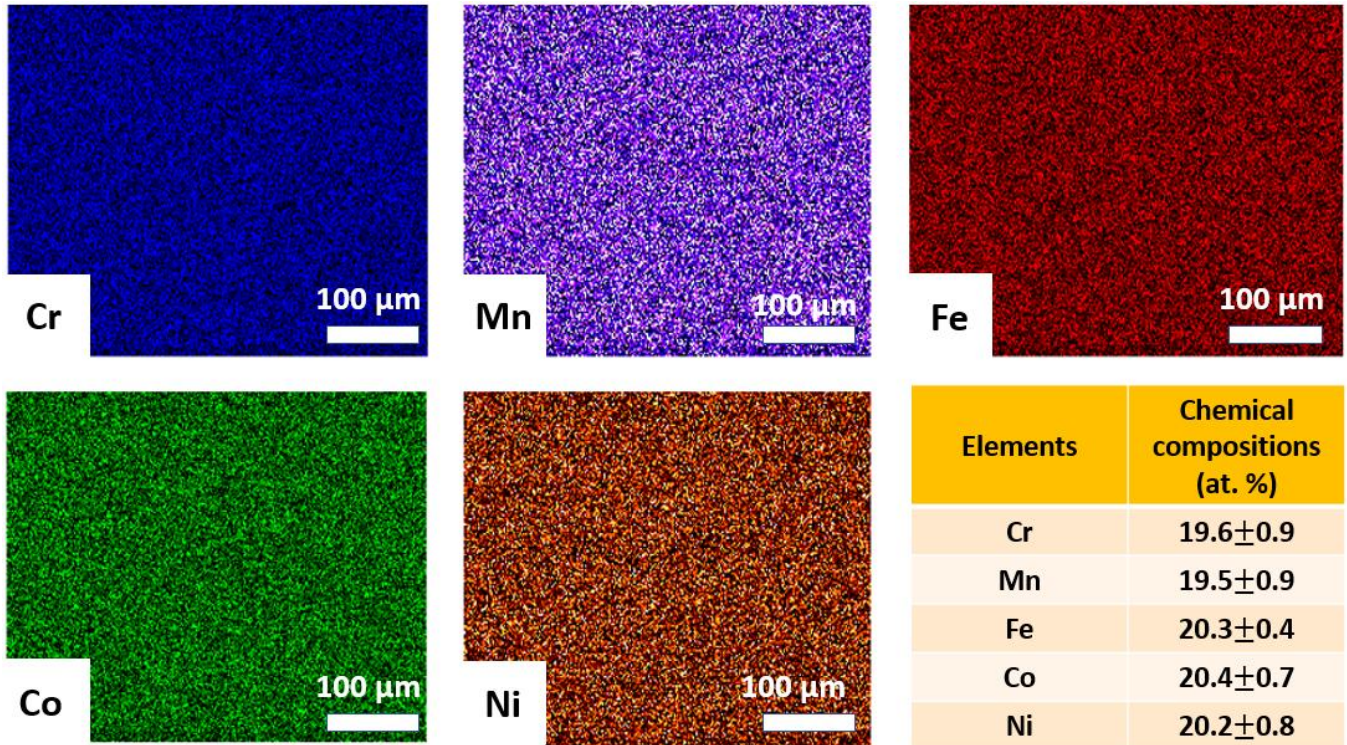


Fig. 1. Composition maps (by SEM-EDX) for the five elements that comprise the CrMnFeCoNi HEA [197].

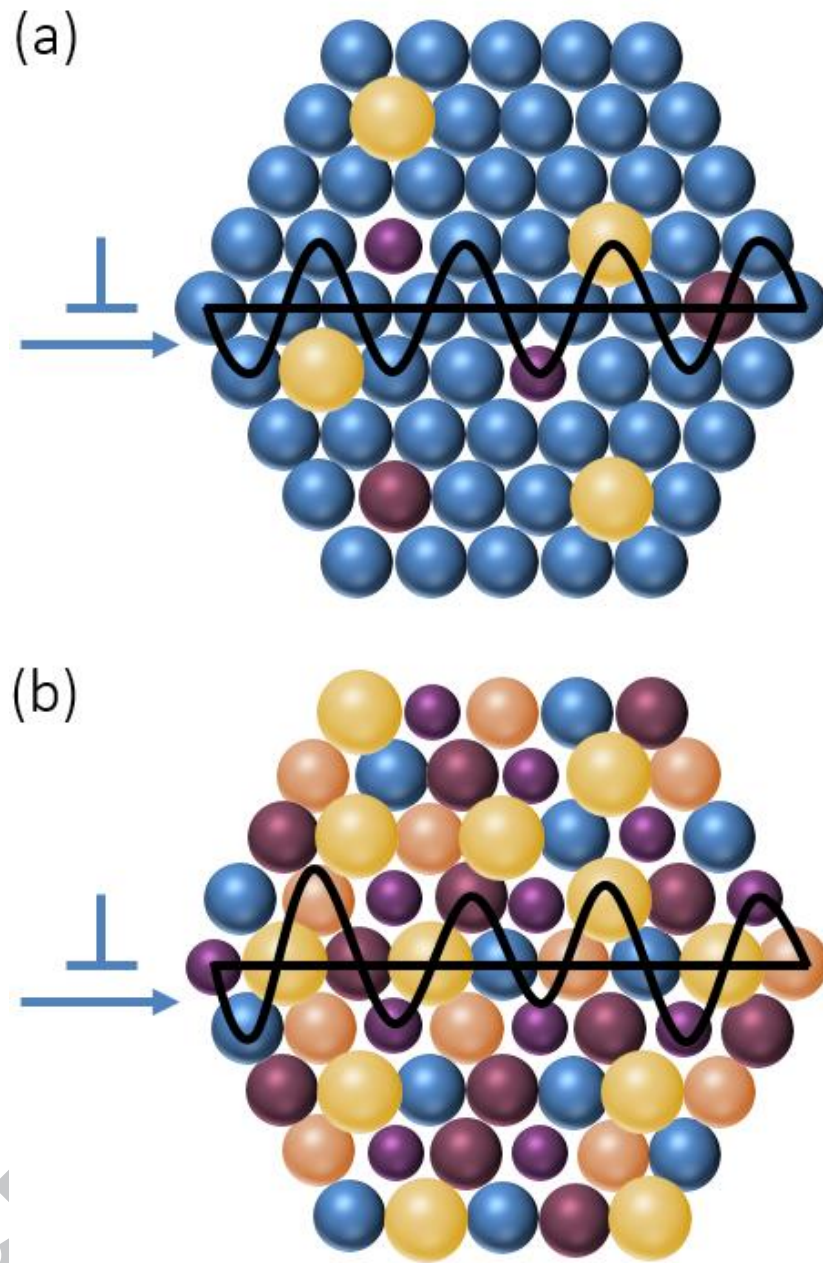


Fig. 2. Schematic drawing showing dislocation motion by overcoming periodic Peierls-Nabarro energy barrier field in (a) a dilute solid-solution, and (b) a complex, concentrated solid solution with five elements. Note the distortions in lattice and variation in Peierls-Nabarro energy fluctuations for HEAs.

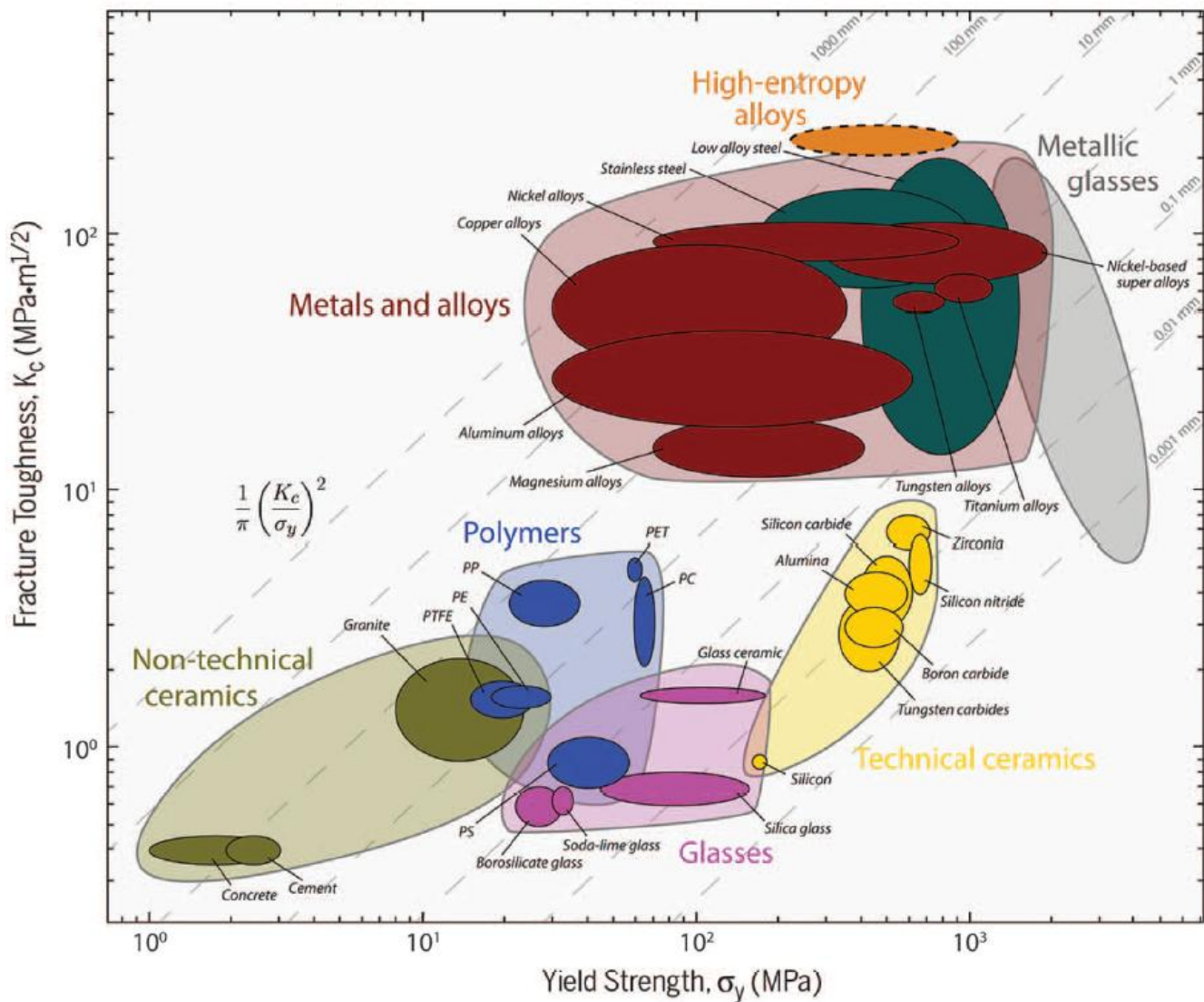


Fig. 3. Ashby plot of fracture toughness vs. yield strength plot of the most commonly used structural materials. HEAs (top right) show an outstanding combination of damage-tolerant mechanical properties compared with other materials [15].

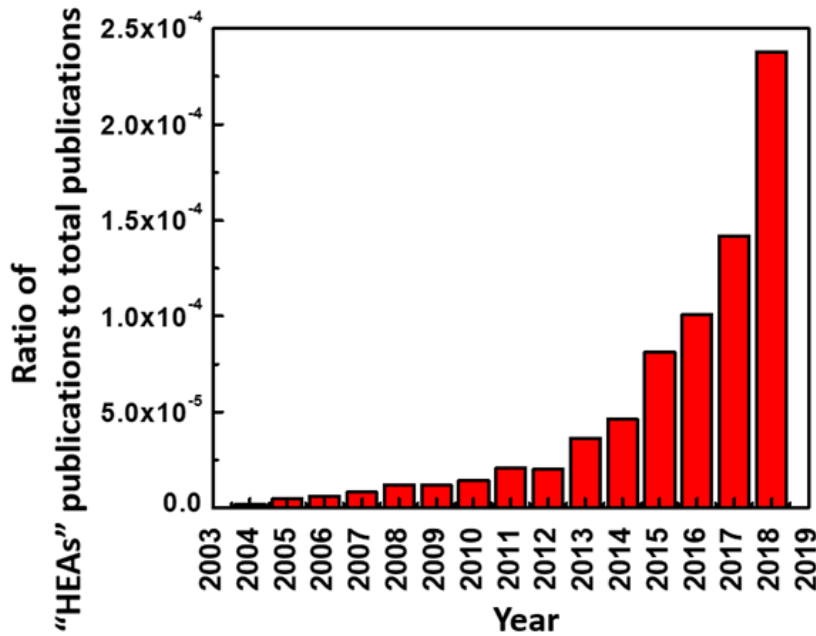


Fig. 4. Ratio of the number of publications under the heading “high-entropy alloy” to the total number of Elsevier publications keeps increasing dramatically over the past decade, from 2×10^{-5} (20 per million) in 2009 to 2.4×10^{-4} (240 per million) in 2018, suggesting the prominence of this new alloy design philosophy. In absolute numbers, 900 papers were published in 2018. (data from the *Web of Science*)

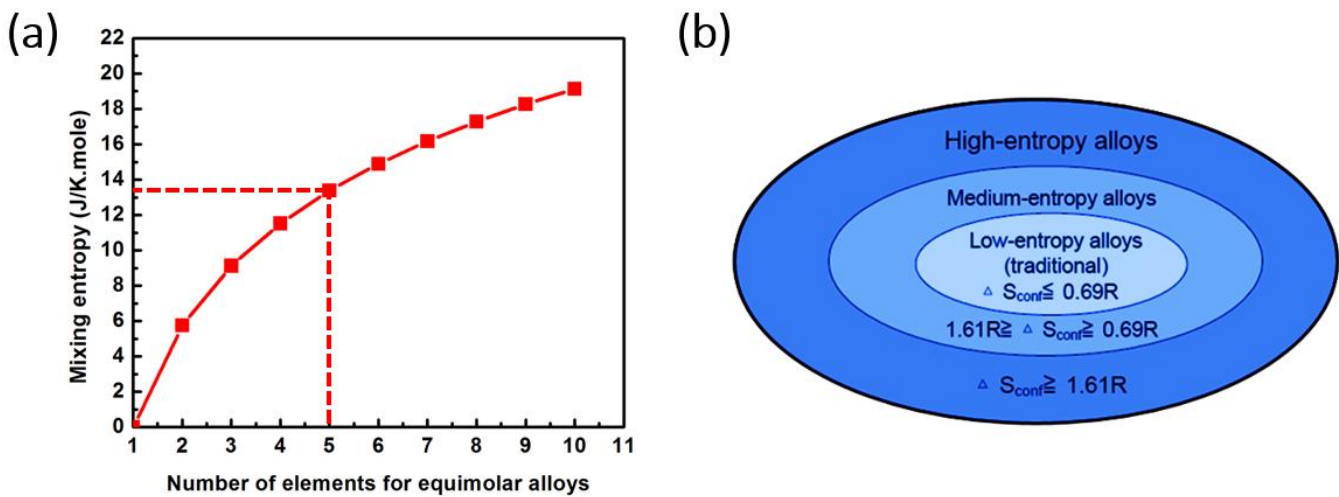


Fig. 5. (a) Influence of number of equimolar elements on the mixing entropy of the system. Mixing entropy for five equiatomic elements corresponds to $1.61R$ ($R=8.314 \text{ J.mol.K}^{-1}$). (b) The alloy systems classified according to the configurational entropy [25].

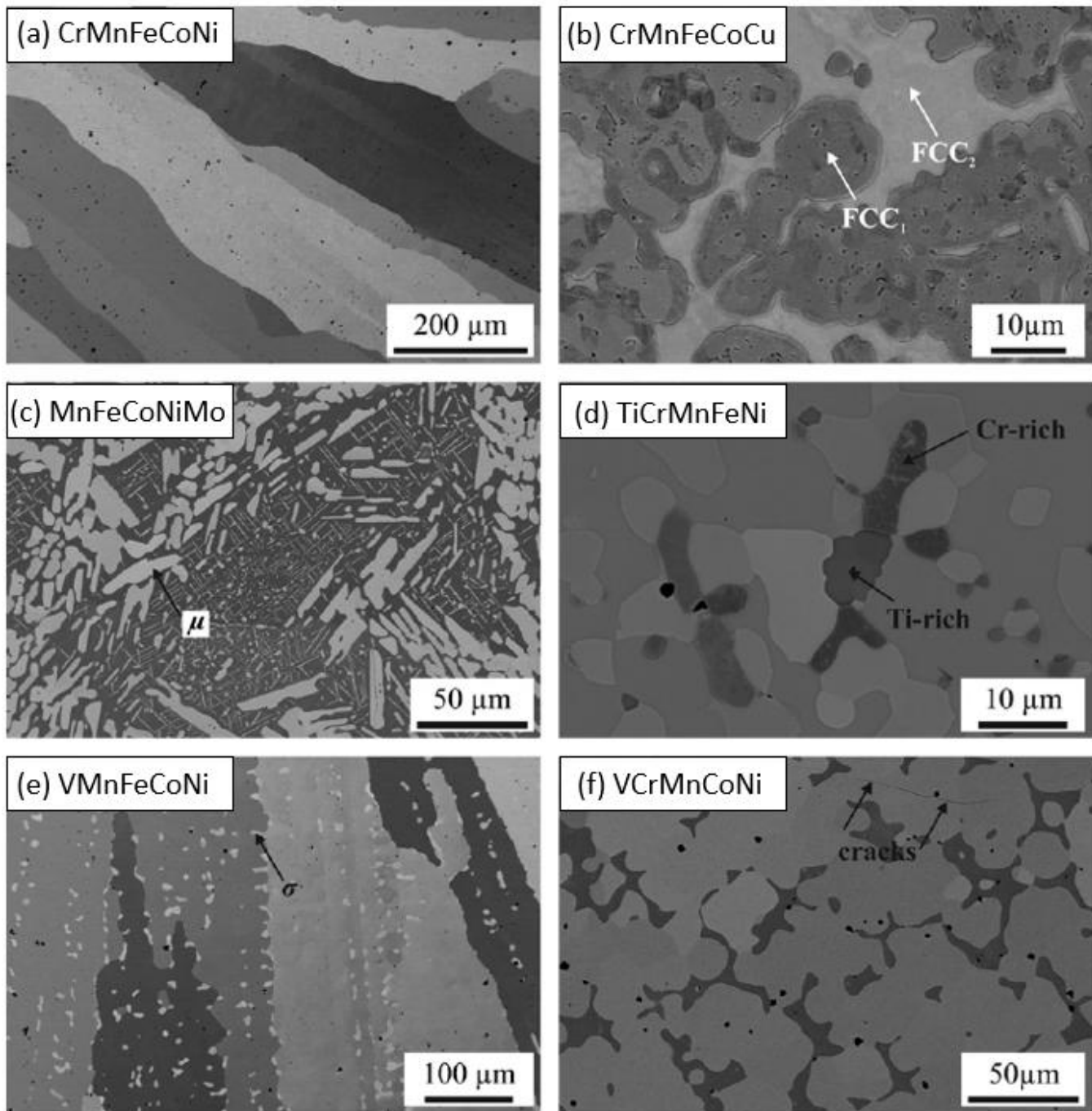


Fig. 6. Backscattered electron (BSE) images of the annealed microstructure of the six multicomponent equiatomic alloys: (a) CrMnFeCoNi HEA, (b) CrMnFeCoCu HEA, (c) MnFeCoNiMo HEA, (d) TiCrMnFeNi HEA, (e) VMnFeCoNi HEA, and (f) VCrMnCoNi HEA [27]. Only the CrMnFeCoNi HEA comprises a homogeneous single phase.

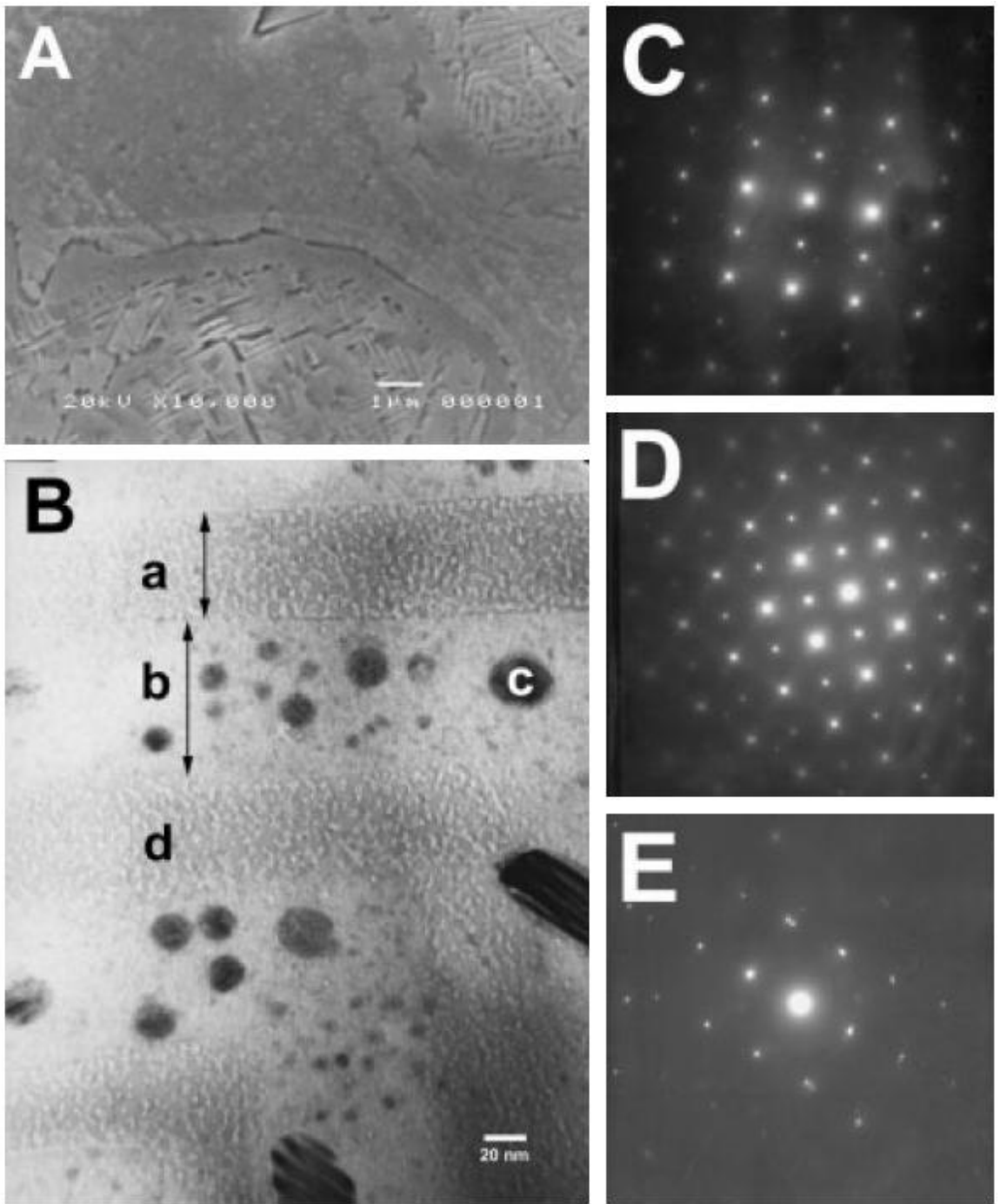


Fig. 7. Microstructure of the AlCrFeCoNiCu alloy. (A) alloys containing multiple phases. (B) Bright-field TEM image; (B-a) the nano-sized spinodal plate with the *bcc* structure. (B-b) nano-sized spinodal plates with the *bcc* structure. (B-c) nano-sized precipitation inside the spinodal plate, which was close to the *fcc* structure; (B-d) nano-sized precipitation inside the spinodal plate with the *bcc* structure. (C-E) The selected area diffraction (SAD) patterns of (B), (B-a), and (B-b) [3].

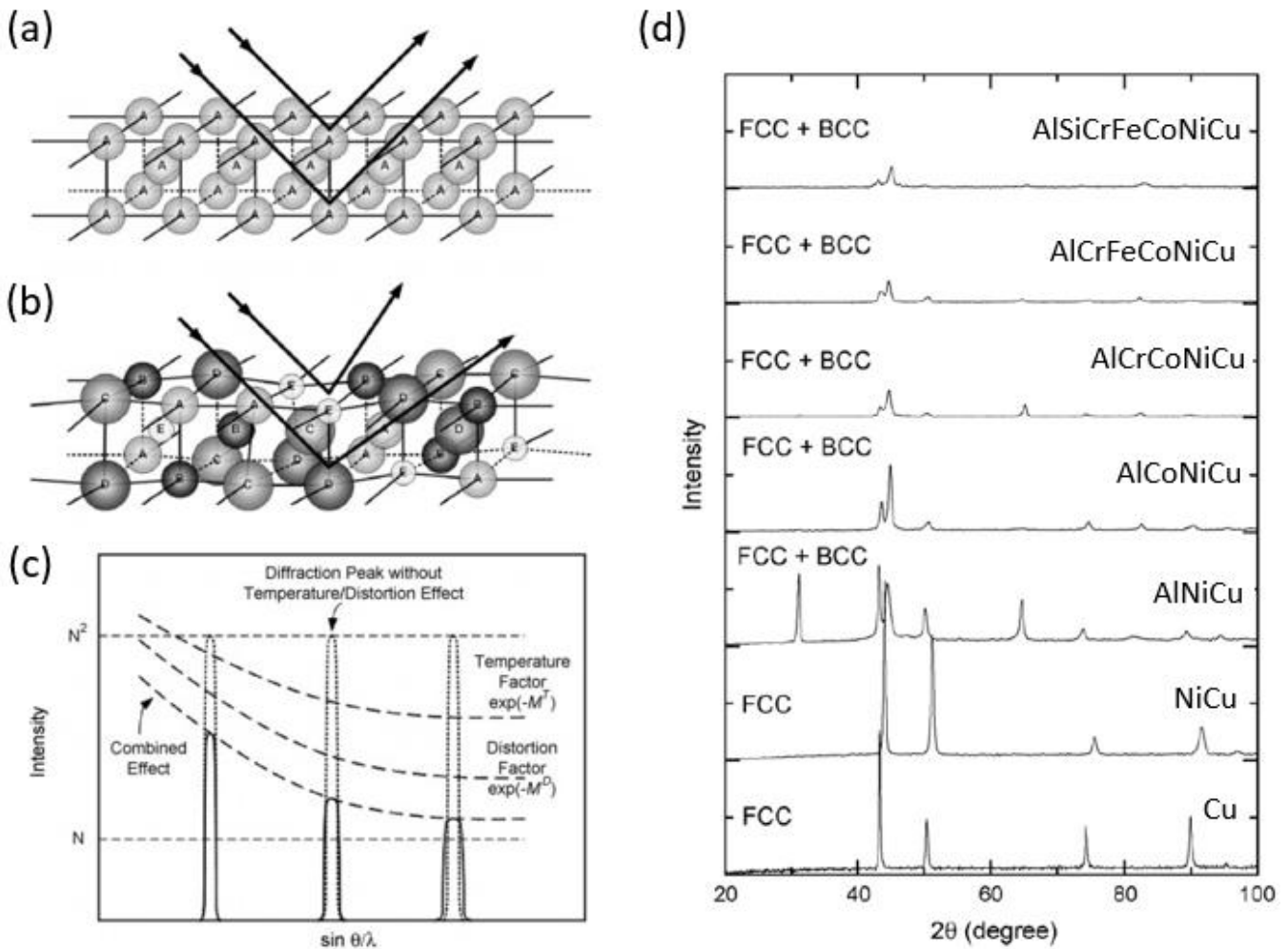
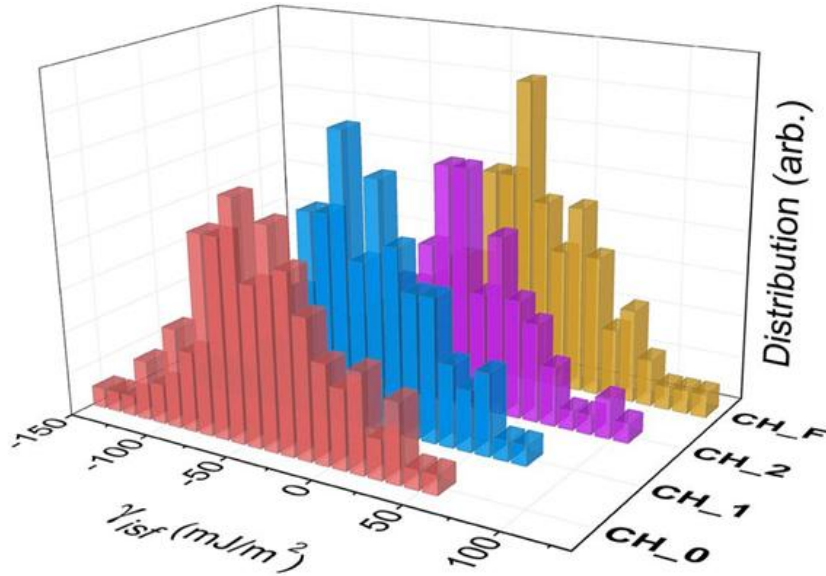
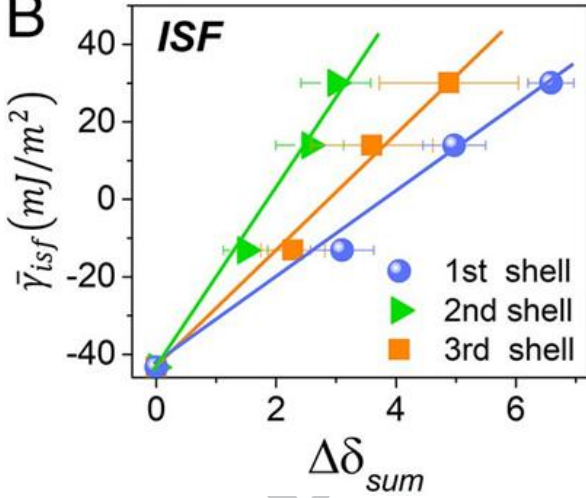


Fig. 8. Lattice-distortion effect on XRD intensities: (a) schematic drawing of perfect crystal structure with pure metals, (b) HEAs with different sized atoms in lattice sites, (c) influence of the temperature and lattice-distortion on the peak intensity of XRD results through $\exp(M^T)$ and $\exp(M^D)$, respectively, and (d) experimental results of the XRD patterns of the HEAs with the increase of the number of the principal elements [30].

A



B



C

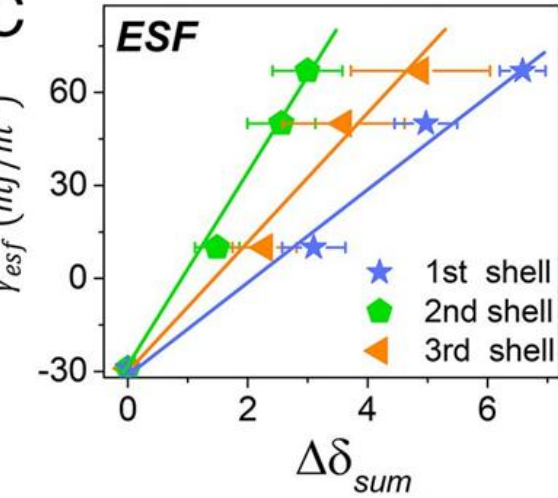


Fig. 9. Stacking fault energy variation with local chemical ordering. (A) Distribution of intrinsic stacking fault energy, γ_{isf} , for equimolar CrCoNi alloys in four specific states, *i.e.*, CH_0 , CH_1 , CH_2 and CH_F , which expand from random solid solution to the highest degree of chemical ordering. Totally 108 stacking faults were considered for analysis in each group. The average energy, intrinsic stacking fault energy $\bar{\gamma}_{isf}$ and extrinsic stacking fault energy $\bar{\gamma}_{esf}$ in (B) and (C), respectively, among those four groups were correlated with the total nonproportional number of local atomic pairs, sum $\Delta\delta$ for the first, second and third nearest-neighbor shells [33]. The conclusion here is that the stacking-fault energy of the CrCoNi alloy is strongly dependent on the degree of local chemical order.

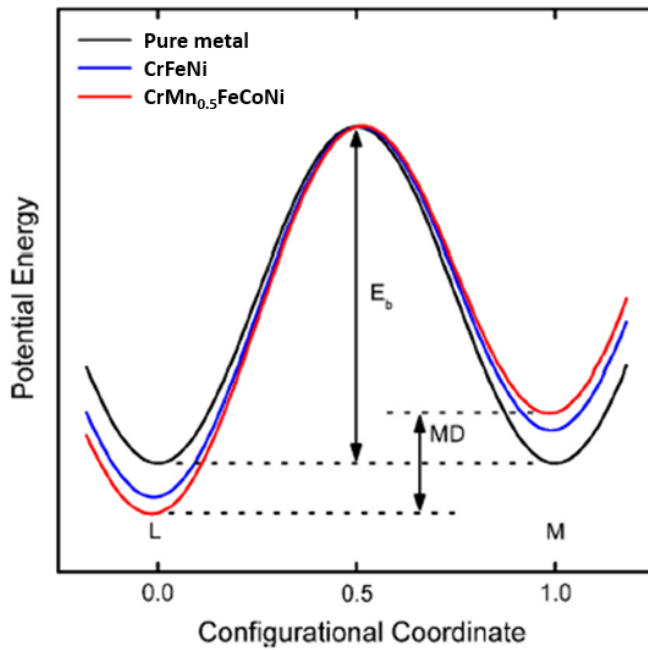


Fig. 10. Schematic drawing showing the lattice potential energy (LPE) and mean difference when a Ni atom migrates in pure metal, CrFeNi alloy, and CrMn_{0.5}FeCoNi HEA [38].

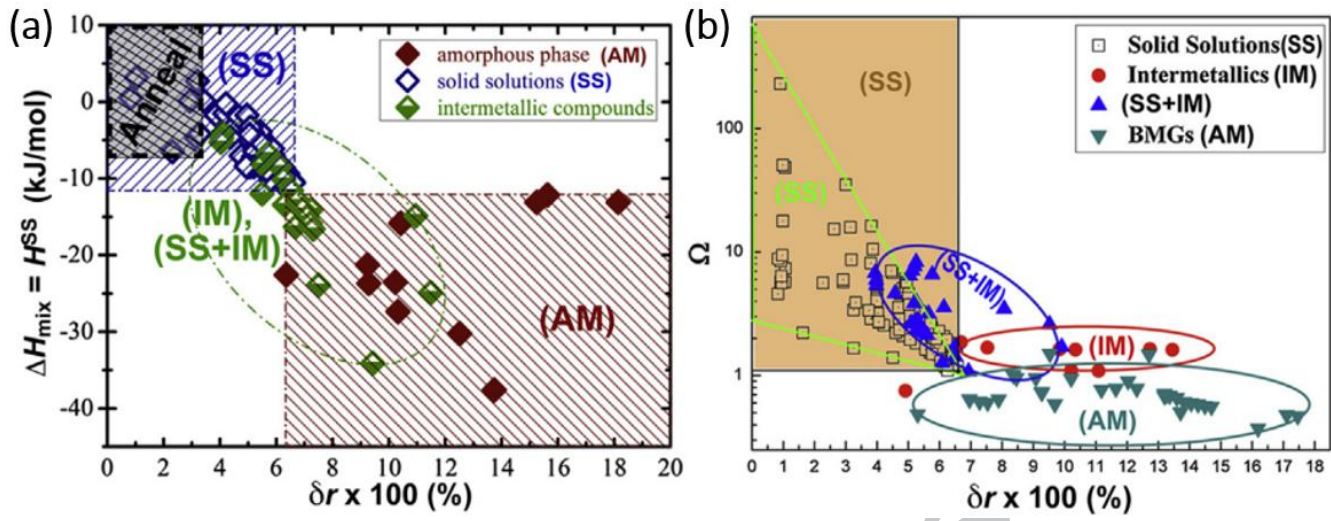


Fig. 11. Empirical indicators to separate solid solution (SS), intermetallic (IM) and amorphous phase (AM) regions using (a) δr and H^{SS} ; (b) δr and C . The annealing data are used to compare with the as-cast data in (a) [43, 45].

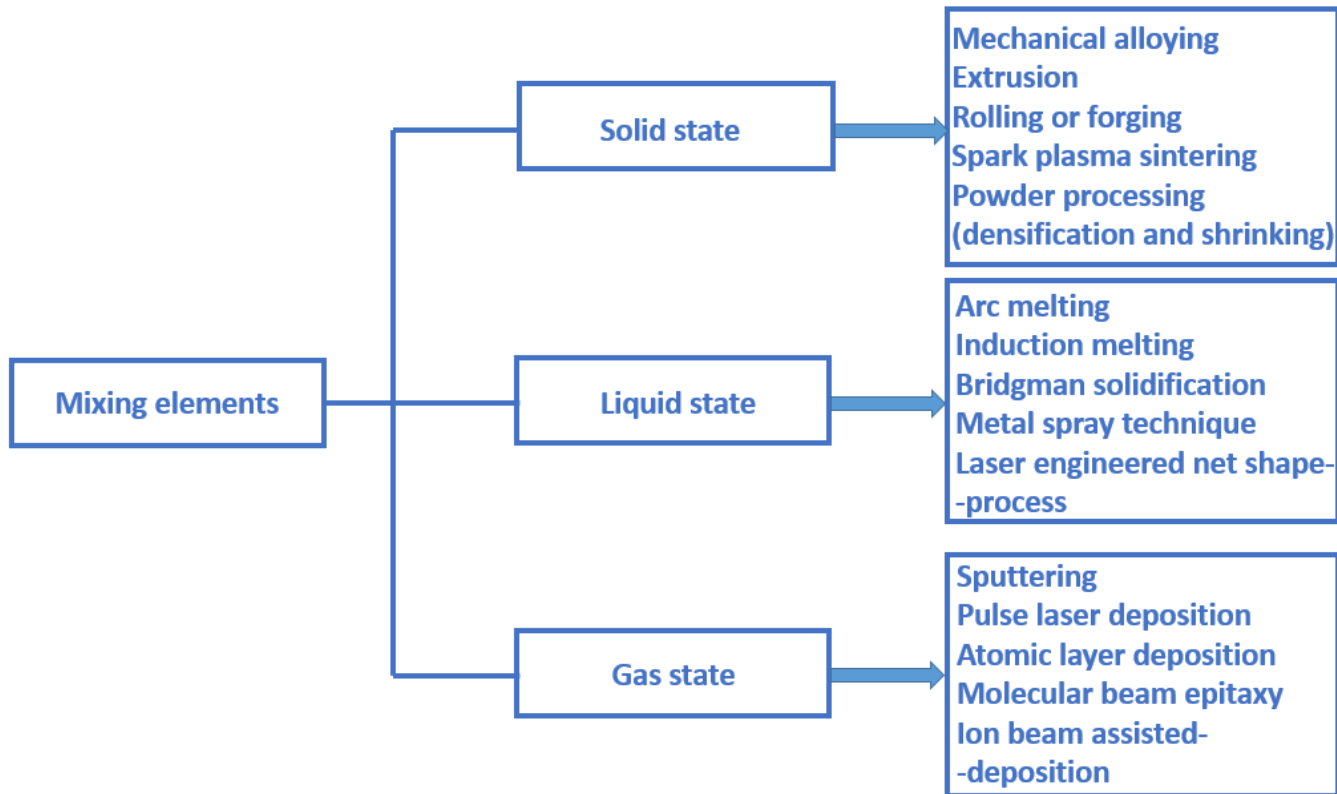


Fig. 12. Synthesis methods of HEAs starting from different states.

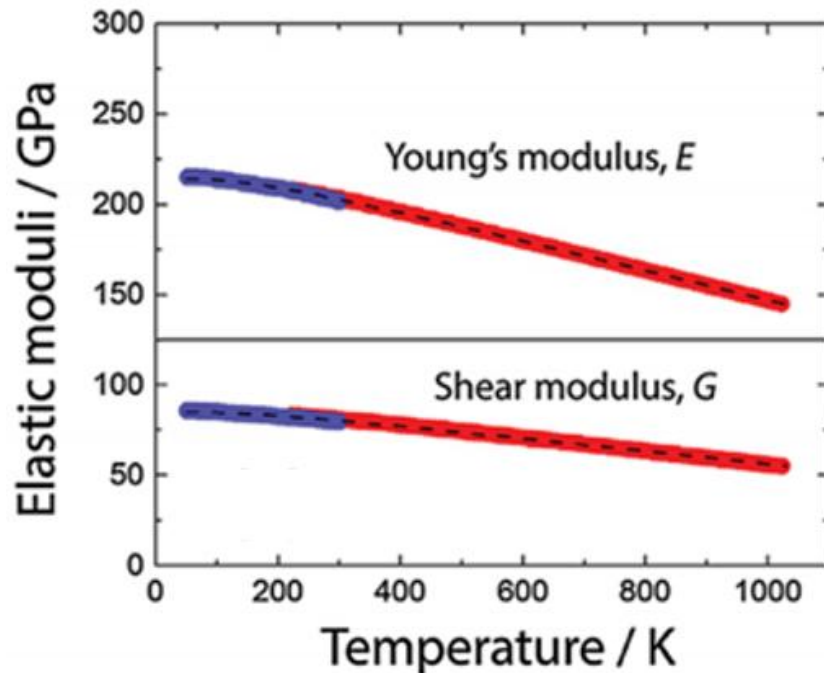


Fig. 13. The dependence of the shear modulus G and Young's modulus E on the temperature for the Cantor alloy. Both G and E decrease monotonically as a function of temperature [54-56].

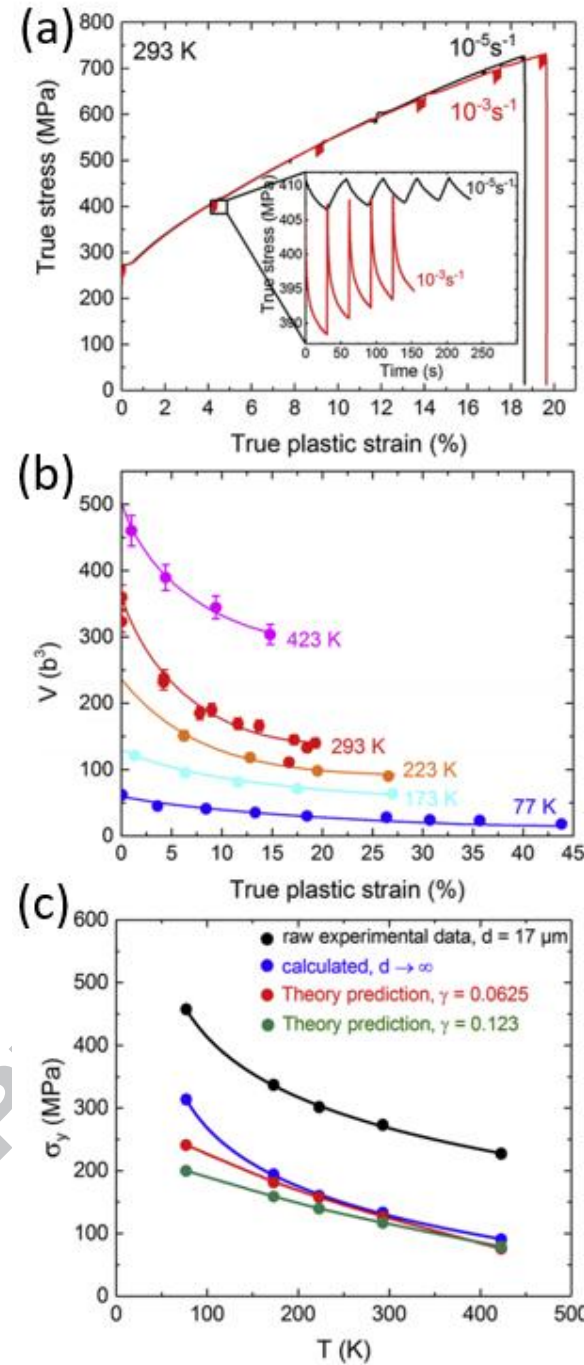


Fig. 14. Determination of the activation volume for plastic deformation of the CrMnFeCoNi Cantor alloy: (a) Successive stress relaxation cycles at room temperature for specimens loaded at two strain rates (10^{-3} and 10^{-5} s^{-1}), (b) stress relaxation as a function of plastic strain for different temperatures, and (c) predicted and measured flow stress at a function of temperature; two values of the dislocation line parameter, 0.123 and 0.0625, are used. Experimental results for a grain size of $d = 17 \mu\text{m}$ translated to single crystal by use of Hall-Petch equation [63].

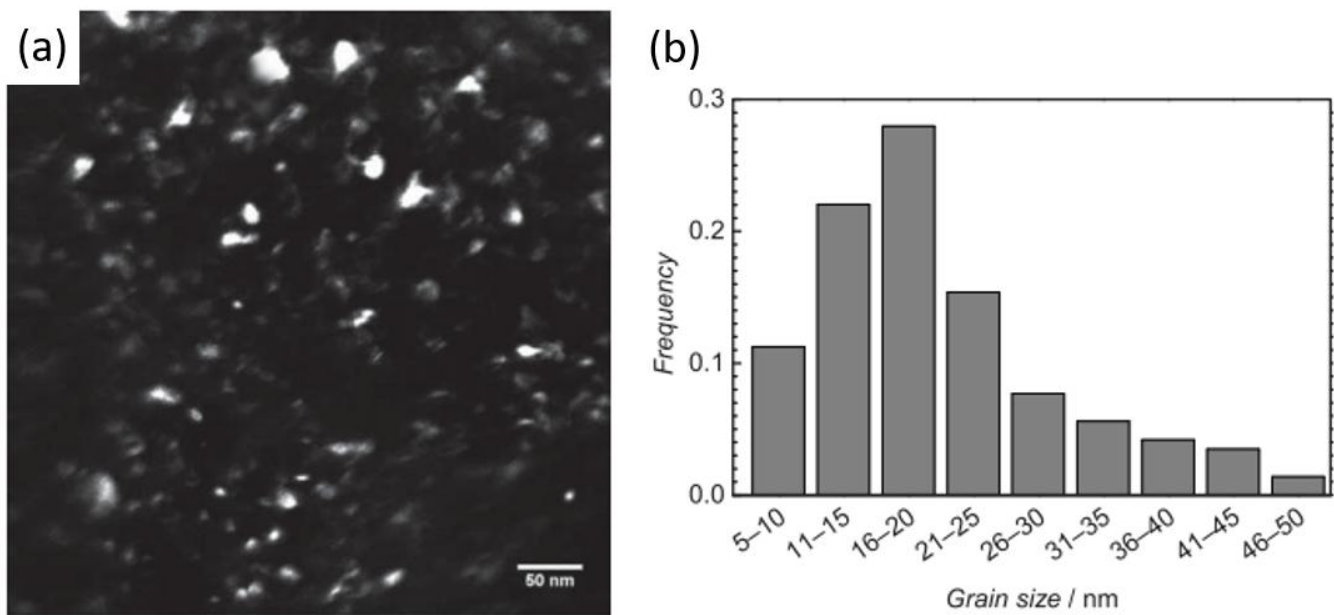


Fig. 15. (a) Dark-field TEM image, and (b) grain-size distribution of the nanocrystalline $\text{Li}_{20}\text{Mg}_{10}\text{Al}_{20}\text{Sc}_{20}\text{Ti}_{30}$ alloy fabricated by mechanical alloying [74].

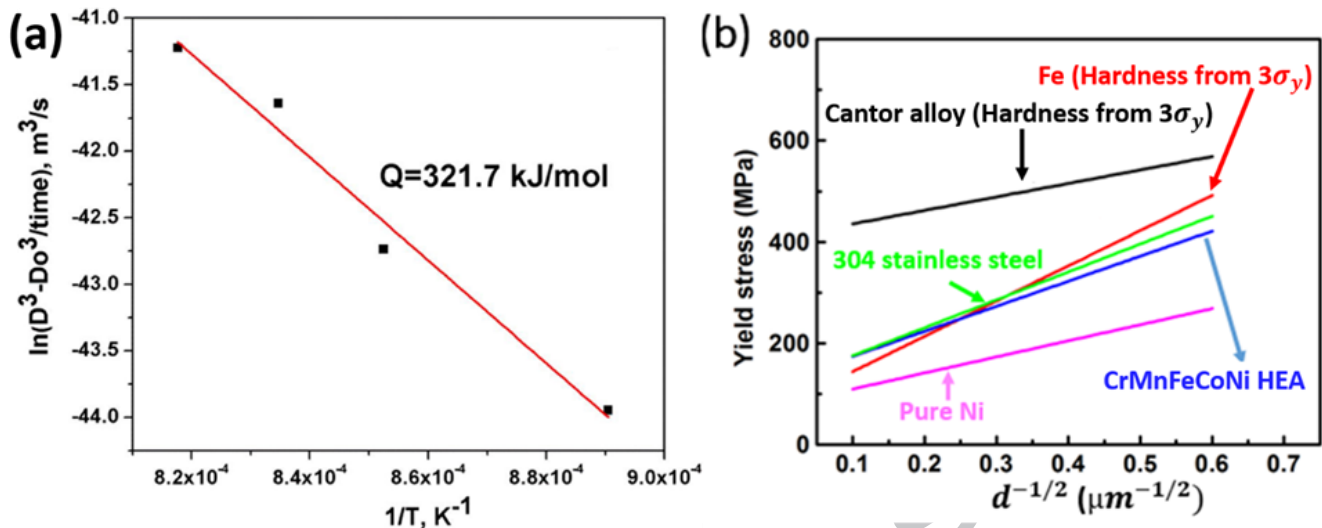


Fig. 16. (a) Linear fit of logarithmic grain growth rate with respect to $1/T$, the slope of which infers the activation energy for grain growth [75]. (b) Hall-Petch relationship for pure Ni [198], pure Fe [82], 304 stainless steel [78] and the CrMnFeCoNi HEA [75, 79]. (The microhardness has been converted to equivalent yield stress using the relationship $H_V = 3\sigma_y$.)

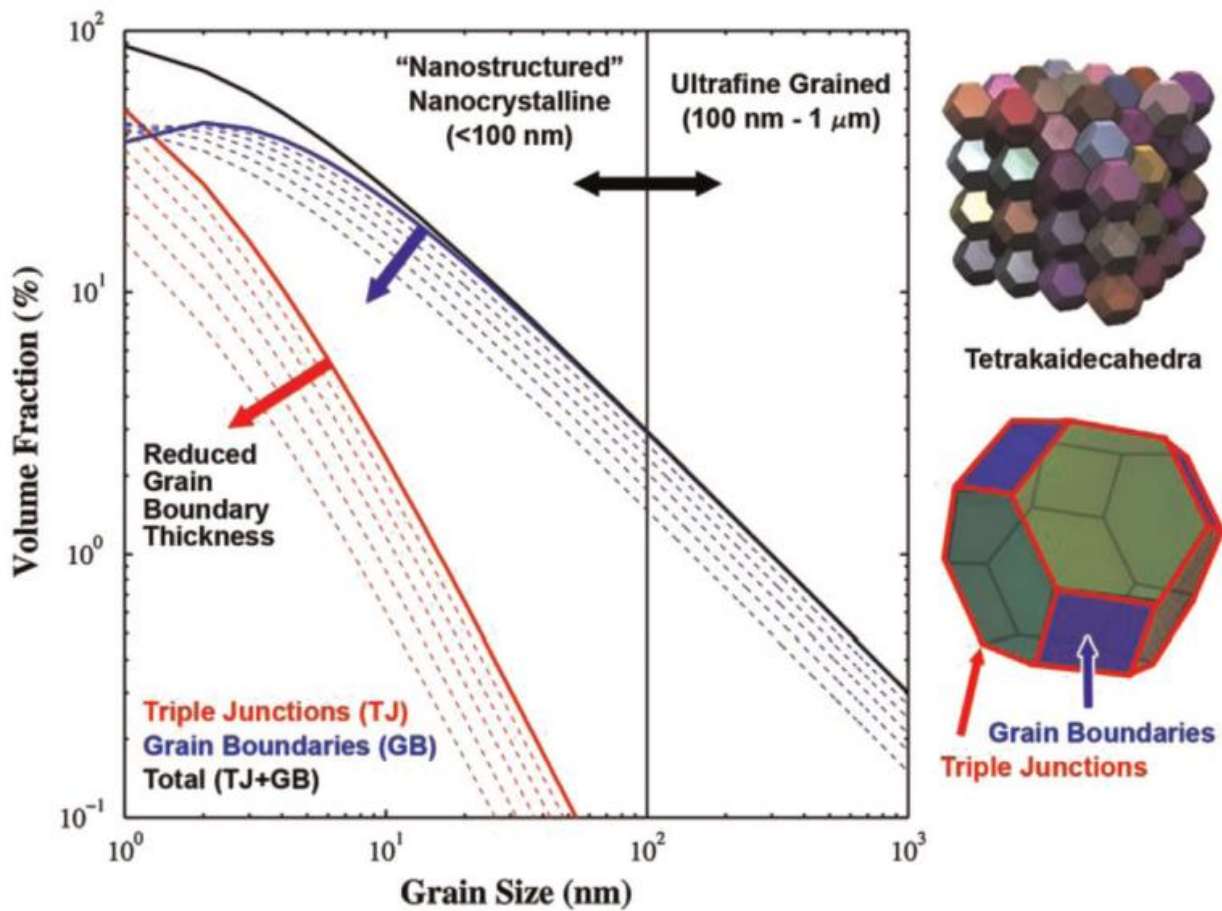


Fig. 17. (a) Variation of volume fraction of inter-crystal regions (grain-boundaries and triple-junctions) with the grain-size from the ultrafine-grained (100 nm to 1 μm) to the nanocrystalline (<100 nm) [81].

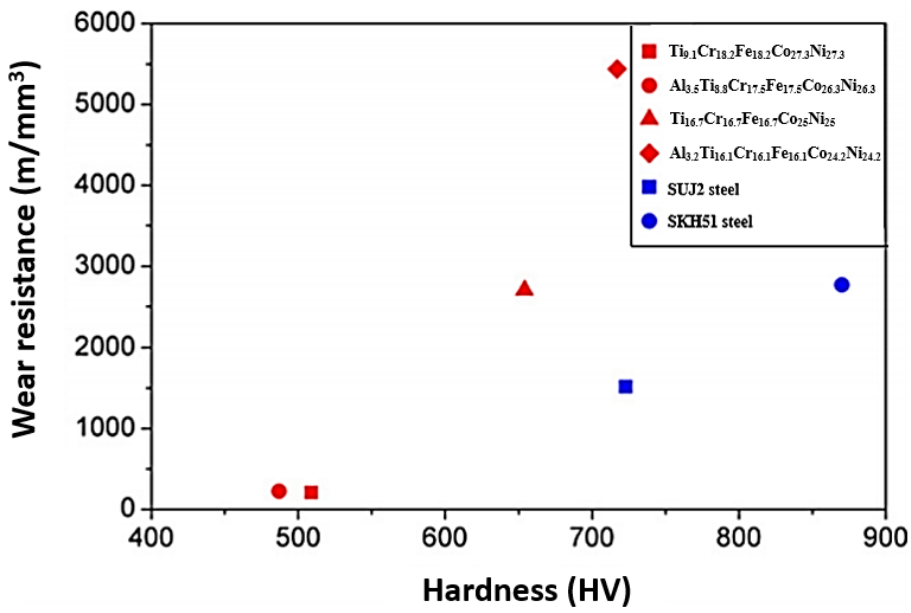


Fig. 18. Wear resistance behavior as a function of hardness of $\text{Ti}_{9.1}\text{Cr}_{18.2}\text{Fe}_{18.2}\text{Co}_{27.3}\text{Ni}_{27.3}$, $\text{Al}_{3.5}\text{Ti}_{8.8}\text{Cr}_{17.5}\text{Fe}_{17.5}\text{Co}_{26.3}\text{Ni}_{26.3}$, $\text{Ti}_{16.7}\text{Cr}_{16.7}\text{Fe}_{16.7}\text{Co}_{25}\text{Ni}_{25}$, and $\text{Al}_{3.2}\text{Ti}_{16.1}\text{Cr}_{16.1}\text{Fe}_{16.1}\text{Co}_{24.2}\text{Ni}_{24.2}$, as compared to reference materials of bearing steel and SKH51 high-speed tool steel [89].

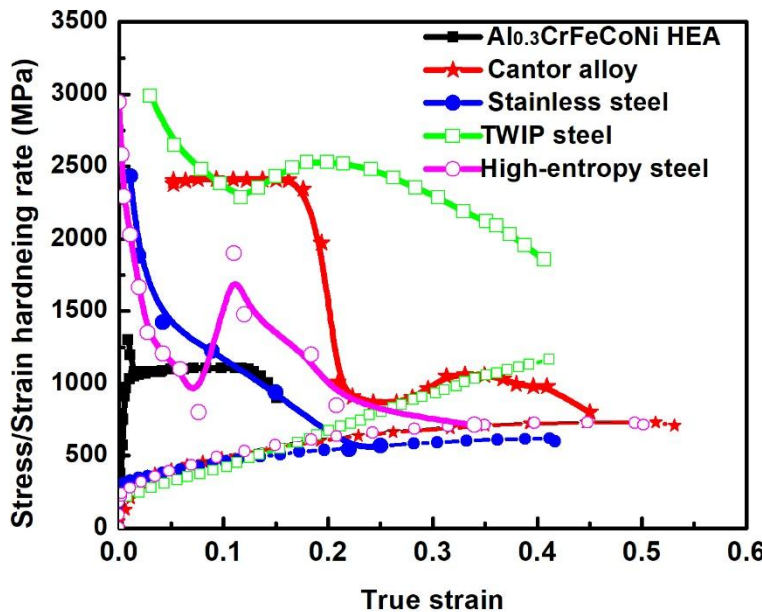


Fig. 19. Comparison of strain-hardening rates as a function of true strain for different alloys: TWIP steel ($\text{C}_{0.6}\text{Al}_{1.5}\text{Si}_{0.22}\text{FeMn}_{18}$) [95], $\text{Al}_{0.3}\text{CrFeCoNi}$ HEA [19,96], 304 stainless steel [94], $\text{Cr}_{10}\text{Mn}_{30}\text{Fe}_{50}\text{Co}_{10}$ high-entropy steel [97], and the CrMnFeCoNi Cantor alloy [15] corresponding stress *vs.* strain are also shown with the same symbols.

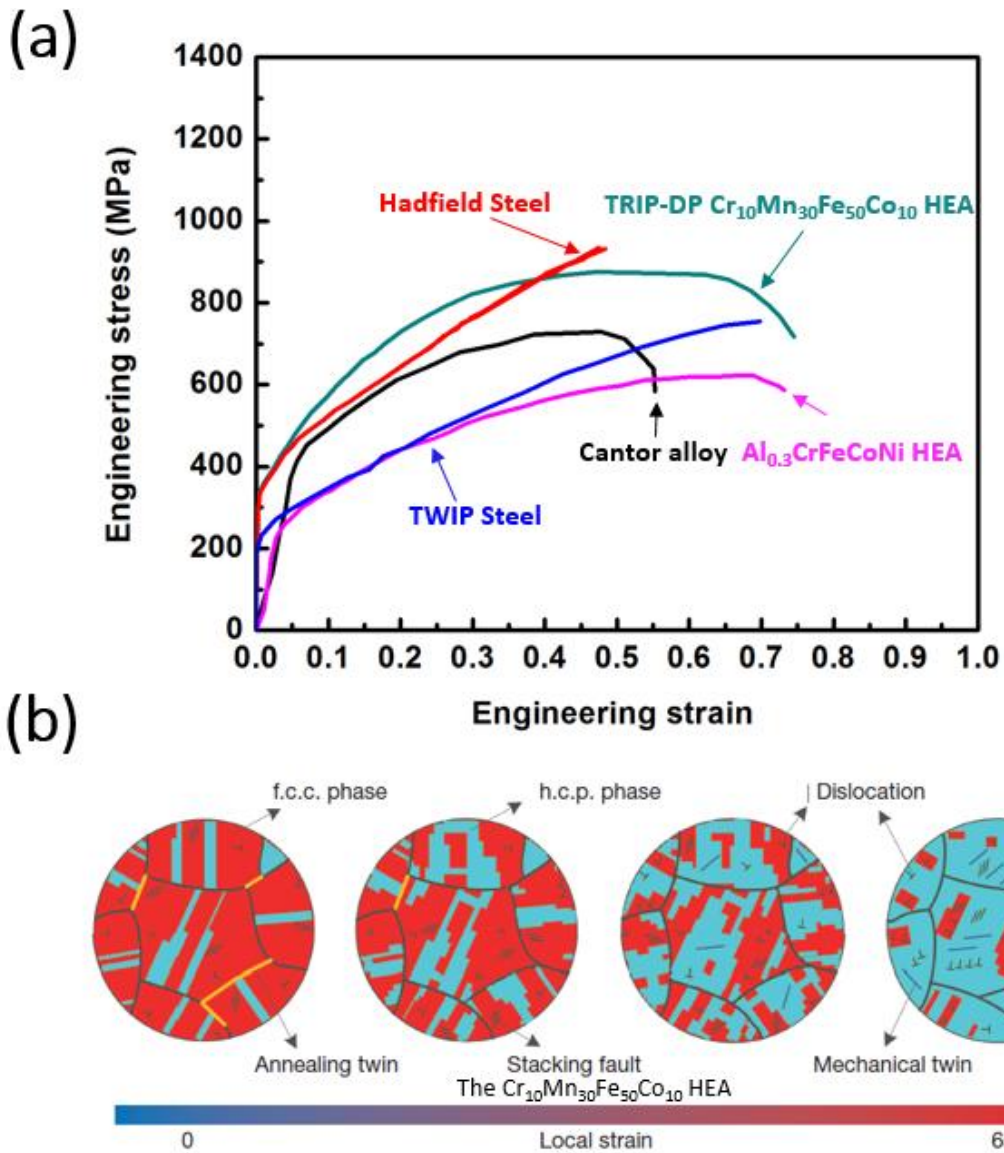


Fig. 20. (a) Comparison of tensile stress *vs.* strain behavior for different alloys: the Cr₁₀Mn₃₀Fe₅₀Co₁₀ TRIP-DP high-entropy steel [97], the CrMnFeCoNi Cantor alloy [15], Hadfield steel [90], TWIP steel [95] and the Al_{0.3}CrFeCoNi HEA [112]; (b) Schematic drawing describing the typical deformation mechanisms of these materials, using the TRIP-DP high-entropy steel as an example [97].

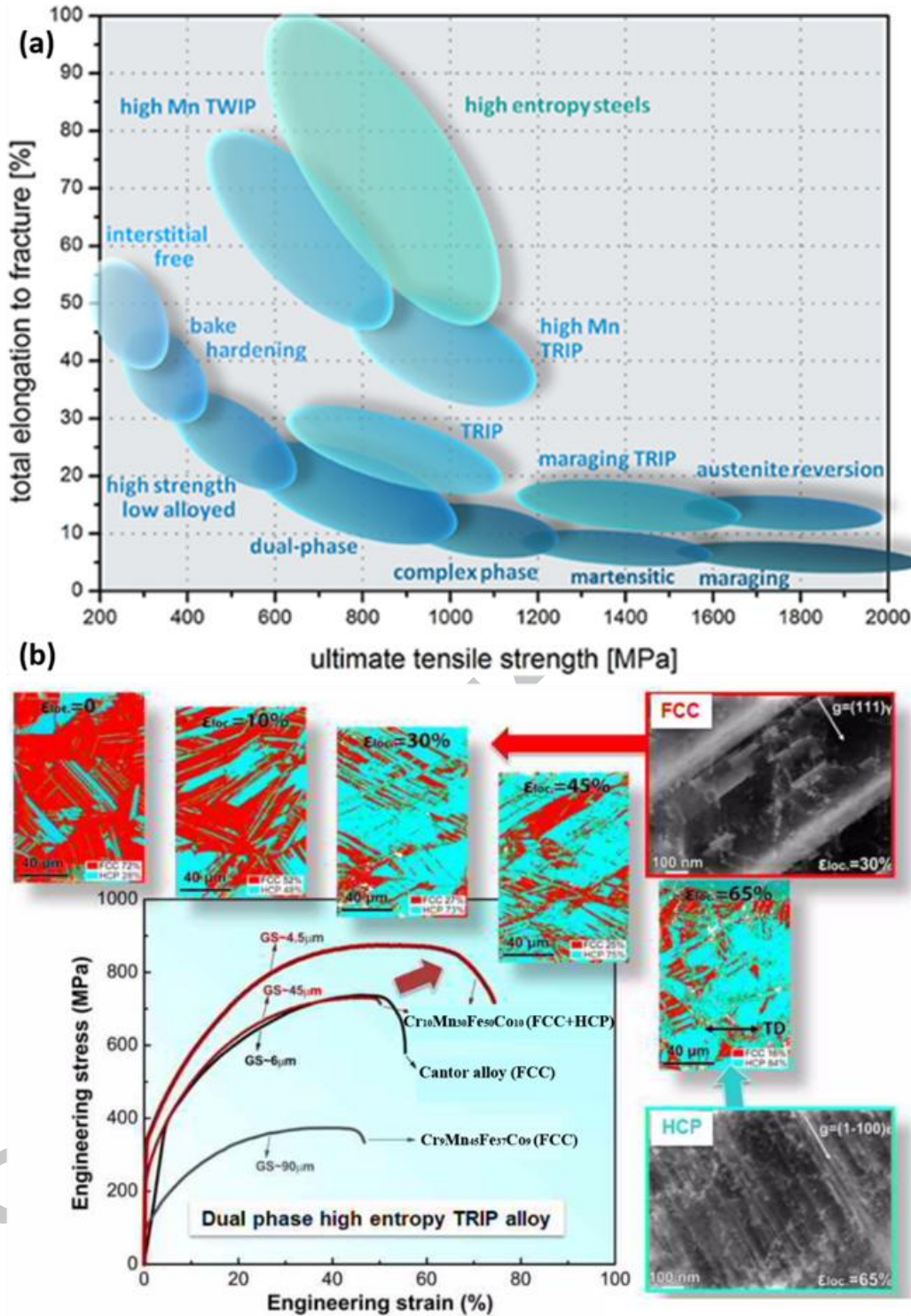


Fig. 21. (a) Ultimate strength *vs.* ductility (“banana”) plot for steels showing high-entropy (HE) steel with superior performance [98]. (b) Tensile stress-strain response for different high-entropy alloys showing superior performance of the TRIP HEA; peripheral micrographs show how the transformation from *fcc* (red) to *hcp* (blue) is associated with the strong work hardening [108].

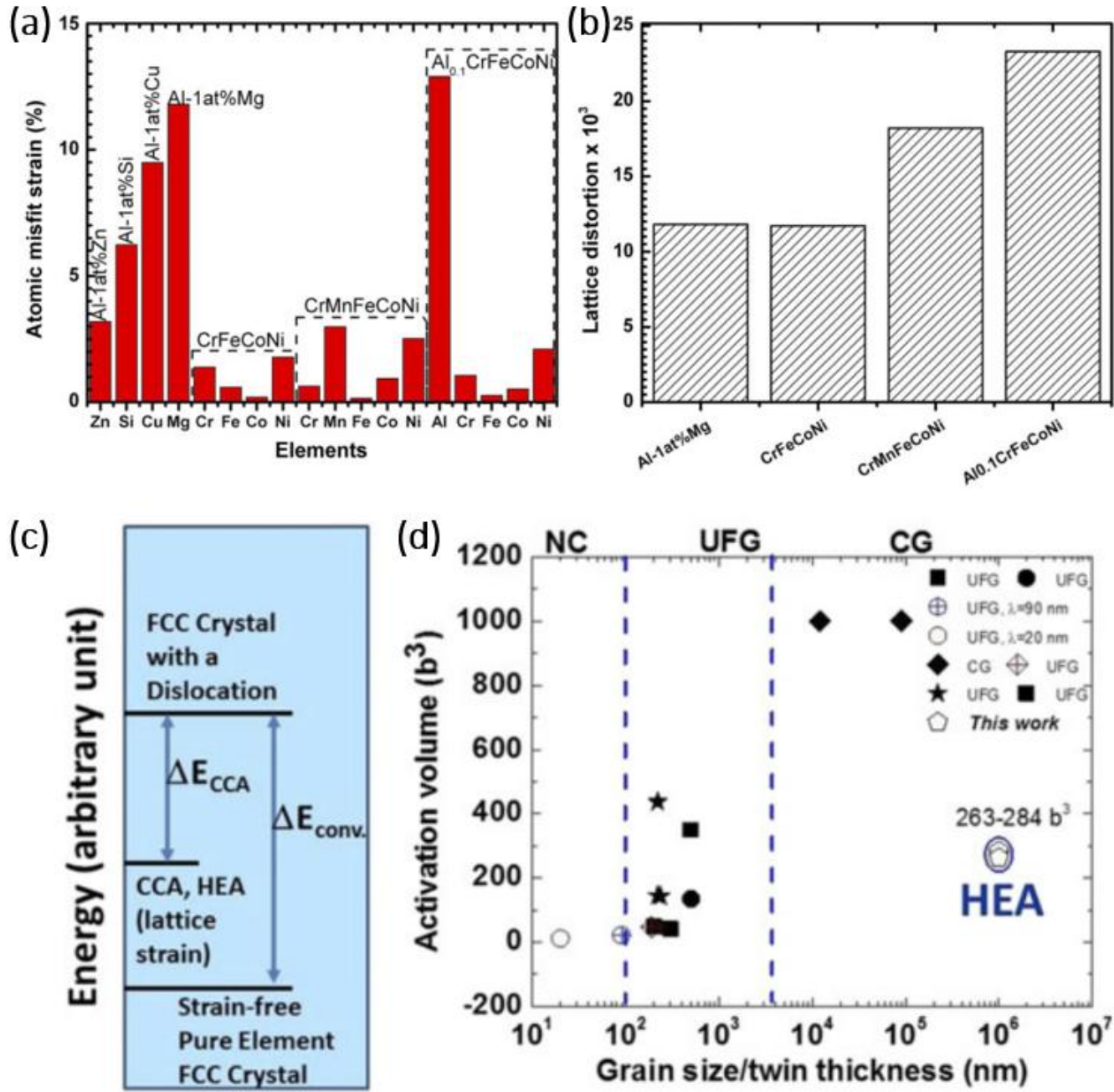


Fig. 22. Lattice mismatch effect in HEAs: (a) Lattice misfit strain of single phase *fcc* binary alloys and HEAs, and (b) Lattice-distortion effect in Al-(1 at. %)Mg alloy, CrFeCoNi HEA, CrMnFeCoNi HEA and Al_{0.1}Cr_{0.1}Fe_{0.1}Co_{0.1}Ni_{0.1} HEA. (c) Schematic drawing showing energy difference for dislocation nucleation in pure element and HEAs, with the influence of lattice strain. E_{conv} is activation energy for dislocation nucleation in conventional alloy, while ΔE_{CCA} is activation energy for dislocation nucleation in HEAs. (d) Anomalous behavior of the coarse-grained Al_{0.1}CoCrFeNi HEA with much lower activation volumes, compared to conventional alloys [29].

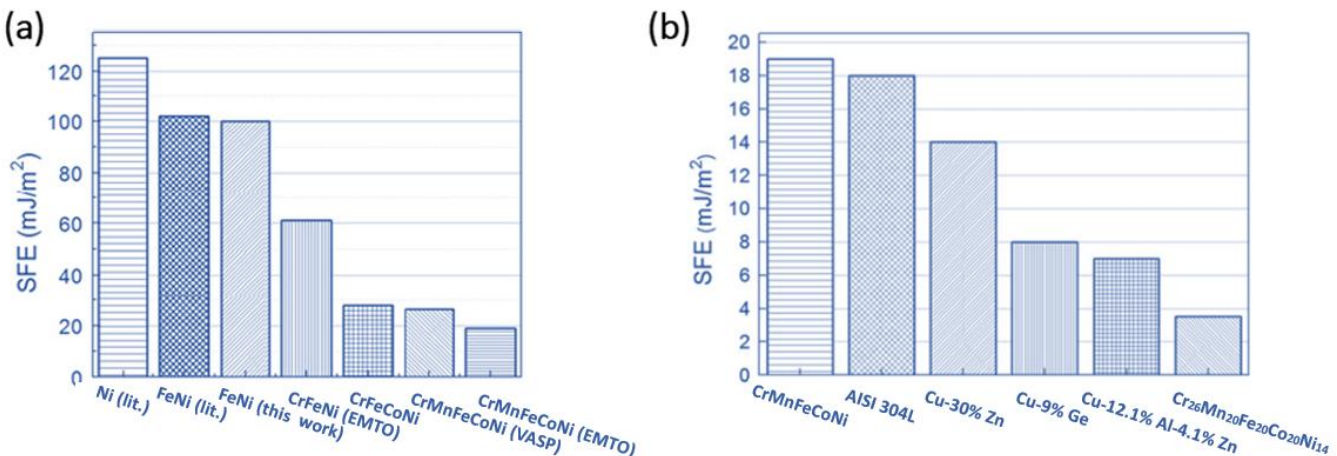


Fig. 23. (a) Stacking-fault energy (SFE) of equimolar *fcc* metals from pure Ni to CrMnFeCoNi HEA. (b) SFEs of equiatomic CrMnFeCoNi and $\text{Cr}_{26}\text{Mn}_{20}\text{Fe}_{20}\text{Co}_{20}\text{Ni}_{14}$ HEAs, as compared with other low SFE alloys [118].

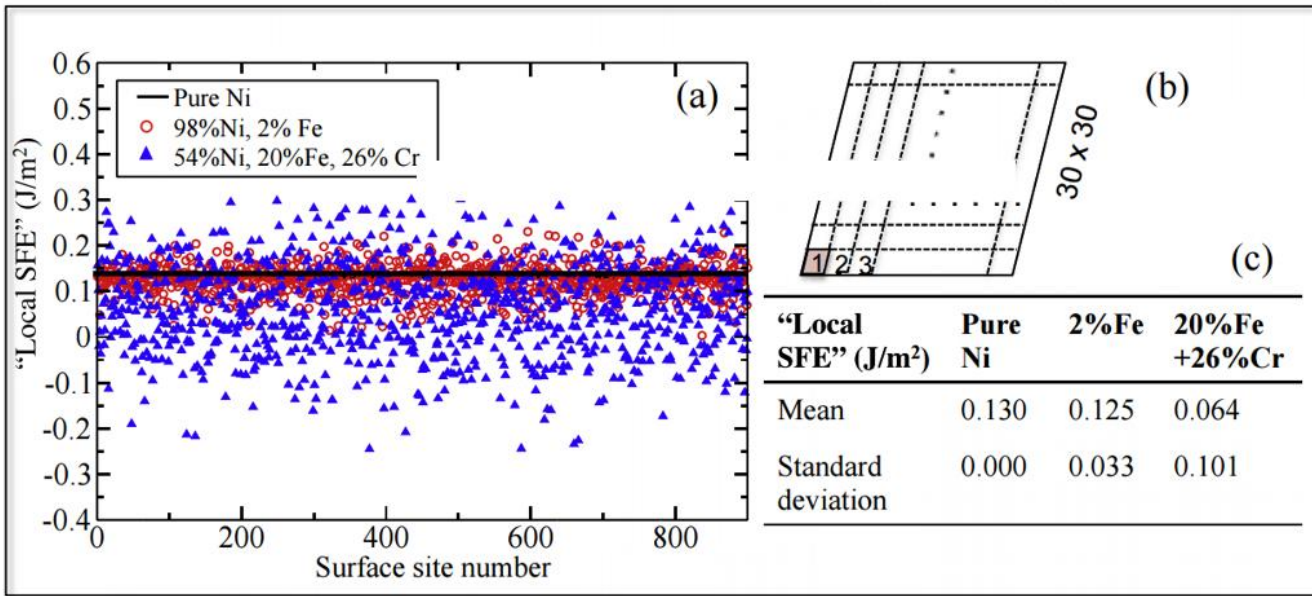


Fig. 24. (a) The values of “local stacking fault energy” of the (26 at.%)Cr-(20 at.%)Fe-Ni alloy, in comparison with pure Ni and the Ni-(2 at.%)Fe alloy calculated at the 900 surface unit cells. (b) The areas of the $30 \times 30 \times 30$ supercell used in the calculations (a). Each unit cell is represented by the red color. (c) The average and standard deviation of the “local SFE”. Addition of solute atoms significantly reduce the stacking fault energy of the system [122]: it is reduced from 130 mJ.m^{-2} (for Ni) to 64 mJ.m^{-2} (for 26%Cr-20%Fe-Ni).

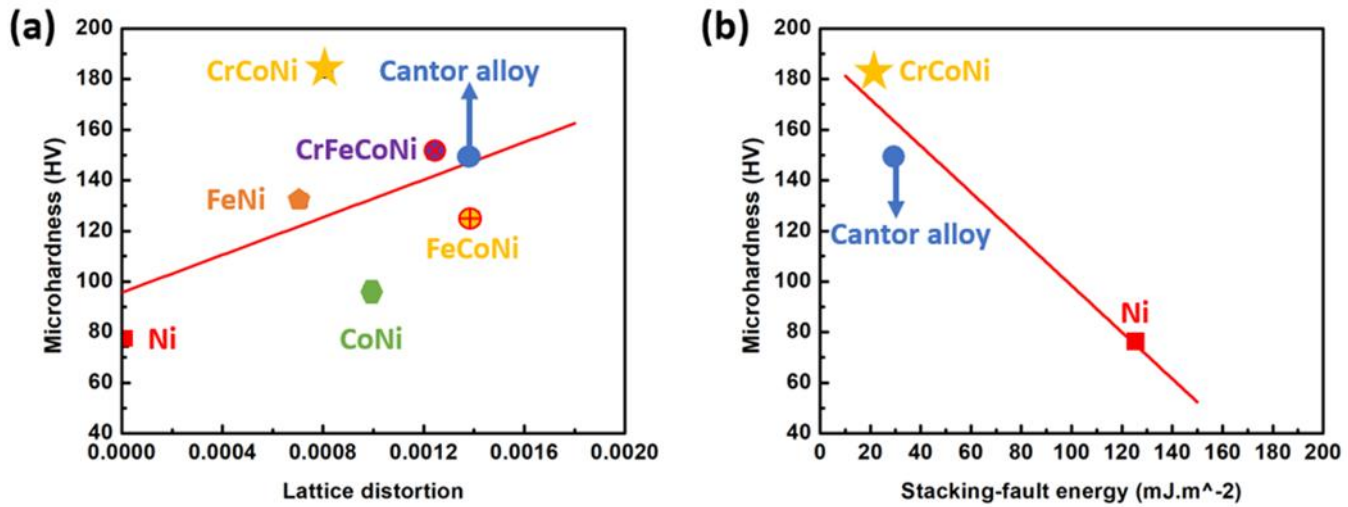


Fig. 25. (a) The relationship between microhardness vs. lattice distortion for Ni, FeNi, CoNi, FeCoNi, CrCoNi, CrFeCoNi and CrMnFeCoNi metals; (b) The relationship between the microhardness of Ni, CoCrNi and CrMnFeCoNi and corresponding stacking-fault energies [123].

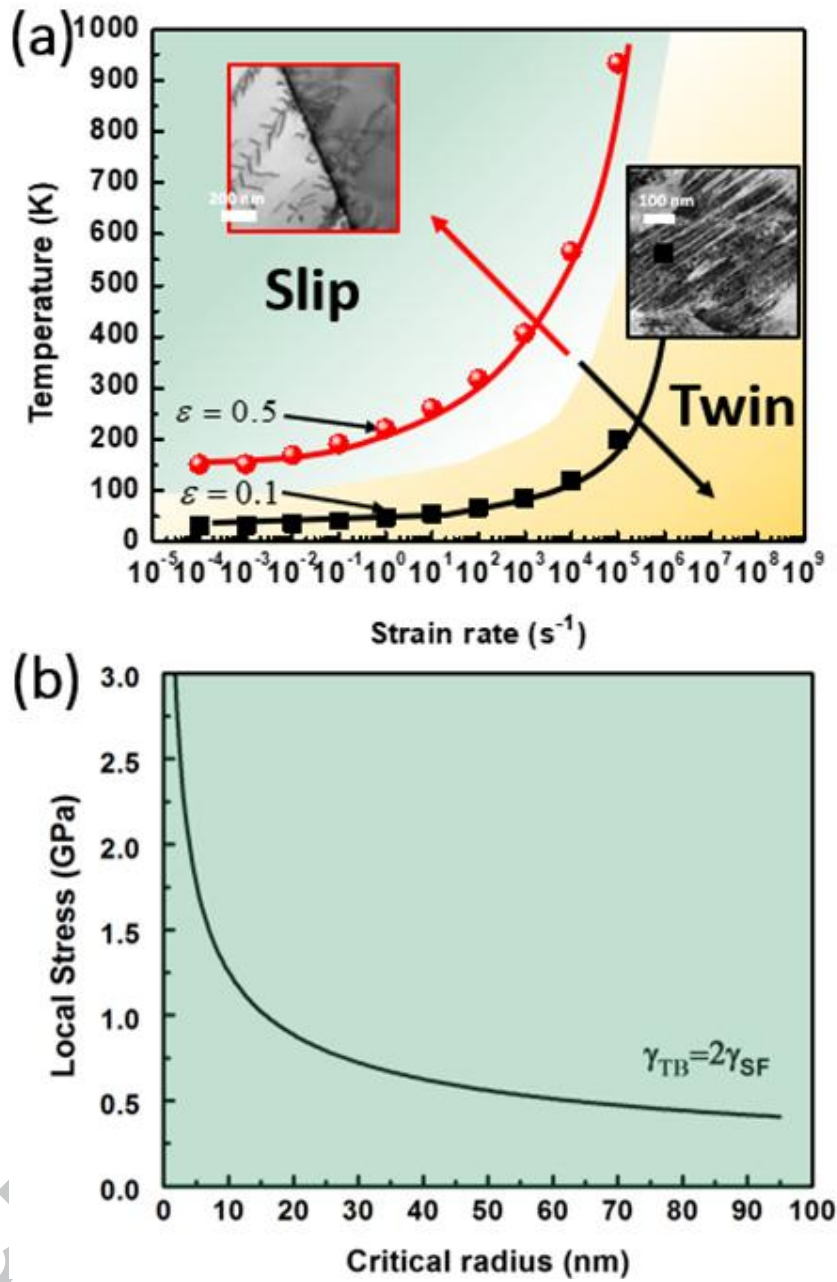


Fig. 26. (a) Slip and twinning regimes transition for polycrystalline CrMnFeCoNi Cantor alloy with grain size $\sim 50 \mu\text{m}$ at two levels of plastic (0.1 (the black line) and 0.5 (the red line) strain. Quasi-static deformation at room temperature generates only slip, whereas shock compression at 10^6 s^{-1} creates twins. (b) Critical radius for twin embryo as a function of local stress for the Cantor alloy [124].

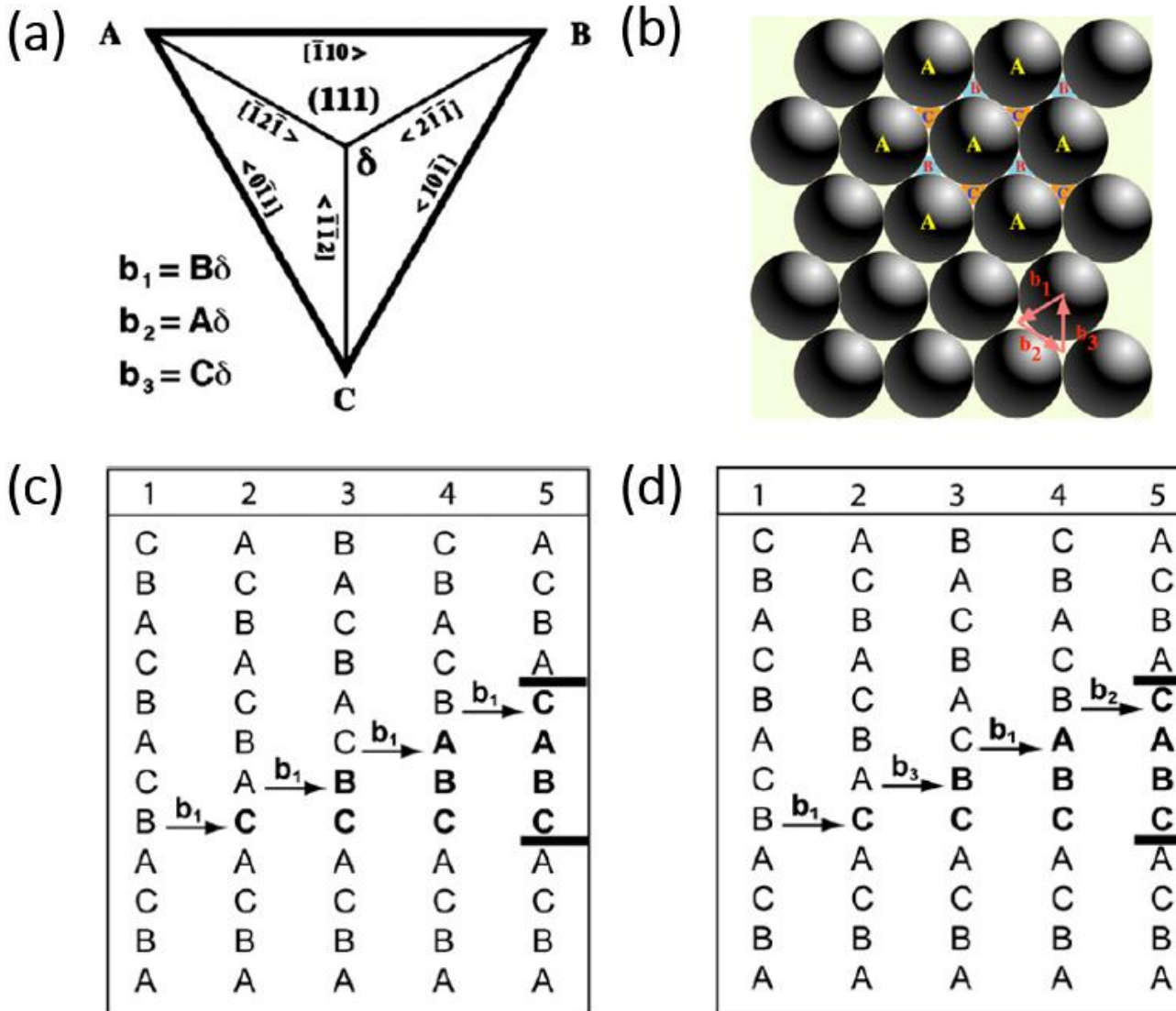


Fig. 27. (a) Thompson tetrahedron showing the Burgers vectors \mathbf{b}_1 , \mathbf{b}_2 , and \mathbf{b}_3 on the fcc $(1\ 1\ 1)$ slip plane of Shockley partial dislocations. (b) Atomic representation showing the partial dislocation Burgers vectors, \mathbf{b}_1 , \mathbf{b}_2 , and \mathbf{b}_3 on the (111) plane. (c) The sequence of forming a four-layer deformation twin by the slip of partial dislocation with the same Burgers vector (\mathbf{b}_1) four times. (d) The sequence of forming a four-layer deformation twin by the slip of four partials with a combination of three Burgers vectors (\mathbf{b}_1 , \mathbf{b}_2 , and \mathbf{b}_3) on (111) slip planes [131].

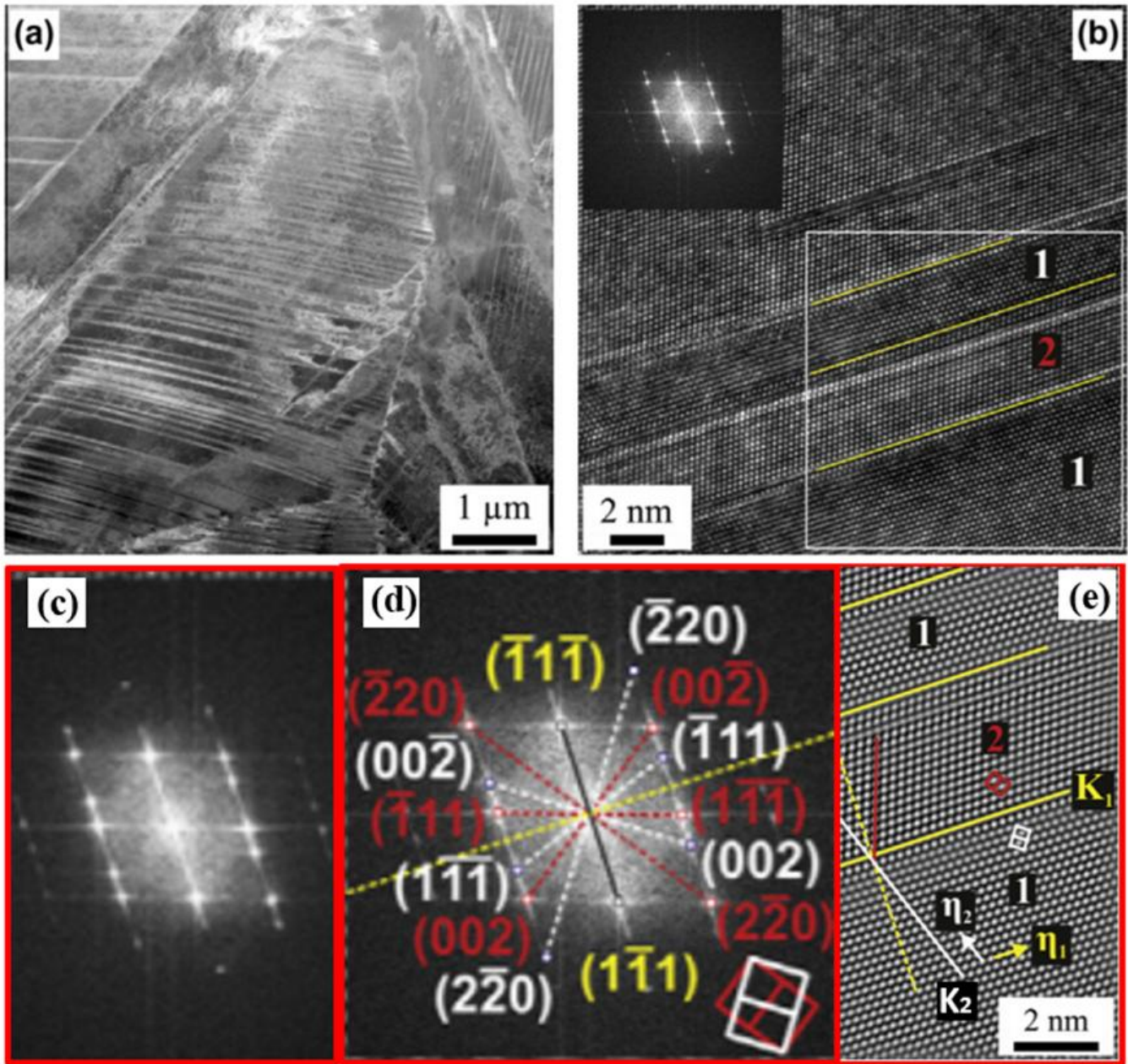


Fig. 28. Deformation microstructure of CrMnFeCoNi Cantor alloy. (a) High angle annular dark-field images of deformation twins in this alloy after a tensile strain ~ 0.2 at 77 K. (b) High-resolution TEM image of twins represented by the “1” and “2” with the corresponding (fast Fourier transform) FFT pattern in (c). (d) Image shows the corresponding diffraction pattern indices in (c). (e) FFT-filtered image illustrating the white square area in (b) shows the corresponding twinning elements [79].

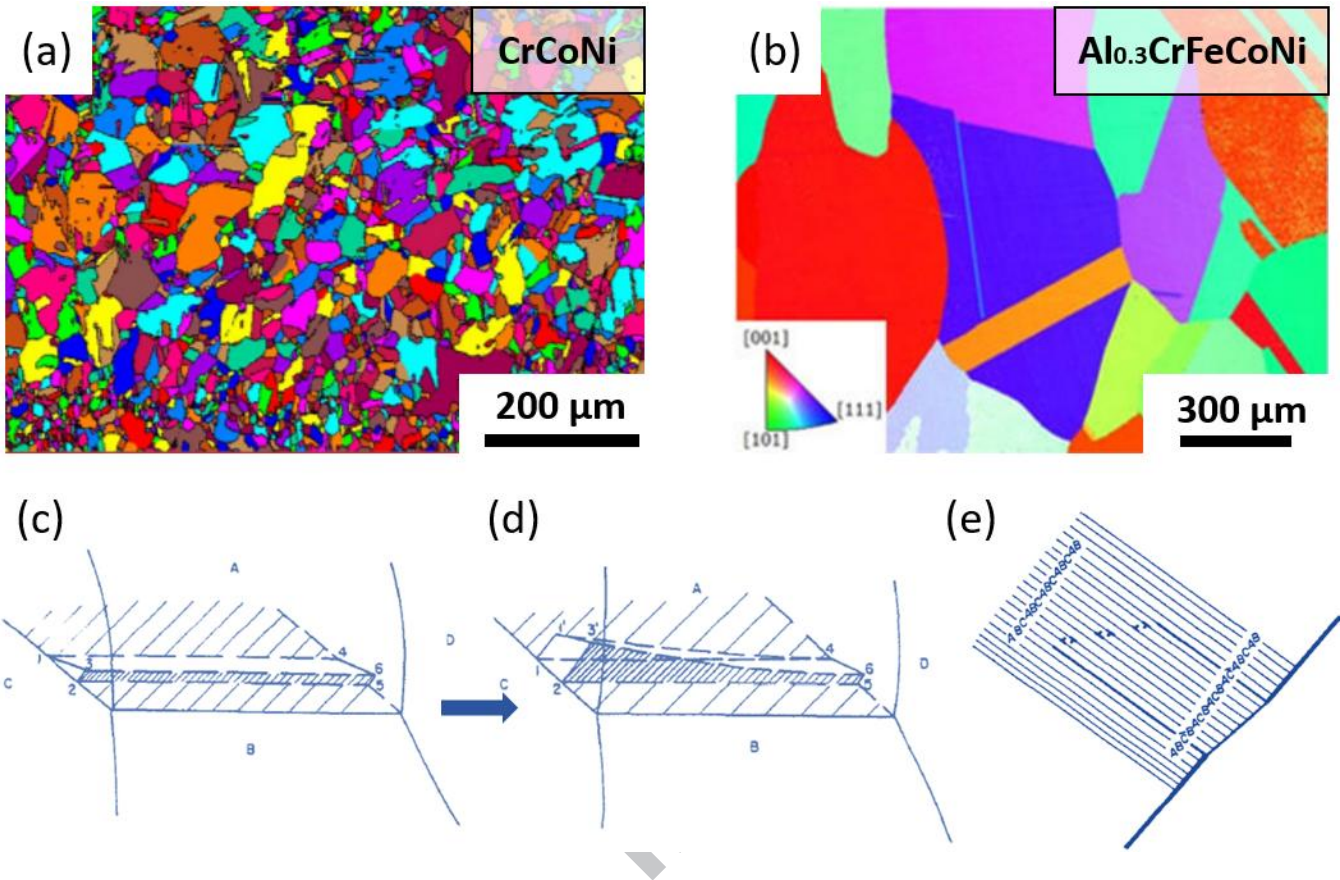


Fig. 29. EBSD-IPF (Electron backscatter diffraction-Inverse pole figure) images showing annealing twins in (a) CrCoNi alloy [145] and (b) Al_{0.3}CrFeCoNi alloy [96]. Schematic drawing showing three-dimensional illustration of nucleation and formation of annealing (or recrystallization) twin ('pop-out' mechanism): (c) small triangular nucleus; (d) growth of annealing twin from one side of the grain boundary; (e) movement of parallel Shockley dislocations with alternative positive and negative Burgers vectors (global $\vec{b} = 0$) on (1 1 1) slip planes leading to growth of annealing twin [134,135]. This pop-out mechanism explains the formation of complete and incomplete parallel-sided twins and single-sided twins.

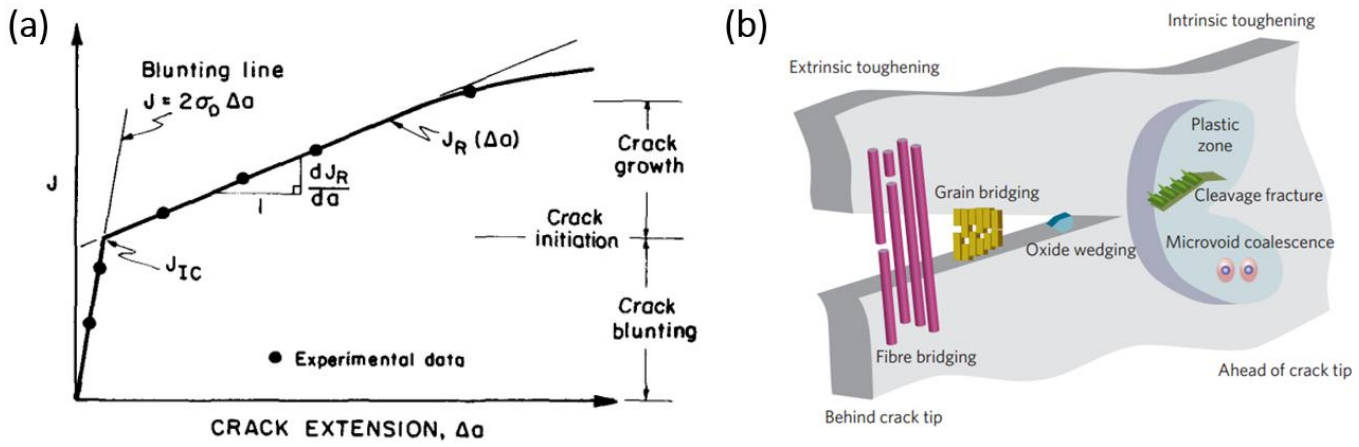


Fig. 30. (a) $J_R(\Delta a)$ crack-resistance curve (R-curve) describing the position of the J_{Ic} at initiation of crack growth where the resistance curve intersects with the blunting line [136]. (b) Schematic drawing describing the intrinsic (plasticity) and extrinsic (shielding) toughening mechanisms in terms of the crack advance [2].

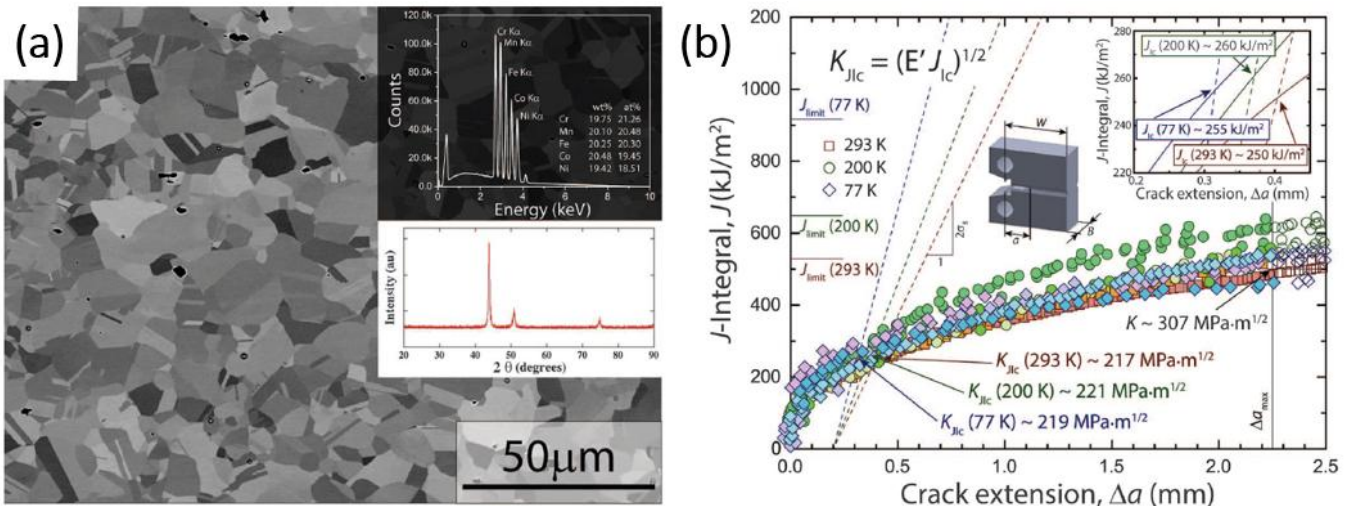


Fig. 31. Microstructure and fracture toughness of the CrMnFeCoNi Cantor HEA. (a) SEM image showing the recrystallized grains with average grain-size $\sim 6\text{ }\mu\text{m}$; the composition is almost equiautomic, and the alloy is a single fcc phase, as shown from x-ray diffraction (XRD) pattern and the energy-dispersive x-ray (EDX) spectroscopy analysis. (b) J -integral and the corresponding fracture toughness K_{Jlc} values of this alloy: $217\text{ MPa}\cdot\text{m}^{1/2}$, $221\text{ MPa}\cdot\text{m}^{1/2}$, and $219\text{ MPa}\cdot\text{m}^{1/2}$ at 293 K , 200 K , and 77 K , respectively [15].

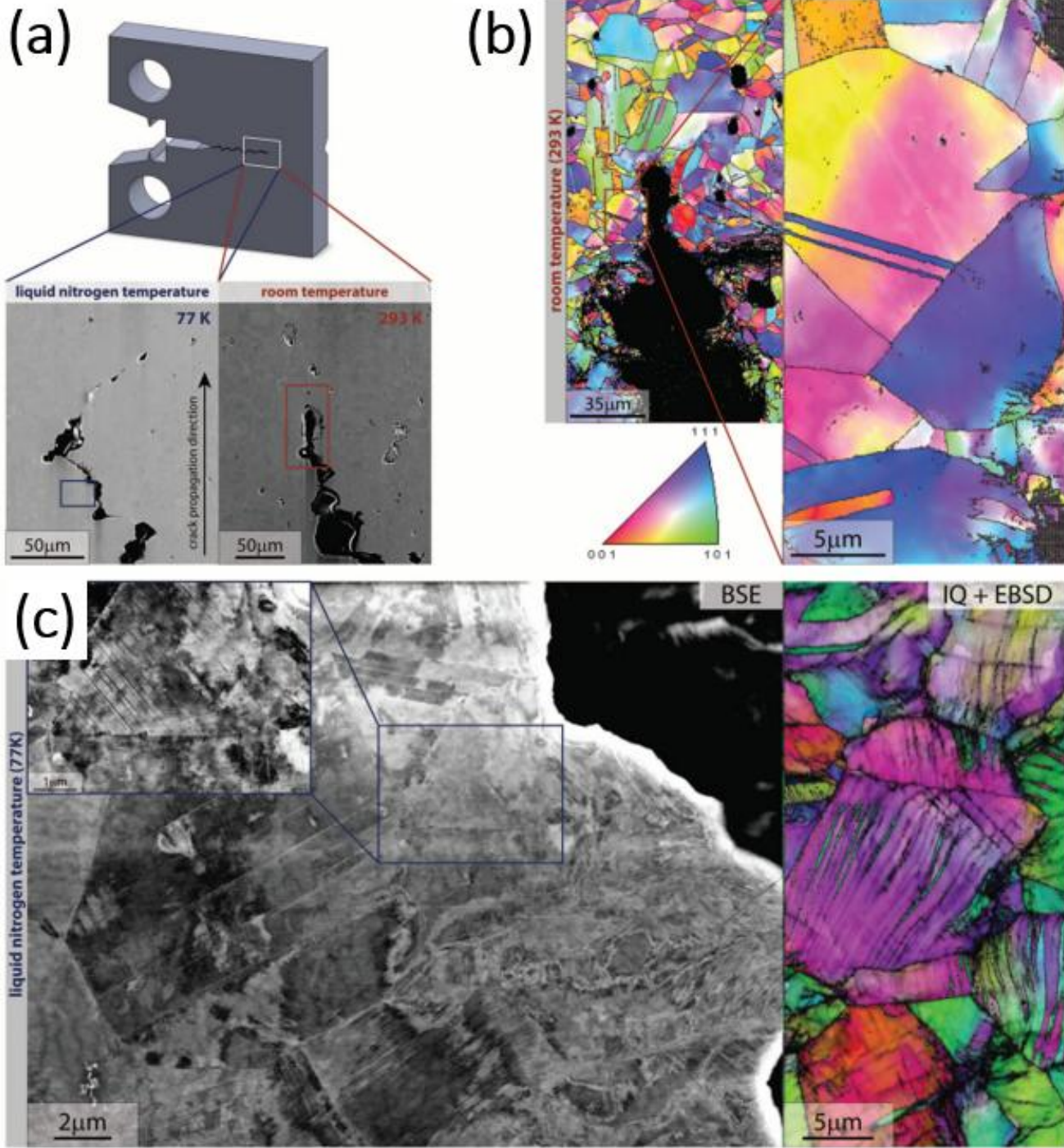


Fig. 32. (a) SEM images of fractured samples tested at 293 K and 77 K indicate ductile fracture of the CrMnFeCoNi HEA by the coalescence of microvoids, with a more distorted crack path at the lower temperature. (b) Electron backscatter diffraction images reveal amounts of annealing twins and significant grain misorientations caused by the dislocation activity at 293 K. (c) Backscattered electron and electron backscatter diffraction images taken at the crack-tip show the formation of deformation twins at nano-scale at 77 K [15].

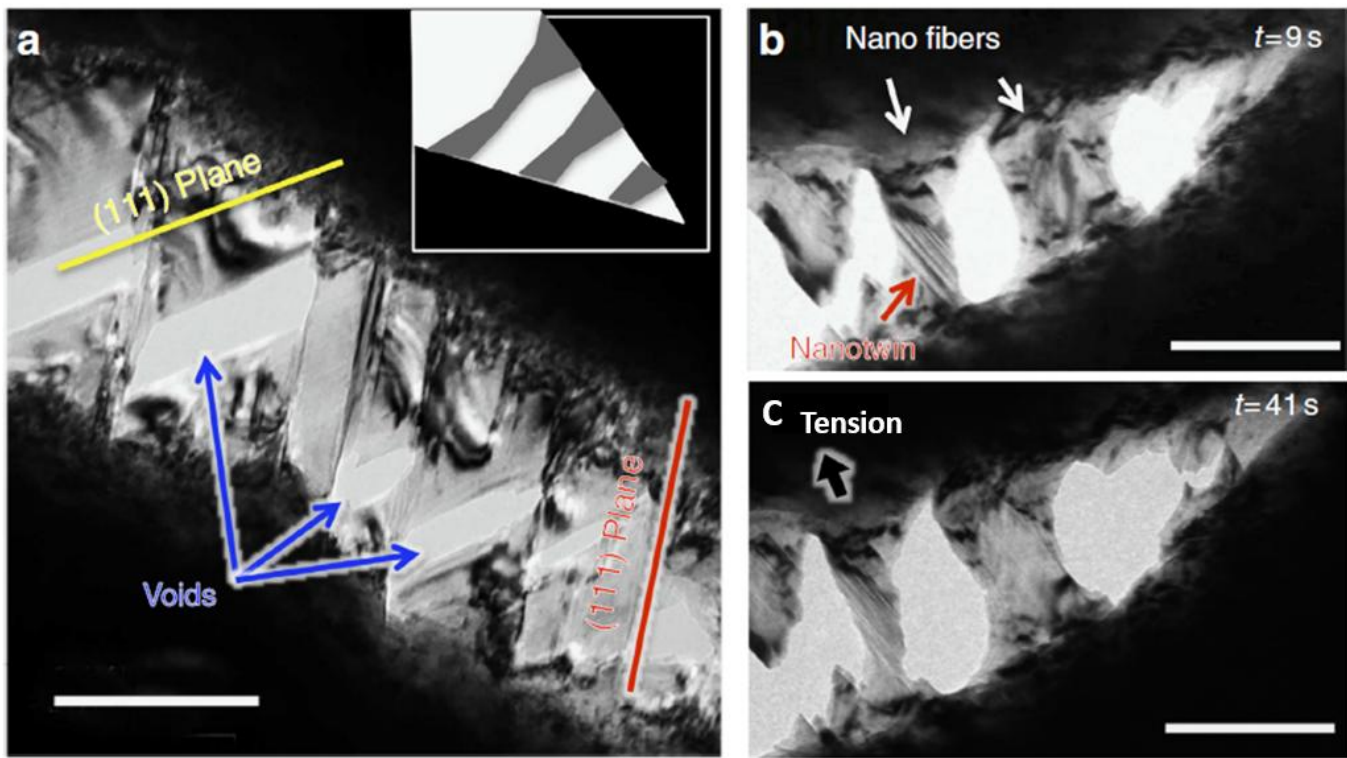


Fig. 33. Bright-field TEM image shows a growing crack during the tension of the CrMnFeCoNi HEA: (a) formation of nano/submicron voids at the intersection of two slip $\{111\}$ planes, which then grow along two slip bands. The crack tip is ~ 500 nm away from the right-lower corner of this image. (b) and (c) two TEM images showing the tensile loading of nano-scale ‘fibers’ bridging the crack (all the scale bars are 200 nm) [144].

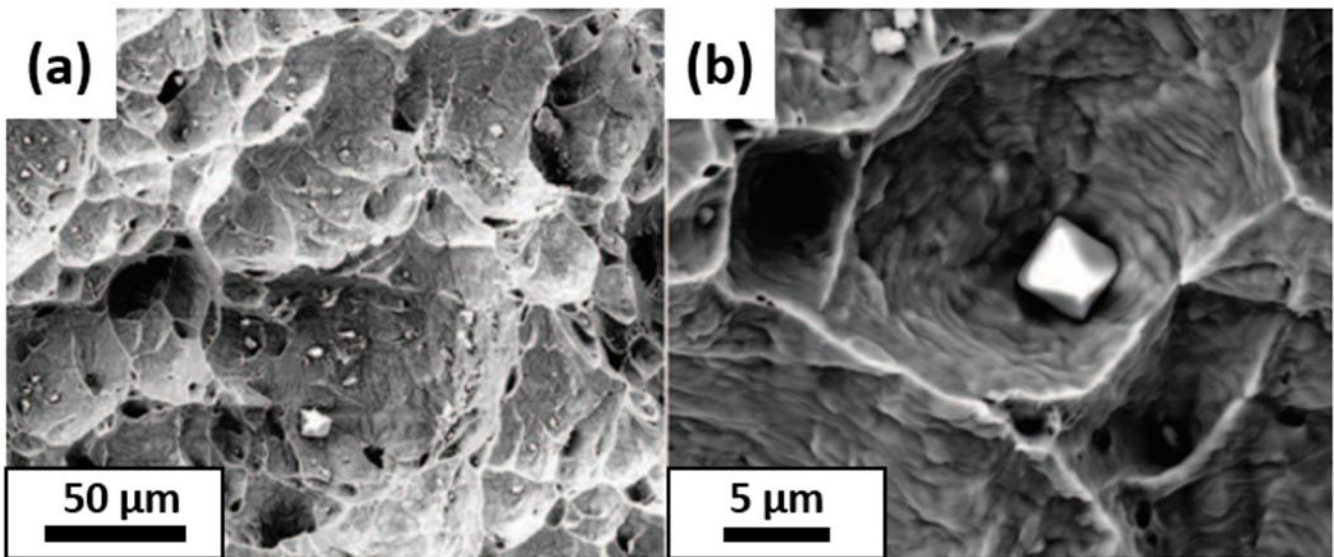


Fig. 34. (a) Dimpled fracture of alloy in fracture toughness specimen; void initiation takes place at Mn- and Cr-rich particles; (b) detail of particle that gave rise to a dimple; dimple size ~20 μm [15].

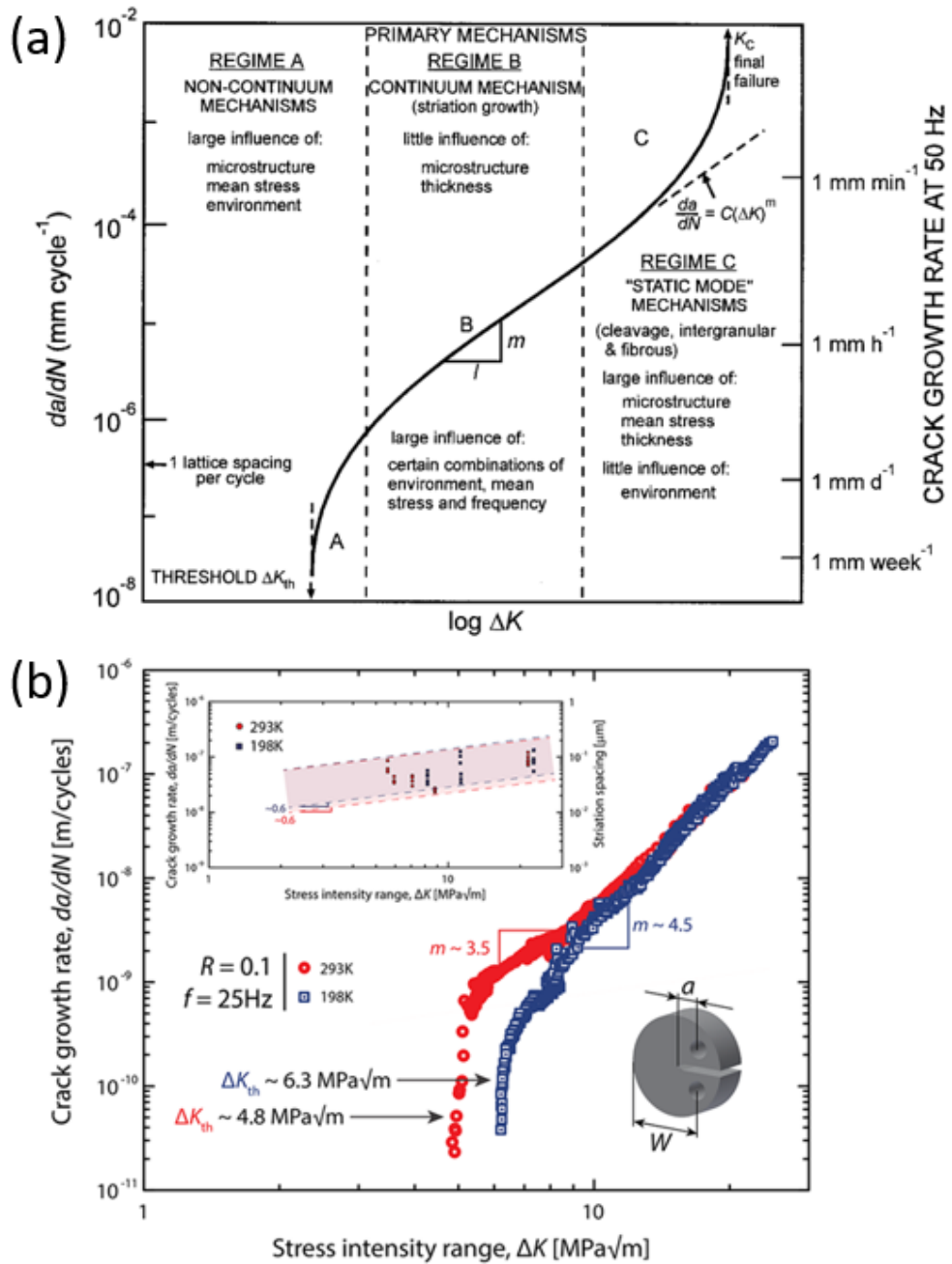


Fig. 35. (a) The changes of the fatigue-crack growth rates da/dN as a function of the applied stress-intensity range ΔK in metals [147]. (b) Fatigue-crack growth behavior of the CrMnFeCoNi alloy, tested at a load ratio R of 0.1 at 293 K and 198 K. A direct comparison of the fatigue-crack growth curves, as a function of the stress-intensity range, ΔK , at both temperatures tested on disc-shaped compact-tension (DC(T)) samples at a frequency of $f = 25$ Hz reveal a clear shift in the fatigue threshold, increasing some 30%, from $\sim 4.8 \text{ MPa} \cdot \text{m}^{1/2}$ to $\sim 6.3 \text{ MPa} \cdot \text{m}^{1/2}$, as the temperature was reduced from ambient to cryogenic conditions. The Paris exponent m was found to change from 3.5 at 293 K to 4.5 at 198 K. The smaller sized, solid symbols in the inset indicate the corresponding variation, as a function of ΔK , in local crack-growth rates, which were estimated from striation spacing measurements on the scanning electron microscopy images of the fracture surfaces [150].

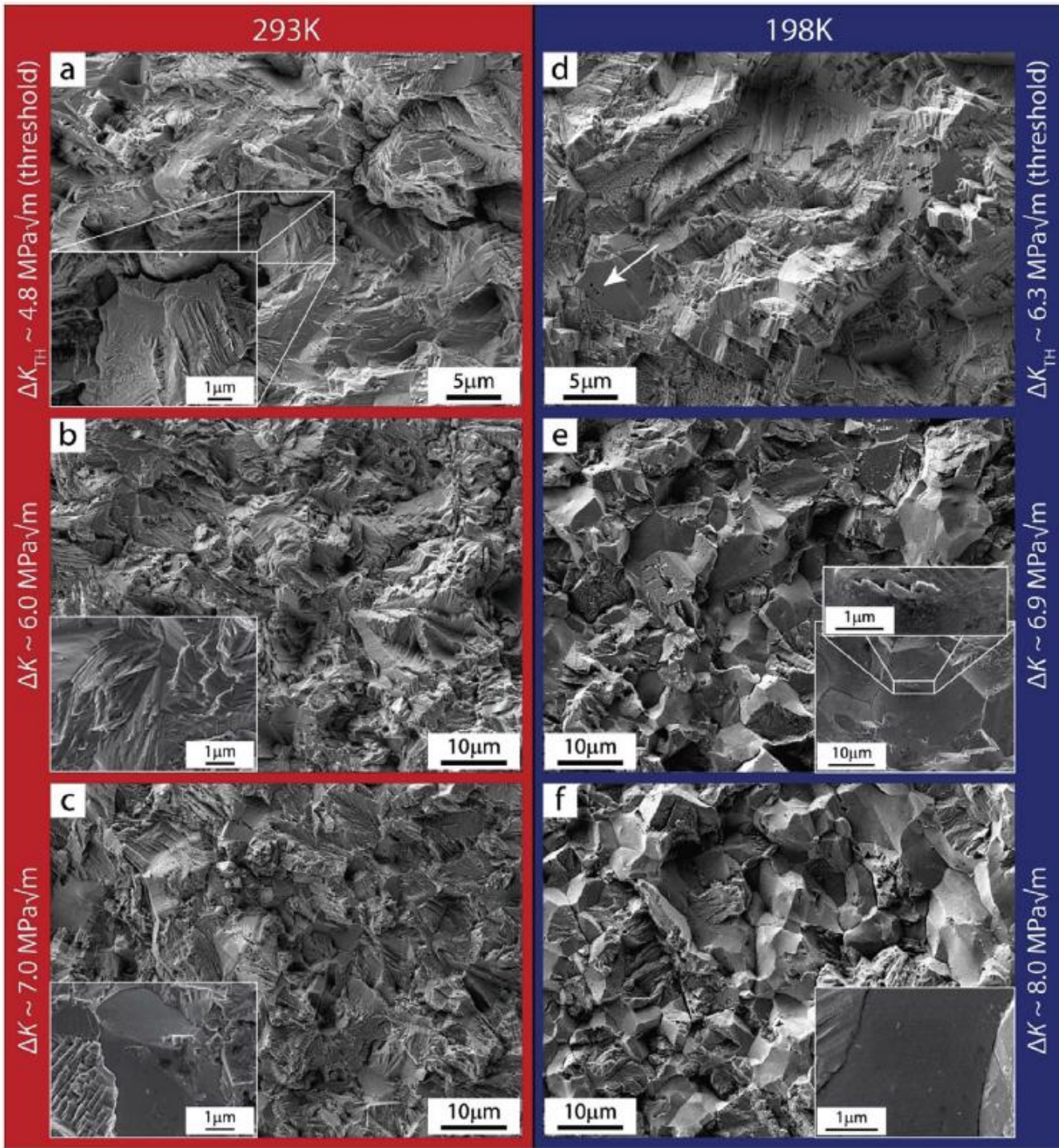


Fig. 36. Fractographic analysis of CrMnFeCoNi specimens tested at 293 K and 198 K. Fracture surface characterization of specimens tested at 293 K show mainly transgranular crack propagation (a–c) with some minor intergranular failure regions (inset of (c)). (e,f) At lower temperatures of 198 K crack propagation occurs mainly through intergranular fracture. The white arrow in (d) and the insets of (e) indicate polyhedral features that likely show the ends of recrystallization twins formed perpendicular to the grain boundaries into the grains during processing of the material [150].

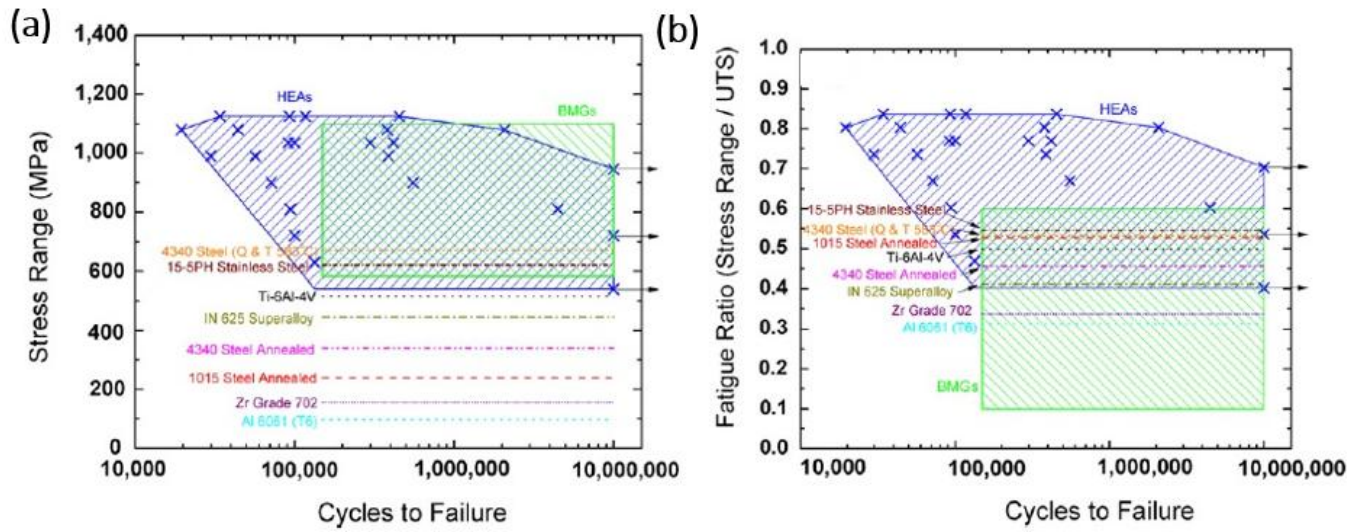


Fig. 37. Fatigue behavior of $\text{Al}_{0.5}\text{CrFeCoNiCu}$ alloy: (a) Stress range (S) vs. the number of cycles to failure (N) ($S-N$) curves of the $\text{Al}_{0.5}\text{CrFeCoNiCu}$ HEA compared with other alloys and bulk-metallic glasses (BMGs); (b) the fatigue ratios (stress range/UTS) of the $\text{Al}_{0.5}\text{CrFeCoNiCu}$ HEA, compared with other conventional alloys and BMGs [151]. Note that these graphs plot the stress range and not the customary stress amplitude (*i.e.*, half the stress range) which is invariably used for stress-life ($S-N$ or Wöhler) fatigue curves.

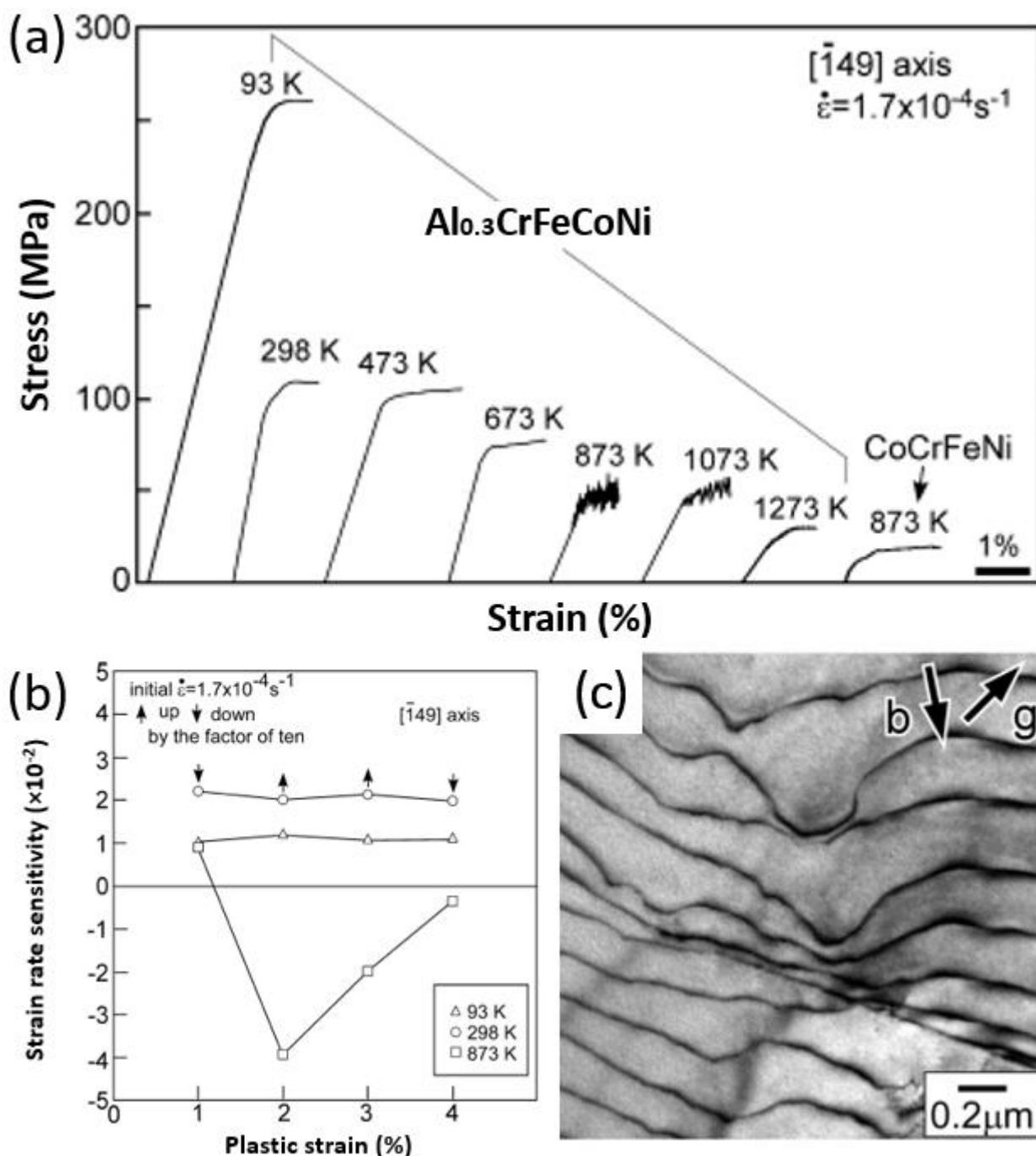


Fig. 38. (a) Stress vs. strain curves for $\text{Al}_{0.3}\text{CrFeCoNi}$ single crystal compressed at temperatures ranging from 93 K to 1273 K. (b) values of strain-rate sensitivity m at specific strain ε measured by strain-rate change testing. (c) TEM micrograph of the dislocation configuration on (111) plane of specimens deformed at 873 K [152].

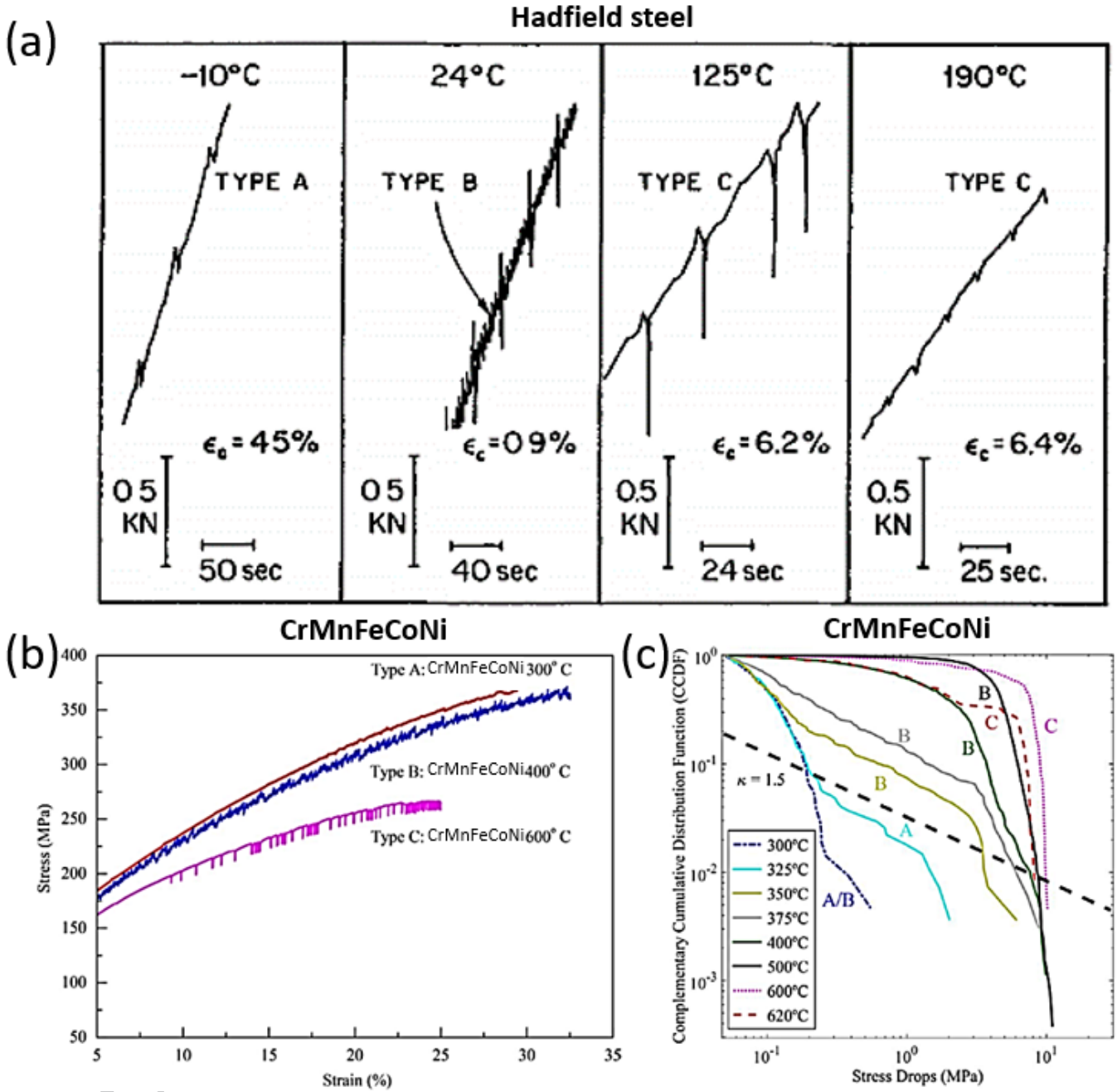


Fig. 39. (a) Serrated flow in Hadfield Manganese steel at different temperatures at the strain-rate of $3 \times 10^{-4} \text{ s}^{-1}$ [107]. (b) Representative stress-strain curves in the CrMnFeCoNi Cantor HEA at a constant strain-rate 10^{-4} s^{-1} , where stress drops and serrations can be observed. (Type-A example from the CrMnFeCoNi HEA at 300°C. Type-B example from the CrFeCoNi HEA at 400°C. Type-C example from the CrFeCoNi HEA, at 600°C.) (c) Complementary cumulative avalanche-size-distribution function $C(S)$ of the CrMnFeCoNi HEA with corresponding Portevin-Le Chatelier effect [159].

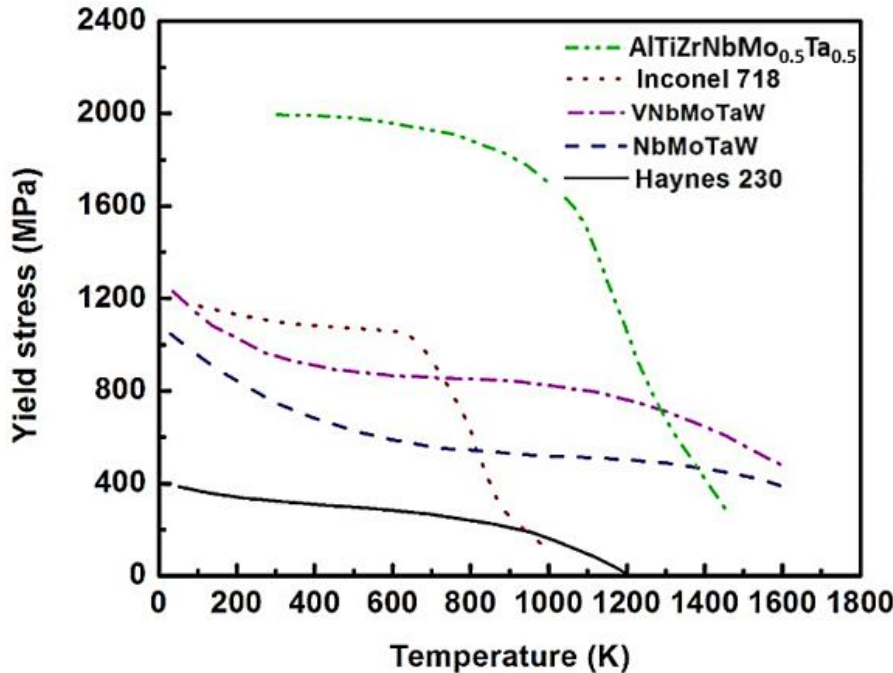


Fig. 40. Variation of yield stress with temperature for selected superalloys and HEAs: Haynes 230 alloy (mainly consisting of nickel-chromium-tungsten-molybdenum), Inconel 718 superalloy (mainly consisting of nickel-chromium-iron-tantalum-niobium-molybdenum), NbMoTaW HEA, VNbMoTaW HEA, AlTiZrNbMo_{0.5}Ta_{0.5} HEA [8].

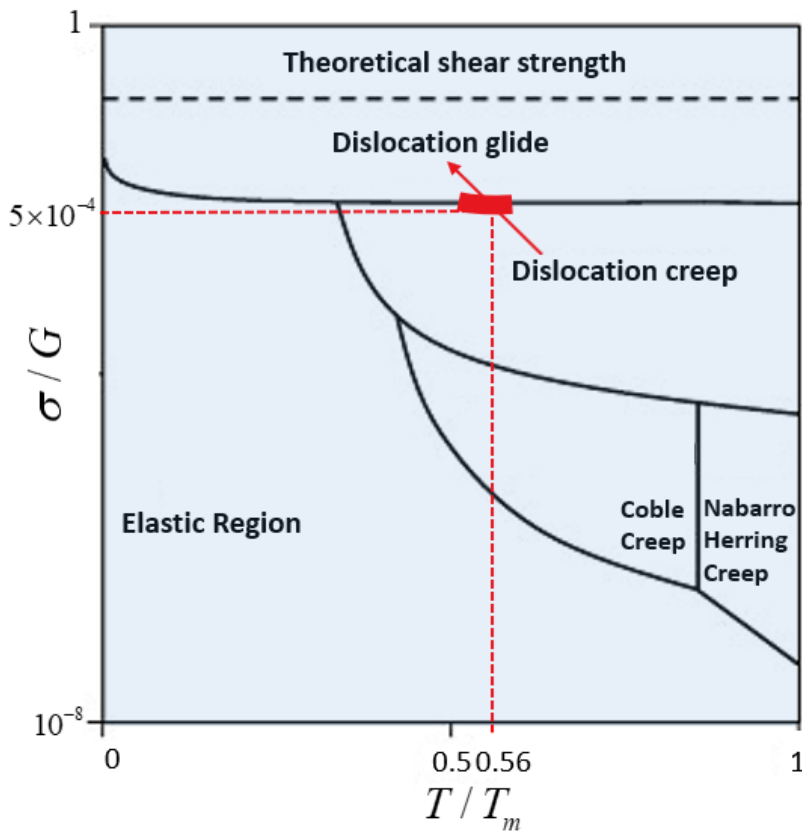


Fig. 41. Weertman–Ashby creep map showing different deformation mechanisms, with the red line showing the transition from the dislocation creep mechanism to the dislocation glide mechanism for the Cantor alloy [168].

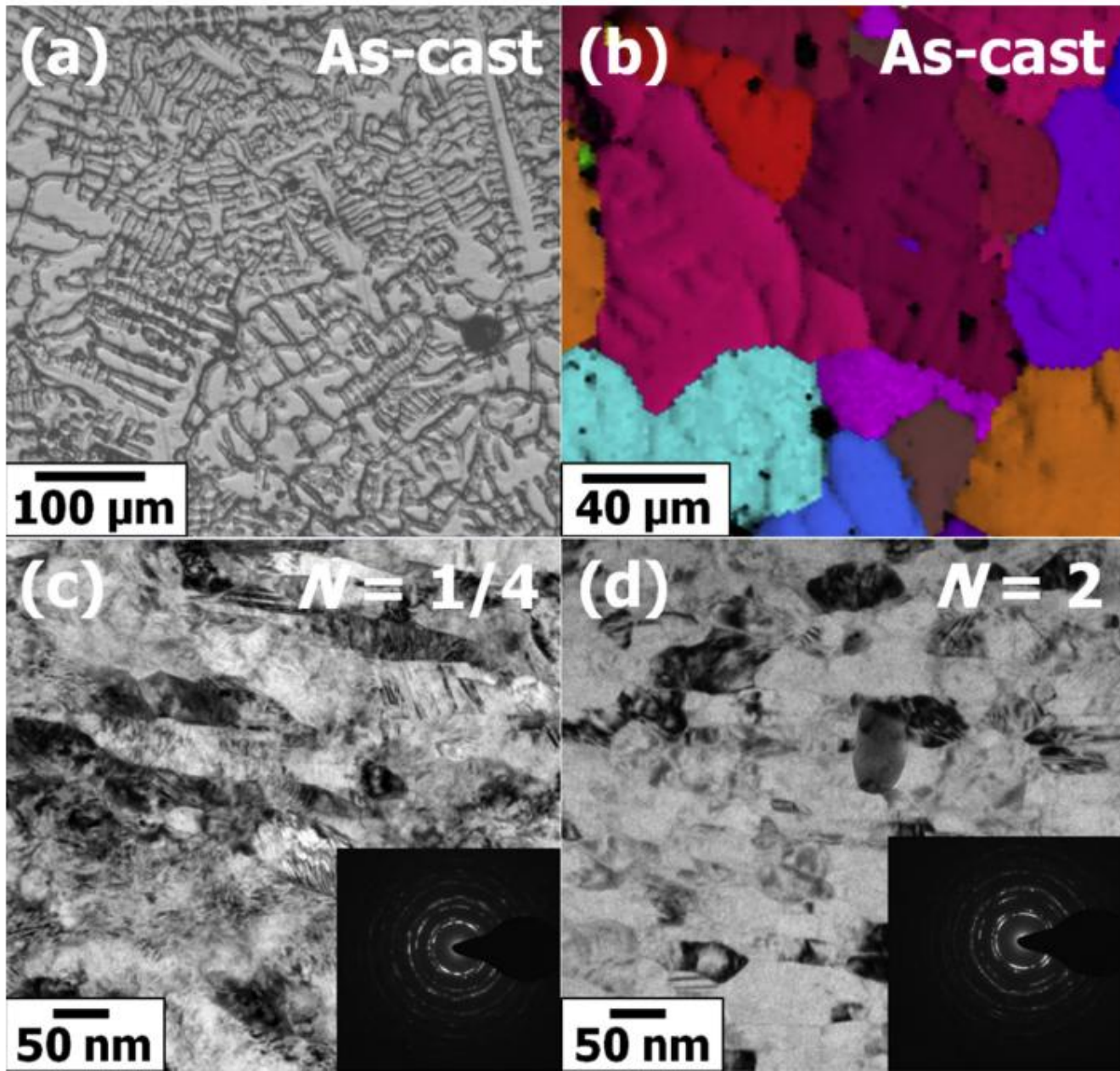
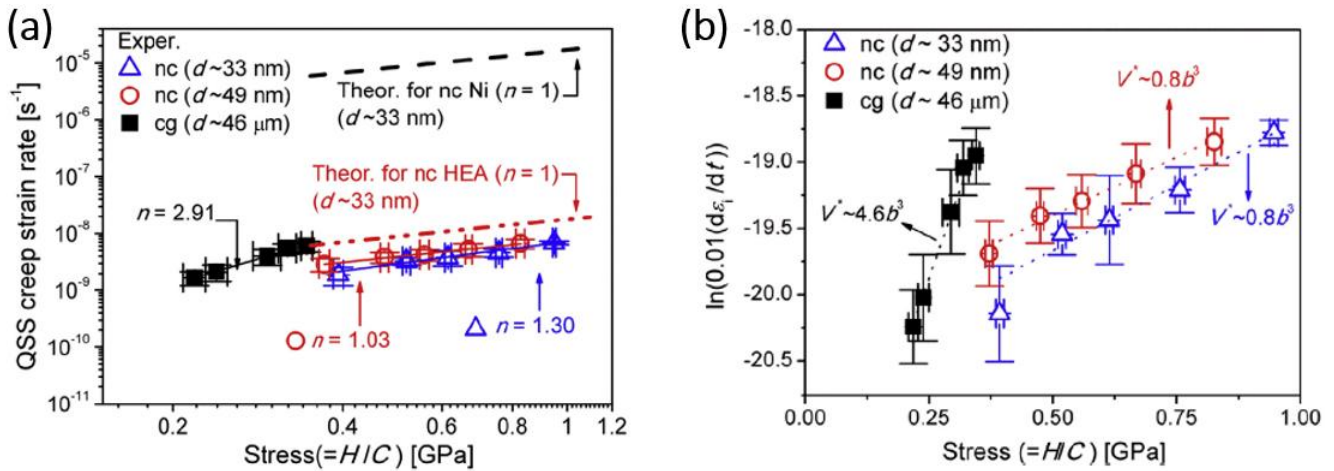


Fig. 42. (a) Optical microscopy image and (b) EBSD image of the as-cast CrMnFeCoNi Cantor HEA; TEM images taken at the edges of the high-pressure torsion disks after (c) 1/4 (applied equivalent strain of ~ 5 at the edge) and (d) 2 turns (applied equivalent strain of ~ 40 at the edge) with the corresponding selected area diffraction (SAD) patterns [40]. Note formation of equiaxed nanocrystalline grain structure after 2 turns with an equivalent strain of ~ 40 .



ACCEPTED MANUSCRIPT

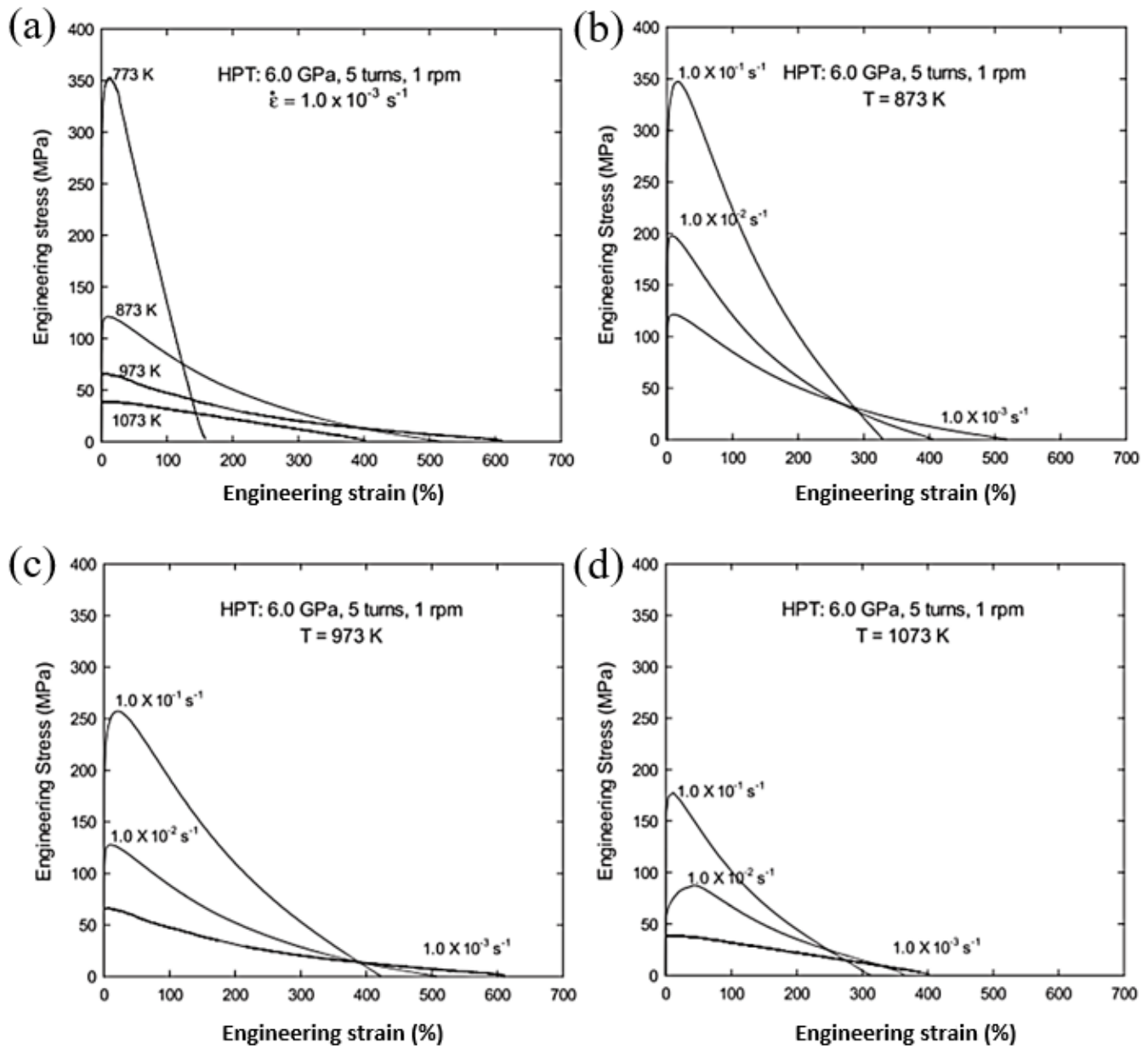


Fig. 44. Engineering stress-strain curves for the nanocrystalline CrMnFeCoNi Cantor HEA processed by large degree of high pressure torsion (five turns) under tension: (a) under constant strain-rate of $1.0 \times 10^{-3} \text{ s}^{-1}$ at various temperatures; at elevated temperatures (b) 873 K, (c) 973 K and (d) 1073 K at strain-rates ranging from 1.0×10^{-3} to $1.0 \times 10^{-1} \text{ s}^{-1}$ [173].

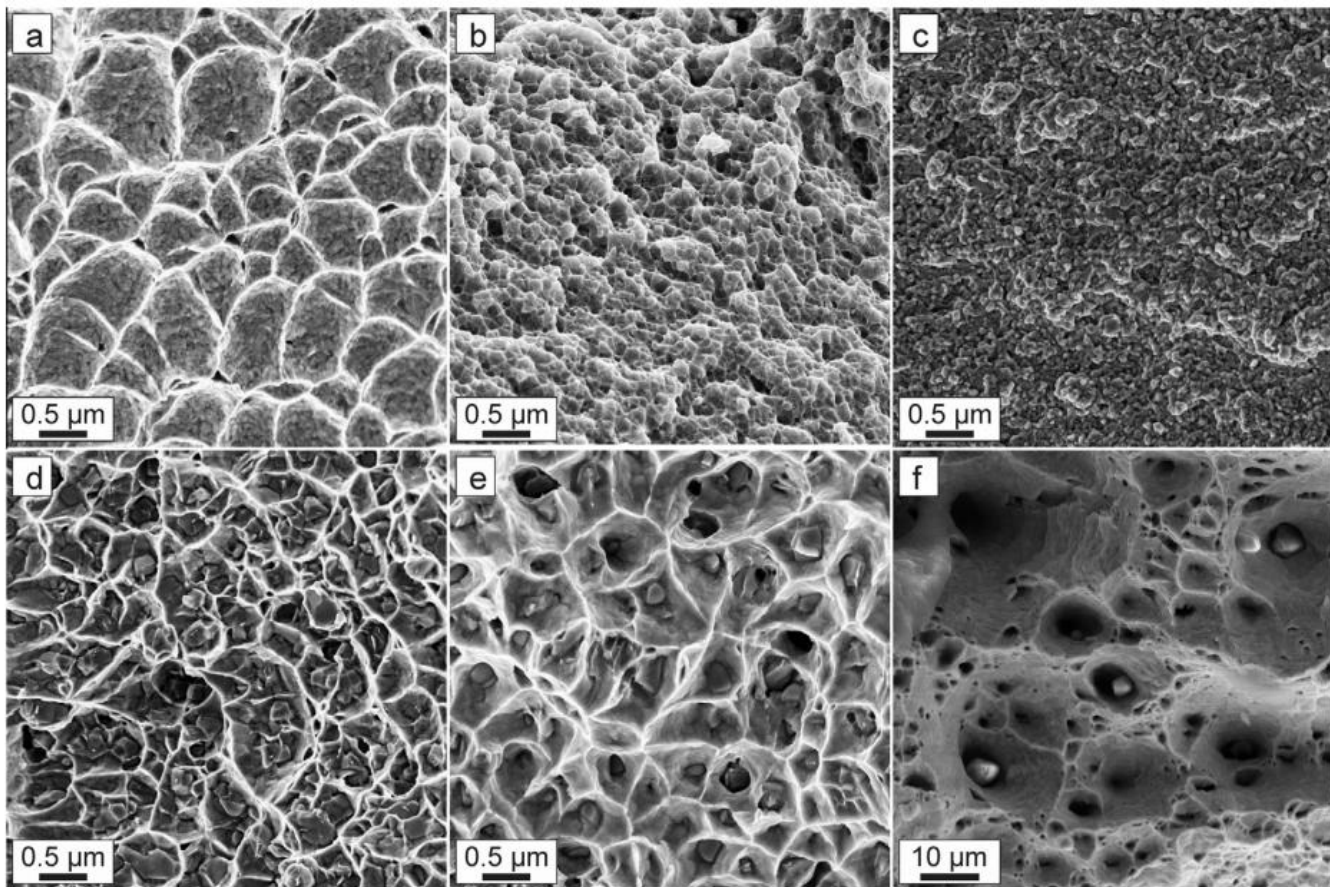


Fig. 45. Morphology of the tensile fracture surfaces of the CrMnFeCoNi HEA: (a) after high pressure torsion deformation, (b) annealed at 450°C for 1 h, (c) at 450°C for 15 h, (d) at 600°C for 1 h, (e) at 700°C for 1 h and (f) at 800°C for 1 h [70]. Note embrittlement for the 450°C anneal and dimple size increasing monotonically for the 600°, 700° and 800°C anneals [70].

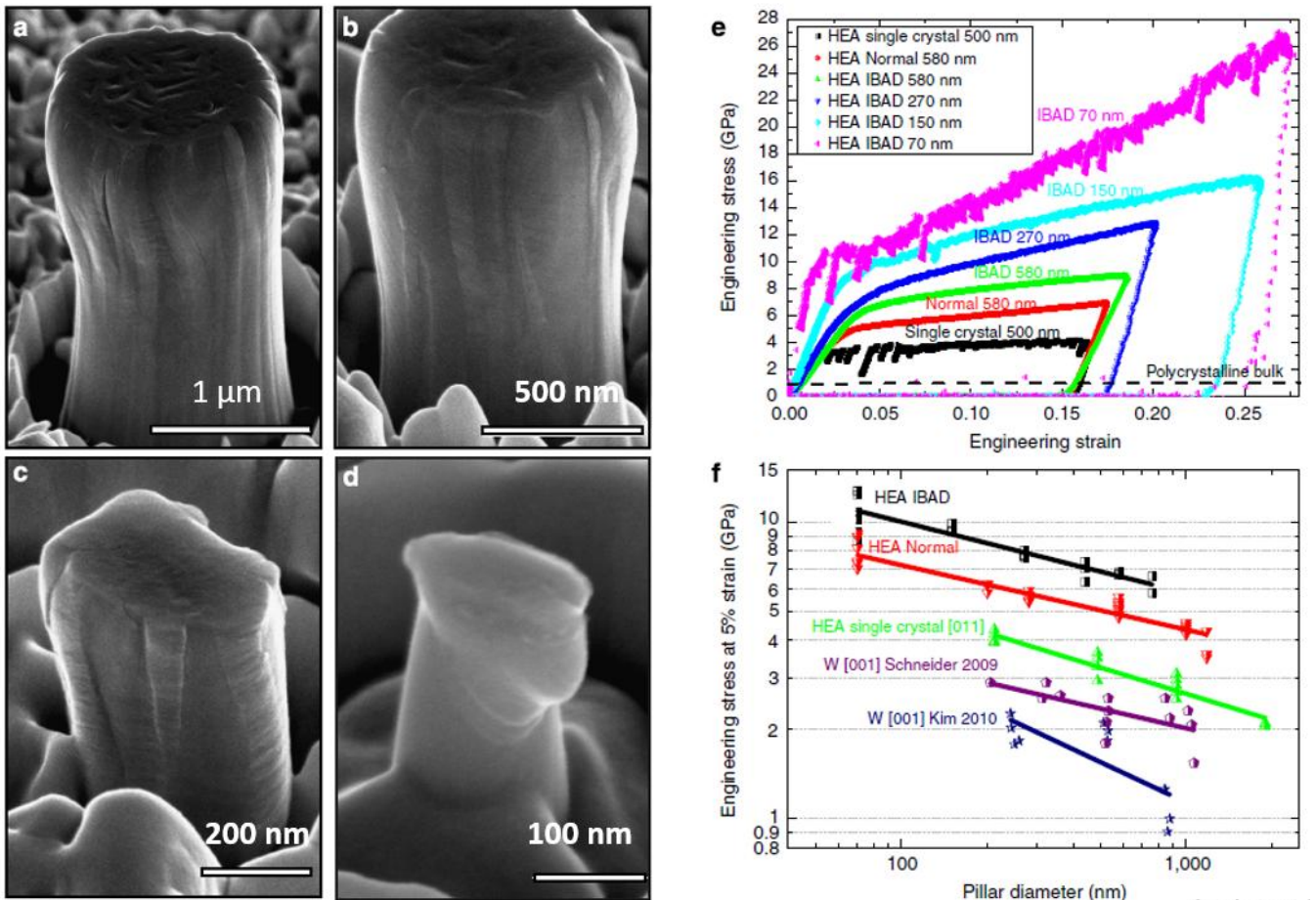


Fig. 46. (a–d) SEM images showing characteristics of as-deformed NbMoTaW HEA pillars with different initial diameters. The HEA is fabricated by ion beam-assisted deposition (IBAD) with diameter (D) ranging from $\sim 1 \mu\text{m}$ to 100 nm . (e) Stress–strain curves of the conventionally processed and IBAD HEA pillars, indicating a size-dependent strength. (f) A comparison of the strength–size relationships for the columnar-structured HEA pillars, single-crystal HEA and W pillars [182].

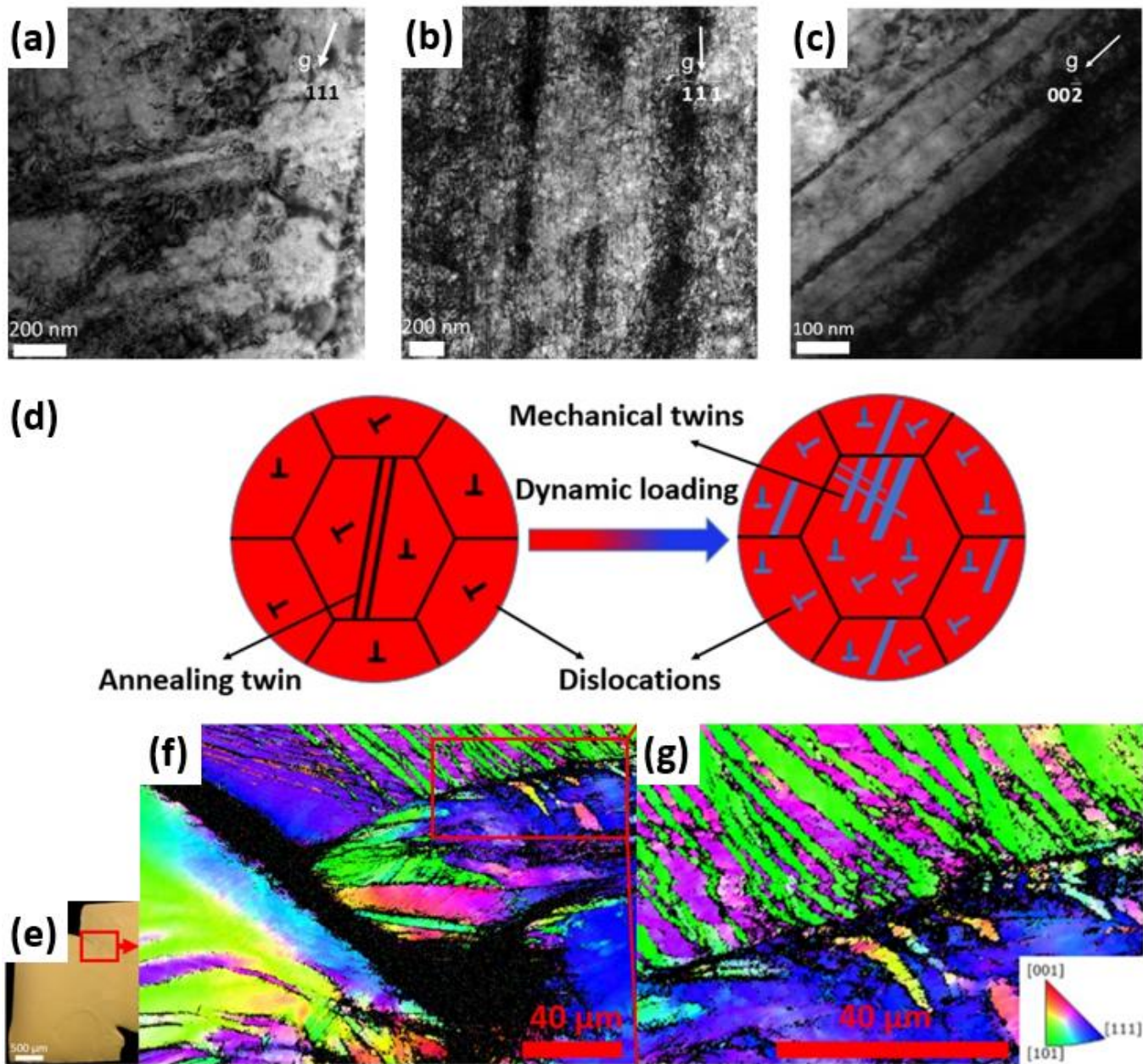


Fig. 47. TEM bright-field images of deformed Al_{0.3}CrFeCoNi HEA samples at quasi-static strain-rate of (a) 10^{-4} s^{-1} ; at high strain-rate of (b) and (c) 1800 s^{-1} . (d) Schematic sketches showing the deformation mechanisms under dynamic loading. (e) Optical microscopy image of the deformed hat-shaped sample. (f) EBSD image near the deformation tip. (g) EBSD image showing deformation twins near the deformation tip [96].

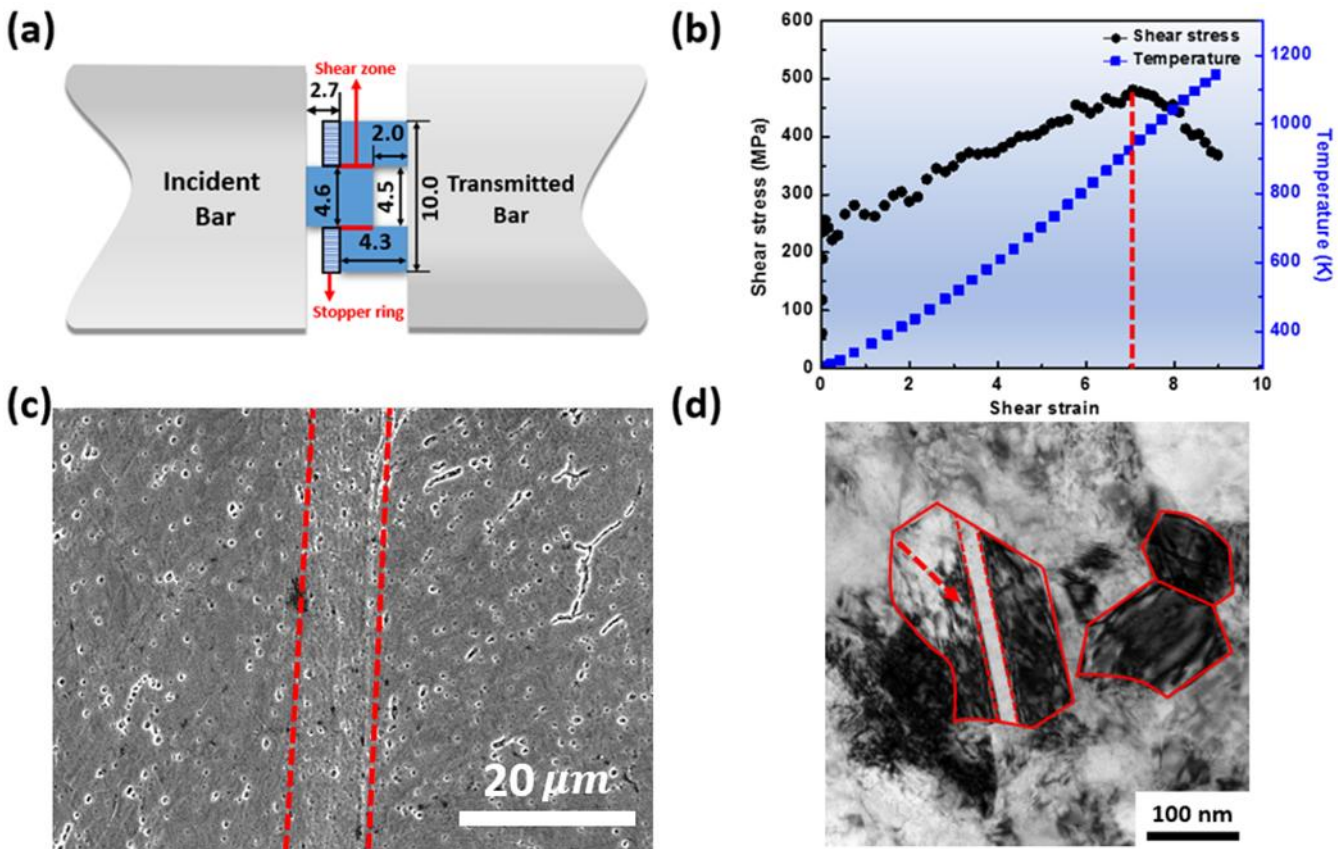


Fig. 48. (a) Schematic drawing showing the dynamically-loading hat-shaped specimen of the CrMnFeCoNi Cantor HEA with a split Hopkinson pressure bar; (b) mechanical response of forced localization in hat-shaped specimen and corresponding temperature rise; (c) SEM image of the shear band of the CrMnFeCoNi HEA; (d) TEM image of microstructure inside the shear band showing ultrafine grain size resulting from rotational dynamic recrystallization. The red arrow points to the recrystallized twin [197].

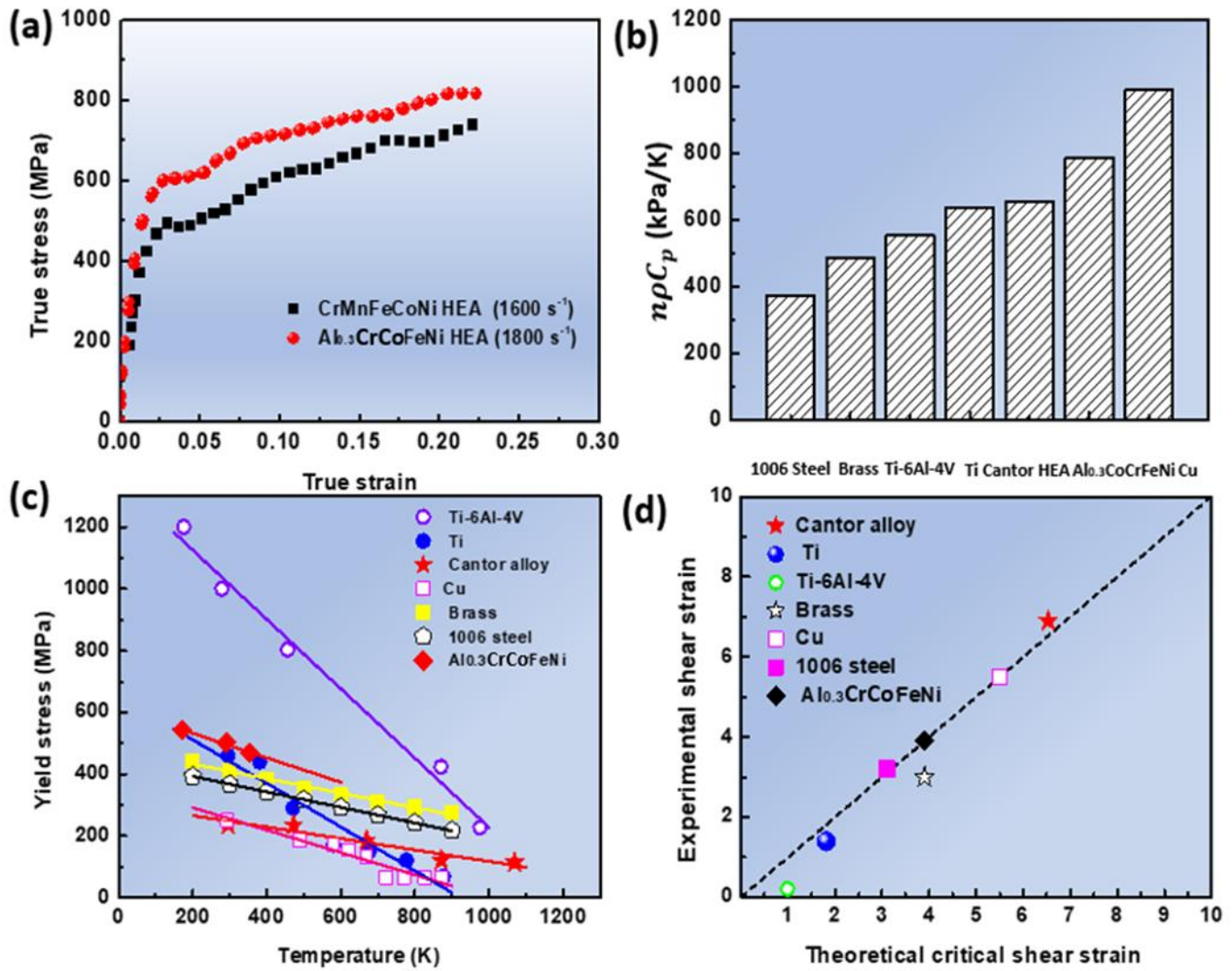


Fig. 49. (a) Mechanical response of Al_{0.3}CrCoFeNi HEA and CrMnFeCoNi Cantor alloy under high strain-rates; (b) values of $\rho C_p n$ (product of heat capacity C_p by density ρ by the work hardening coefficient n) for pure Ti, Ti-6Al-4V alloy, AISI 1006-steel, Copper, Brass, Al_{0.3}CrCoFeNi HEA and Cantor alloy; (c) thermal-softening rates of different materials; (d) predicted and experimental critical shear strain for shear localization [186].

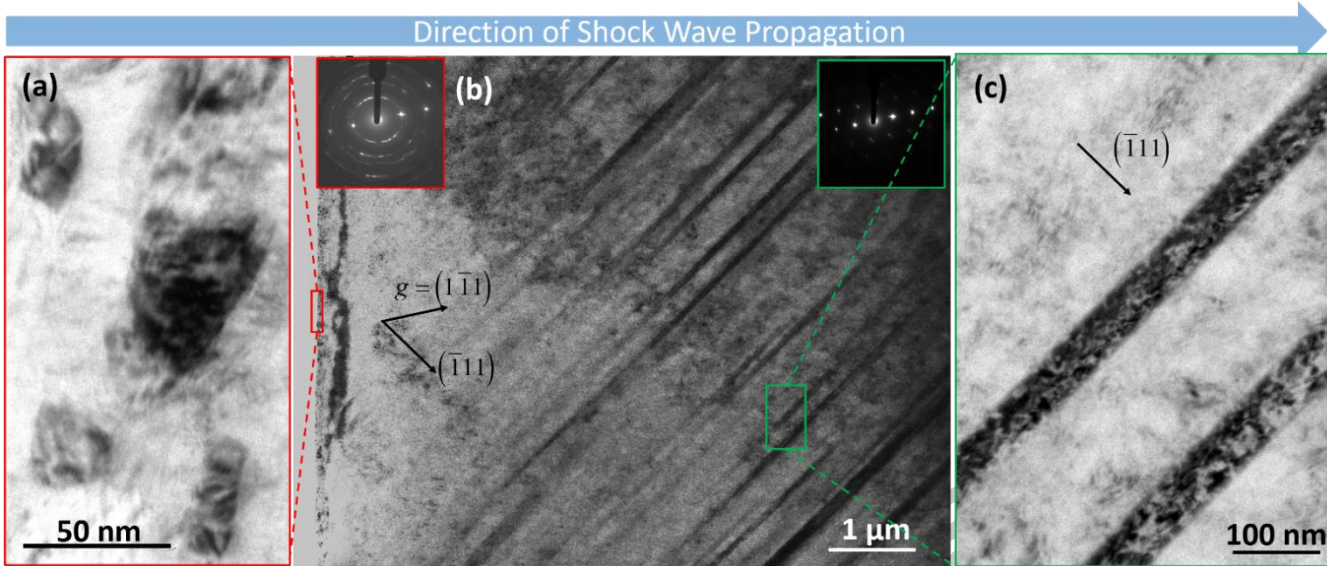


Fig. 50. Shock compression of $\text{Al}_{0.3}\text{CrFeCoNi}$ HEA using high-power pulsed laser generating an initial pressure of (100-200) GPa: (a) nanocrystalline layer covering the recovered sample; (b) low magnification TEM image shows high density of planar faults as the primary deformation mechanism; (c) magnified view of the planar faults. [194].

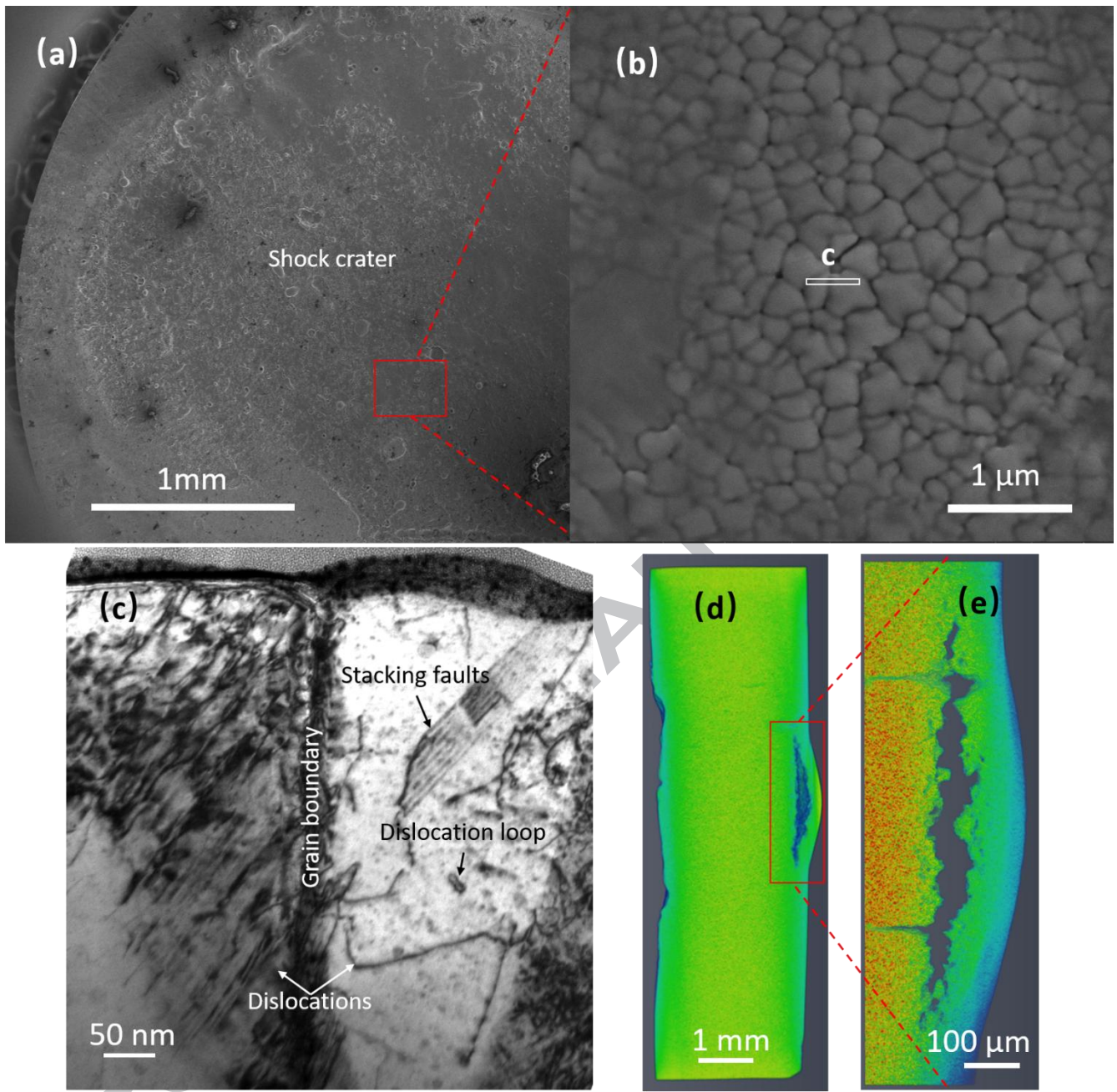


Fig. 51. Laser shock of the CrMnFeCoNi Cantor alloy. (a) SEM micrograph of the recovered sample with a shock crater visible at the front surface; (b) magnified view of the ultrafine-grained surface region inside the shock crater; (c) the cross-sectional TEM images of the regime close to the surface showing dislocations, stacking faults and nanoscale twins; (d) X-ray computed tomography of the laser shocked sample shows a crater (compression) in the front surface and a bulged rear surface (tension); (e) magnified view in the vicinity of the spall plane shows a rough fracture surface, indicating a ductile failure [195].